Title
Self-Injection Locking (SIL) Radar System for Vital Sign and Heart Motion Detection

Author
Reggad, Hind

Publication Date
2021

Peer reviewed|Thesis/dissertation

Self-Injection Locking (SIL) Radar System for Vital Sign and Heart Motion Detection

By

Hind Reggad

Dissertation

Submitted in partial satisfaction of the requirements for the degree of

Doctor of Philosophy

in

Electrical and Computer Engineering

in the

Office of Graduate Studies

of the

University of California

Davis

Approved:

Rajeevan Amirtharajah, Chair

Xiaoguang Liu

Anh Vu Pham

Committee in Charge

2021

To my parents, Abdu-Rahman and Rabia, whose sacrifice for me and my siblings is extraordinary and not existent. I hope with this achievement, I have fulfilled the dream you had for me all these years giving me the best education I could imagine.

To my loving husband, Justin, whose words of encouragements and supports lifted me up during the darkest time.

To my siblings, especially Youssef, for all their support and inspiration.

Contents

List of Figures

List of Tables

Abstract

Self-Injection Locking (SIL) Radar System for Vital Sign and Heart Motion Detection

Self-injection locked oscillators have been used in recent years in many applications such as motion sensing and have demonstrated good performance. Applications of this motion sending capability can be expanded to health care and biological signals. In fact, radar has been increasingly utilized to monitor human heart health in recent years, as it has many advantages compared to other available systems. Radar can be miniaturized unlike ECG, CT or MRI systems and so radar imaging can be very compact in size and therefore can be used in in-home care and for ambulatory monitoring. Also, radar sensors can actually detect the cardiac volume, as it is correlated with the heart motion, which can be utilized to monitor the heart and detect some known heart problems, such as heart arrhythmia; in addition, radar is a promising tool to be used for adjusting medications needed for heart failure patients. Several radar monitor products in the market prove to be accurate and efficient for monitoring sleeping quality and avoiding sleep apnea. Also, many research groups leveraged radar technology to successfully monitor heartbeat in both contact and non-contact scenarios. However, the systems used usually require two antennas, one each for the receiver and transmitter, and need more circuitry for leakage cancellation. Since the need for a portable heart monitor is increasing, specifications such as area and power need to be minimized. This work investigates an effective way to use self-injection locking in a radar system to detect cardiac motion with minimal hardware and reduced power. It expands the idea of using a phase-locked loop (PLL) system and a single antenna, which reduces system complexity. This work investigates and compares a LC-based voltage-controlled oscillator (LCVCO) and a ring voltage-controlled oscillator (RVCO) mainly in terms of sensitivity for motion detection and phase noise. A study of injection-locking of both the LCVCO and RVCO is also established. The study has proven that the RVCO is superior to the LCVCO in terms of sensitivity while the phase

noise won't be much different as the frequency of interest is very small, in fact heart rate and respiration frequency is band-limited up to a few Hertz. The sensitivity of both systems was studied, and was shown to be directly proportional to the locking range of the oscillators, or inversely proportional to the quality factors of the oscillators. However, while analytical expressions for the locking range and the quality factor of the LCVCO are well established, similar expressions for the RCVCO are not. In this work, a derivation of both the locking range and the quality factor of a 4-stage ring oscillator is presented. The theory demonstrated that a radar system based on a RVCO PLL has a better sensitivity and consumes less power and area, which makes it very suitable for a portable heart monitor. To verify the proposed idea, a design of both systems, LCVCO-based PLL and RVCO-based PLL was done in a 65 nm CMOS process at 1.5 GHz. The simulation and measurement results confirm the idea proposed. The RVCO shows better performance across all metrics: higher sensitivity by 4 dB, lower power consumption by 30 %, and smaller area, almost half, compared to the LCVCO.

Acknowledgments

This thesis is the fruit of years of hard work as a graduate student at the University of California, Davis. Throughout these years, my determination and fortitude toward finishing this dissertation grew stronger not only from small successes but also from failures along the way. First and for most, thanks to Allah Who enables me to achieve and complete this thesis. I owe my biggest gratitude to my father, who until the last day of his life has encouraged me to fulfil my dream to finish my Ph.D., as he didn't get the opportunity to complete his education. Also, I thank my mother who has planted in me the seed of love of education. My parents through their unconditional love and moral and financial support have enabled me to complete my undergraduate studies and set the stage for my graduate studies. To my husband Justin who lifted me in my lowest points during my doctoral journey and whose support and encouragement have been the light in my way. This achievement is equally mine as it's his. I am also thankful for my daughter, Noor, whose birth during my research has given me strength and commitment. My gratitude extends to all my siblings, Mohammed, Zainab, Bouchra, Youssef, Naima, Houda, Asmaa, Abdellah, Khadija, and Abdelhadi, who have helped me through this journey with moral and financial support. I also would like to express my gratitude to my in-laws, Drew and Deirdre, who have also supported me and been there for me. Further, I am very grateful to my family and friends, especially Vera, Lashauna, and Areaj, who have been by my side through this journey. Also, their support, advice and encouragement have made me the person I am now.

Also, I would like to thank my advisers, Prof. Xiaoguang Liu and Prof. Rajeevan Amirtharajah, who have introduced me to the RFIC design and have guided me throughout my PhD journey. In fact, there continuous guidance, encouragement, and enormous knowledge were crucial for the achievements and effective completion of this work. I cannot imagine I could be the researcher I am today without their tremendous support and advise. I want to thank Prof. Anh Vu Pham for being there at my qualification exam and providing me with useful insights and for reading me dissertation. I would like to thank, further, Prof. Hussain Al-Asaad and Dr. Dennis Matthews for also being part of

my qualification exam and have given me prolific guidance at the dawn of this project. I am also very thankful to Prof. Saif Islam who was the first mentor to introduce me to the world of research. Also, to Prof. Warren Smith, Prof. Perry Heedley, Prof. Steven Dehaas and Prof. Fethi Belkhouche who have guided and mentored me throughout my undergraduate and my master's journey at Sacramento State University of California.

Furthermore, I thank my friends and colleagues at the DART Lab. Dr. Chang Liu, Dr. Xiaohu Wu, Dr. Xiaomeng Gao, Xiaonan Jiang, Mahmoud Nafe, Daniel Kuzmenko, Hao Wang, Li Zhang, James Do, Jingjun Chen, Saleh Hassanzade, Songjie Bi and Naimul Hasan. They all have been a support system during my doctorate journey at Davis. Dr. Chang has provided me with great help and guidance during my first tape-out ever. I want to thank Xiaonan for helping me with the antennae design during this project. My thanks extend to Li, Jingjun and Daniel for there help with different tools in the lab. I also want to thank Hao for helping me with measurements and through his advice and recommendation which helped me with my internship at Skyworks.

.

Chapter 1

Introduction

1.1 Background

Radio detection and ranging or radar has been widely used in many different applications for a several decades. Radar uses radio waves to detect objects, motions and distances with different topologies. For instance, frequency-modulated continuous-wave (FMCW) radar systems have the ability to detect both the velocity and range of an object. Also, pulsed radar systems, which can be divided into two main groups, Basic Pulse Radar and Moving Target Indication Radar, are used when the received signal is very weak compared to the transmitted signal as using pulses permits the transmitting and receiving signals to happen at different times by sending a high-power signal and waiting for the echo signal from the object. Continuous-wave (CW) system are usually used to detect moving objects using the Doppler shift in the received signal. CW systems can't measure range and are usually used for speed measurement [11].

Radar technology, first developed for military applications, has expanded its utility to a broad spectrum of civil applications, including remote sensing like automotive radars, navigation, air traffic control and biomedical sensing [12]. In fact, biomedical radars are used to monitor biological targets and provide motion and location of a specific target for applications such as human-gesture identification and in-home health care monitoring. Indeed, radar technology does many things in improving in-home care monitoring, from detecting a person's presence, tracking him/her when moving while distinguishing the

movement from a wide spectrum: from the moving of the body as a whole to each limb and even internal movement like chest movement due to respiration and heart beating or even blood pressure [13].

Sensing human respiratory and heart motion using radar technology has been widely investigated. For respiratory systems, radars can detect the rate of respiration and even monitor the insurgence of some conditions related to problems with breathing. Radar can track respiratory rates while sleeping and can be also used to detect and help prevent sudden infant death syndrome (SIDS). Furthermore, concerning heart monitoring, while other systems, like the electrocardiogram (ECG), only detect the electrical signal going through the heart, radar systems can detect the real muscular movement of the heart, and thus radar can provide more accurate results and enables the detection and diagnosis of more complex heart problems such as arrhythmia. Furthermore, radar-based systems can also be used to detect survivors under rubble in the case for an earthquake for instance, and also provides accurate measurements through walls, obstacles, and clothing.

Also, radar systems can be safer compared to x-ray or computed tomography (CT) systems as it doesn't use any ionized detection method and thus is free of radioactive material. Another advantage is that radar can be miniaturized and be able to penetrate any obstacle. In fact, radar systems can be wearable and used in-home care monitoring, unlike ultrasound, CTs or magnetic resonance imaging (MRI) systems that are very bulky. In this research, the focus will be on developing a wearable miniaturized radar system to closely monitor heart movement and detect heart problems such as arrhythmia.

1.2 Cardio-Pulmonary Motion

In a human body, the heart, cardiac motion, and lungs, respiratory motion, are intimately interconnected in the chest cavity. The heart resides in the cardiac notch in the left lung. As a result, using Doppler radar to detect chest movement will automatically capture both the cardiac motion and the respiratory motion as well.

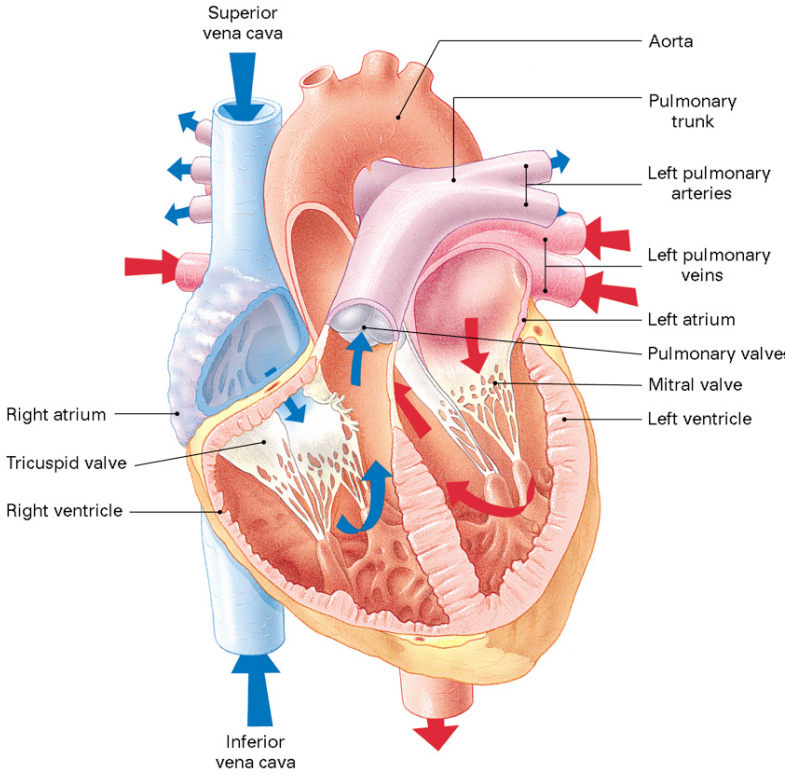

Figure 1.1: A diagrammatic section of the heart-physiology [1].

1.2.1 Heart motion

The heart, in a simplified version, can be considered as a two-pump system in series. The first pump, the right ventricle, is a low-pressure pump that sends blood to the lungs. While the second, the left ventricle, is a high-pressure pump that pumps blood to the body. The blood is delivered from the right ventricle to the lungs to pick up the oxygen from the air inhaled. The oxygenated blood is then returned to the left atrium and moves into the left ventricle. This then pumps the blood into the (high pressure) systemic arteries, where the oxygen moves into the tissues. Then, the de-oxygenated blood from the body flows through the (low pressure) veins back to the right atrium and then into the right ventricle where the cycle repeats [1]. When the heart goes through this cycle and contracts to create the pressure that drives blood flow, it move,s forcing the chest to move accordingly and producing a noticeable displacement at the surface of the skin.

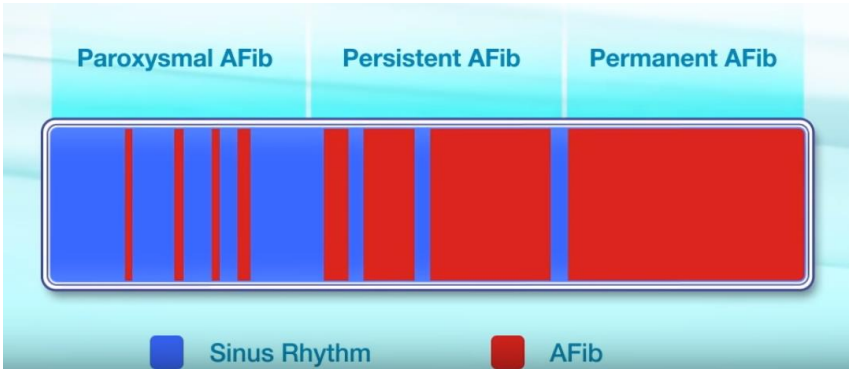

Figure 1.2: Different types of AFib episodes [2].

1.2.2 Respiratory Motion

Respiratory motion is related to the process of gas exchange within the lungs during breathing. The gas exchange happens when the atmospheric gas comes into intimate contact with blood. This process includes two systems, one for the gas and another for liquid. For this research, we are only interested in the gas system in the lungs. When inhaling air from the atmosphere, the diaphragm, a large dome-shaped muscle separating the thorax and the abdomen, contracts, moving downward and becoming flat, to increase the thoracic volume. In addition, the external intercostals, the muscles located between the ribs, rotate the ribs outwards and upwards to increase the cross-section of the thoracic cavity [1]. In fact, during inspiration, the thoracic cage expands both anteriorly and laterally, which is done by the rib and sternum movement. Exhalation, on the other hand, is passive and doesn't require any muscle activity. During expiration, the abdominal muscles contract, which increases the pressure against the diaphragm to bring it back to equilibrium state at rest. However, in other states, both inhalation and exhalation are active. During exercise, more muscles are used, the internal intercostals, to pull the ribs downward, decreasing the volume of the thorax and forcing exhalation [3].

1.2.3 Cardiac Diseases

The main motivation of this work is to save life. Heart disease is among the leading diseases that threatens human lives and deserves to be examined very carefully. In fact, strokes, one of the most serious heart diseases, is considered to be the fourth leading cause

of death in the United States of America, about 800,000 people have a stroke every year. According to the Centers for Disease Control (CDC), every 40 seconds someone has a stroke in the US and someone dies of a stroke every 4 minutes [2]. Moreover, in 2018, 1 in every 6 deaths from cardiovascular disease was a result of a stroke [2]. In a study, 15% to 20% of all strokes are attributed to one type of arrhythmia, Atrial Fibrillation (AFib) [14]. AFib patients have five times greater risk to get a stroke; however, if AFib is successfully diagnosed, then 75% of all AFib-related strokes can be prevented and lives could be saved. There are three types of AFibs: permanent, persistent and intermittent or paroxysmal AFib. As it can be seen from Fig. 1.2, permanent AFib happens when a person is constantly experiencing an arrhythmia episode while persistent AFib is when the arrhythmia is experienced more than 80% of the time. Intermittent AFib is the very challenging type to diagnose, because the arrhythmia episode can happen randomly, but can be as deadly. A person with an intermittent AFib can have an episode that may last from a few seconds to a few days which makes it hard to be accurately diagnosed.

1.2.4 Cardiac Monitoring Instrumentation

Traditionally, an electrocardiogram (ECG) or (EKG) is used to track the heart's motion, using surface electrodes on the body. The ECG captures the actual electric current generated within the heart from the cardiac muscle depolarization followed by repolarization within each cycle. It generates a waveform known as a PQRST waveform that is associated with one event from the cardiac cycle discussed, as shown in Fig. 1.3, a downward deflection on the ECG waveform suggests that the cells are depolarizing, or their charges are becoming positive, while the upward inflection implies a repolarization of the cells, becoming more negative in charge. The P wave is related to arterial depolarization which spreads from the SA node to the AV node. The PR interval represents the time to spread the signal from the sinus node to the AV node; it is measured from the start of the P wave to the start of the QRS complex. The latter in a healthy heart has a much higher amplitude than the P wave and is caused by ventricular depolarization. The J-joint is where the QRST ends and the ST segment begins, and it is a point that can suggest a few problems in the heart. The ST segment represents the ventricle's depolarization and

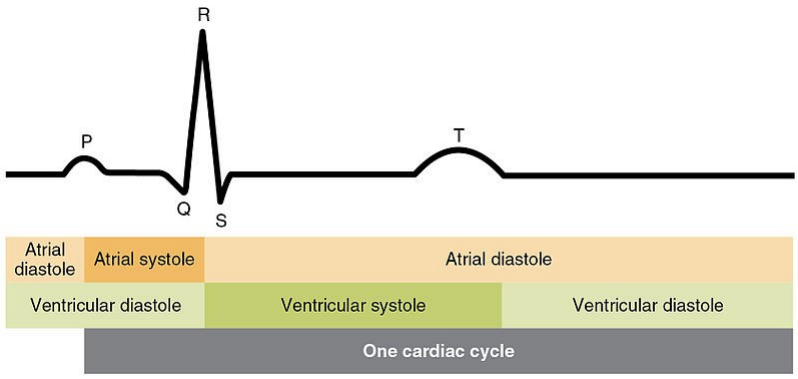

Figure 1.3: The cardiac cycle mapped with ECG [3] .

it connects the QRS complex to the T wave. Finally, the T wave is the repolarization of the ventricles [3]. In addition to the ECG, ultrasound imaging and other radiation-based medical techniques can also be used for heart monitoring. Ultrasound imaging scans the intracorporal organ structures by using ultrasound technology and it is accurate and a very mature technology. Although these technologies are very mature and have been widely used in hospitals, they have several drawbacks. In most cases, these techniques can only be accessed in hospitals or at doctors' offices, which is not convenient especially for patients living in rural areas. In addition, they are also not comfortable, as they require sticky gels and multiple electrodes attached to the body etc. Furthermore, another critical disadvantage of ECG and ultrasound is that they are not suitable for long-term monitoring of intermittent AFib mentioned above. Since the intermittent AFib can last any time between a few seconds to a few hours and happens randomly, to be successfully diagnosed with these techniques the patient needs to stay in the hospital for three days

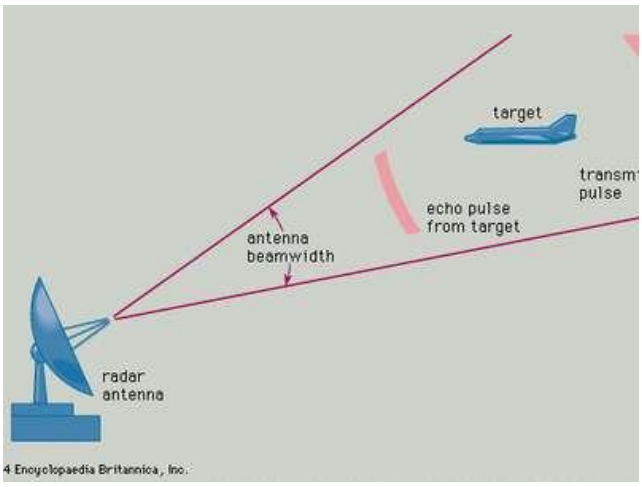

Figure 1.4: Radar system detecting a target [4]

or more. The only existing device for this kind of detection is a Holter monitor. A Holter monitor is a battery-operated portable device that measures and records the heart's activity (ECG) continuously for 24 to 48 hours or longer depending on the type of monitoring used [15]. People invented the Holter monitor to diagnose intermittent Afib; however, the Holter monitor requires many leads attached to the patient's body with sticky gels, which makes it not comfortable for the person to be wearing it for a long period of time. Thus, an alternative method needs to be used for cardiac long-term monitoring. One of the technologies that could be used is radar.

1.3 Radar Basics

Radar systems have been widely used in many different applications and are based on the transmission and reflection of electromagnetic (EM) waves. Radar uses radio waves to detect objects, motion and distances with different topologies. When an EM wave travels through two different materials with different dielectric constants or diamagnetic constants, the wave will either scatter or reflect from the boundary between the two materials. This concept is more useful for electrically conductive materials, metals for instance, which is utilized for submarines, automotive vehicles, and aircraft detection.

Radar uses EM waves to detect an object's location, speed and distance; it can further

track an object as it is moving. Radar is an active sensing approach with a transmitter and a receiver. As seen in Fig. 1.4, radar involves transmitting an EM wave into space from an antenna in a specific direction. The transmitted EM wave scans the space. Once an object is within the space of the transmitted wave, the object intercepts part of the transmitted energy and reflects another part, the echo, back to the antenna [4]. Radar has some factors that limit its performance, including wave scattering, clutter interference, and noise due to the circuitry. These limitations are encompassed in the radar range equation,

$$P_R = \frac{PtA_rG_t\sigma F^4}{(4\pi R_t R_r)^2}, \tag{1.1}$$

where P_R is the received power, A_r is the receiving antenna's effective aperture, G_t is the transmitting antenna's gain, σ is the target's radar cross section, F is the pattern propagation factor, R_t is the distance between the transmitter and the target, and R_r is the distance between the target and the receiver. To be able to detect the target and determine its specifications like distance, velocity etc., the echo or received power, P_R, needs to be larger than the noise level.

Radars are split into different categories based on their functionality and wave characteristics. For instance, frequency-modulated continuous-wave (FMCW) radar systems have the ability to detect both the velocity and range of an object. Also, pulsed radar systems, which consist of three main groups, are used when the received signal is very weak compared to the transmitted signal as it permits transmitting and receiving signals to happen at different times by sending a high-power signal and waiting for the echo signal from the object. In addition, continuous-wave (CW) systems are usually used to detect moving objects using the Doppler shift in the received signal but cannot measure the range and are therefore usually used for speed measurement [11].

1.3.1 CW vs. Pulsed Radar

Radar waveforms, as discussed before, can be divided into two general types: continuous-wave and pulsed. A CW radar is based on a continuous transmission for the RF signal, usually without interruption. The same is also applied to the receiver as well. They are

based on a simple architecture and can be used for both heterodyne and homodyne receivers [11]. The CW radar is narrow-band, as a result the filters in the receiver end of the system can be easily implemented. Also, when interested in measuring the displacement or the velocity of an object, the signal processing is straightforward. In addition, a pure CW radar system can unmistakably detect and measure the velocity and displacement of any object at any range and moving at any velocity. One of the issues of the CW is that it suffers from a poor isolation between the transmitter and receiver, and a fraction of the signal leaks between the two through coupling or through the antenna. In fact, the small signal leaked between the two relegates the CW system to have relatively low power and as a result to short-range detection [16]. Another issue worth mentioning is the signal and its noise sidebands reflected from the clutters in the environment back to the receiver, which combined with the leakage signal, add a DC offset and low frequency noise to the desired signal.

The Doppler radar is useful in measuring the velocity of a target using a continuous wave. The system transmits a constant frequency signal, which is reflected from the target and received by the radar's receiver. If the target is not moving then the frequencies are not changed. However, if the target is moving, then the frequency received by the radar is changed by the Doppler effect. In fact, the Doppler effect's equation is,

$$f_r = f_t \frac{1 + v/c}{(1 - v/c}, \tag{1.2}$$

where f_r is the shifted received frequency, f_t is the original frequency, v is the target velocity, and c is the speed of light. Equation 1.2 can be simplified as,

$$f_r = f_t \frac{c + v}{c - v}. \tag{1.3}$$

The Doppler frequency or the beat frequency can be expressed as,

$$f_d = f_r - f_t = 2v \frac{f_t}{c - v}. \tag{1.4}$$

In many Doppler applications the speed of the target $v << c$, then equation 1.6 is:

$$f_d = 2v \frac{f_t}{c}, \tag{1.5}$$

and the target velocity is determined from,

$$v = \frac{f_d c}{2 f_t}. \tag{1.6}$$

On the other hand, a pulsed-based radar system uses a pulse generator to transmit a burst of energy and waits for the echoes from the target. It transmits waves during a very short time duration, with a pulse width of τ that can be ranging from a few nanoseconds to sometimes as miliseconds. One of the advantages of the pulsed radar is that during transmission, the receiver is completely isolated from the antenna, avoiding leakage and protecting it from the transmitter high power signal. Moreover, the pulsed radar has the ability to measure the object range instantaneously. However, the implementation of the pulsed radar is very complex. Although pulsed radar uses only one antenna for receiving and transmitting, it requires a very high power. In this application, cariopulmonary monitoring, the range measurements are not useful in detecting the biological signals [17], CW radar will be used in this work.

1.4 History Of Vital Signs Radar-Based Sensors

The first practical radar system was invented in 1935 by the British physicist Sir Robert Watson-Watt and used for military applications. It wasn't until the year of 1971 when the first radar system was used for vital signs sensing. In fact, the system was used to sense sleep apnea in infants by tracking respiratory rates using an antenna that is 50 cm away from the tested subject and would send a warning if breathing was not detected for more than 30 s [18]. While the first demonstrated heart rate measurement was demonstrated in [19], where a radar system, with a 2 GHz antenna placed at 3 cm away, was used to capture heart rate while holding breath. After that, many different systems were presented trying to improve the sensing of vital signs in terms of both signal processing and hardware simultaneously while separating the respiratory rate from the weak heart rate signal. The work done in [20] has proven to detect vital signs of subjects using a digital rate detection algorithm. It used for the first time a quadrature receiver to avoid the null point problem during phase demodulation. The null points happen at every quarter wavelength and can be addressed by quadrature transmission. In [21] [22]

successful measurements were presented using automatic clutter cancellation to detect respiratory and heart rate for people under seven layers of rubble, seven feet of bricks and behind walls.

After that, and in the last 20 years, the development of radar systems for vital sign detection has known a fast growth focusing on improving the technology in terms of power consumption, size, weight, detection range, accuracy and robustness for noncontact and wearable sensors [23]. Research has focused on different aspects of the radar sensors for biomedical applications, including antennae, signal processing, and the hardware development itself, using ultra-wideband (UWB) pulse radar or continuous wave (CW) radar; ranging from using the standard architecture of a transmitter/receiver-based system with two antennae or using a circulator to using self-injection-locking (SIL) theory. In fact, many researchers in the 2000s have prioritized the improvement of antennae to enhance the sensitivity of the radar-based sensor; both cancer tumors [24] [25] [26] and chest movement due to respiration and heart beating [27] [28] [29] were targeted as applications.

1.4.1 Summary Of The Dissertation

The structure of this dissertation is as follows. Chapter 1 has presented an overview of cardiopulmonary function and the importance of monitoring them. It also discussed some of the standard medical instrumentation for heart monitoring. Also, radar systems are presented as a suitable alternative for the traditional detection methods. Radar has advantages over these instruments because of many reasons. Finally, different types of radar systems were addressed and the CW based radar is chosen for this application.

Chapter 2 presents a detailed overview of the human heart anatomy and the basics of the cardiopulmonary motion. It also describes cardiac diseases, e.g., arrhythmia. It also shed the light on the electrical stimulation of the heart that helps with heart motion detection. Further, since radar will be used for detection, a path for the least power loss of EM propagation was established.

Chapter 3 describes the theory of SIL operation. It also discusses the literature review of different work published on SIL systems for vital sign monitoring.

Chapter 4 presents the SIL radar system based on a PLL as a demodulator. It also

presents a sensitivity and phase noise study of the proposed SIL radar system using two different VCO architectures.

Chapter 5 presents the theory of the phase-locked loop (PLL) design. It analyses each block of the PLL and presents an analysis of the loop in terms of transient response, stability and phase noise.

Chapter 6 presents the proposed SIL radar system based on both the LCVCO and the RCVCO. It presents the circuit simulations and layout. It also presents the antenna design used for this vital sign detection system.

Chapter 7 discusses the experimental characterization of the proposed sensor. It also presents a quantitative comparison between both SIL radar systems based on the LCVCO and the RVCO oscillator.

Finally, Chapter 9 presents conclusions and future work.

Chapter 2

Understanding Cardiac Arrhythmia

2.1 Cardiopulmonary Motion

In a human body, the heart, cardiac motion, and lungs, respiratory motion, are intimately interconnected in the chest cavity. The heart resides in the cardiac notch in the left lung. To have a better understanding of how to measure the heart signal and identify heart arrhythmia, we have to understand the fundamentals of the heart's anatomy and motion.

2.1.1 Heart Anatomy

The heart is one the most essential organs in the human body. It's a very complex hollow muscular organ that keeps all other organs alive. As shown in Fig. 2.1 the heart can be considered as a two-pump system in series. The first one, the right ventricle, is a low-pressure pump that sends blood to the lungs. While the second, the left ventricle, is a high-pressure pump which pumps blood to the body. The blood is delivered from the right ventricle to the lung to pick up the oxygen from the air inhaled. The oxygenated blood is then returned to the left atrium and moves into the left ventricle. This later pump the blood into the (high pressure) systemic arteries, where the oxygen moves into the tissues. Then, the de-oxygenated blood from the body flows through the (low pressure) veins back to the right atrium then into the right ventricle and the cycle repeats [1] . When the heart goes through this cycle and contracts to create the pressure that drives blood flow, it moves forcing the chest to move accordingly and produce a noticeable displacement at the surface of the skin.

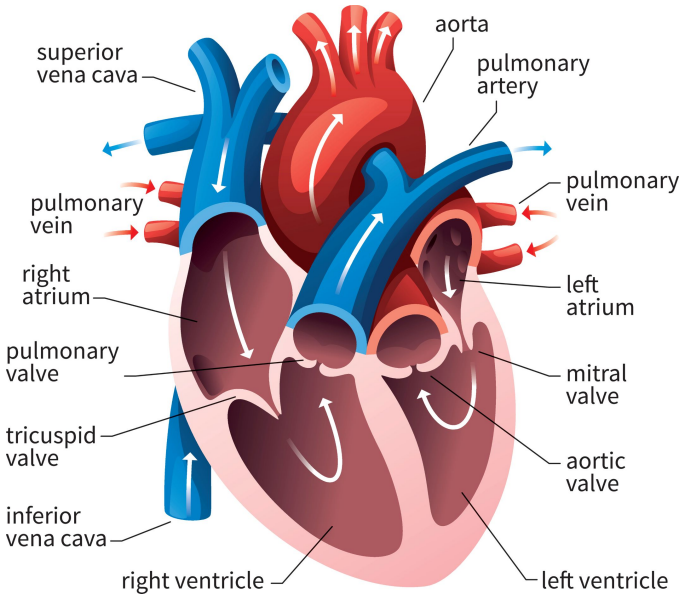

Figure 2.1: A diagrammatic section of the heart physiology [1].

In the human body, the heart is surrounded by the pericardium and is located in the chest between the lungs behind the sternum and above the diaphragm. It is smaller compared to the lungs, in fact it only weighs about 275 g in average and has the size of a fist. It measures 12 cm long, 8-9 cm wide and 6 cm from front to back. It is composed of three layers, endocardium, myocardium, and pericardium. The endocardium is the smooth inside thin lining of the heart. The myocardium is the middle layer of the heart muscle. The pericardium is the fluid sac that surrounds it. The blood flows from the vena cava, Fig. 2.1, into the right atrium septum to the right ventricle, which pushes it into the lungs via the pulmonary arteries. The blood then absorbs the oxygen from the lungs and returns to the left atrium through the pulmonary veins. When the mitral valve is open, blood from the left atrium enters the left ventricle. After, it enters the left ventricle, as this later contracts, the aortic valve opens and blood is injected out the aorta to the body through the aortic valve providing oxygen and nutrients to the rest of the body and removing carbon dioxide from it in the meantime. The valves of the heart are crucial for the directionality of blood flow; they are passive and open and close corresponding to the pressure differences in the heart chambers. They open to relieve the over-pressure in a chamber and closes to prevent back-flow [1]. The adult human heart beats at an average

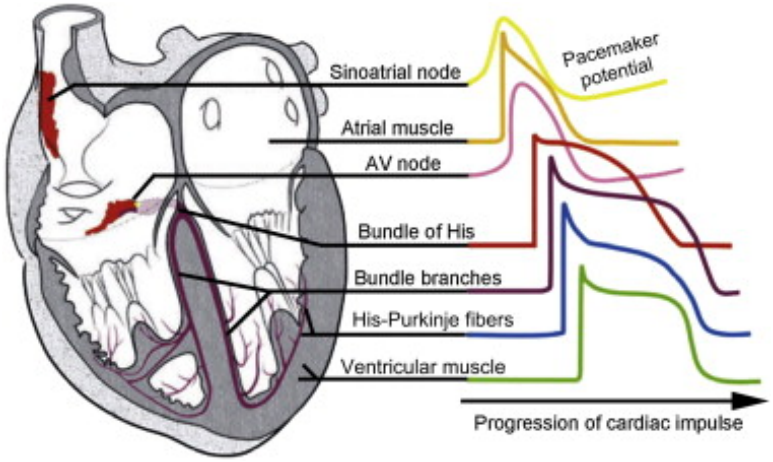

Figure 2.2: The propagation of the electrical signal through the heart starting at the SA node [5]

rate of 70 beats per minute (bpm) and pumps approximately 6-7.5 liters of blood daily, beating about 115,000 times each day. However, heart rate is different from one person to another depending on age and a person's physical activity. For instance, for a person at rest, the heart rate can goes as low as 50 pbm and goes higher than 150 bpm during moderate intensity activities [1].

2.1.2 Electrical Stimulation Of The Heart

The contractions of the muscles of the heart have to be effectively timed and globally organized for the heart to properly function. To establish that, the heart has a conduction system that initiates a contraction and then distributes it throughout the heart. This system starts with an excitation of the action potential at the pacemakers, which occurs in the sinoatrial (SA) node, then it spreads during atrial systole in the atria. Then, the excitation is delayed when it arrives at the atrioventricular (AV) node, Fig. 2.2. Subsequently, the electrical signal goes to the Bundle of His, and after that it divides into the right and left Bundle branches where it propagates rapidly through His-Purkinje fibers to the right and left ventricle. As the excitation spreads down the septum, it triggers a contraction that moves the ventricles upward to pump the blood out [5]. The SA node is the central pacemaker of the heart, but any of the other electrical tissues can be a pacemaker as well. The advantage of the SA node is that it can generate a faster electric

impulse compared to the others. However, in the case of an the SA node failure, the other parts of the electrical system can take over at a slower pace. In addition to the pacemaker cells' electrical signal that causes the heart to beat, some nerves, from the autonomic nervous system, can change the rate of the pacemaker cells and how strongly the heart contracts. The autonomic nervous system consists of the sympathetic nervous system and the parasympathetic nervous system both having opposite function. The parasympathetic nerves decrease the heart rate and decrease the force of contraction. In contrast, the sympathetic nerves increase the heart rate and increase the force of contraction.

The cardiac cycle begins by an atrial systole that forces a small amount of blood into the relaxed ventricles. This process of atrial systole lasts for about 100 ms and is responsible for a fifth of the ventricular filling, then the atrial diastole starts. After that, ventricular systole starts, which causes the aortic valve to close. As the ventricular pressure increases above the arteries' pressure, the semilunar valves open and blood starts flowing. The whole process lasts for about 300 ms. The third stage is the ventricular diastole. It starts with the relaxation of the ventricles and the pressure drop in them; this closes the semilunar valves as blood flows back against their ends to fill the relaxed atria. At the end all heart chambers relax and the ventricles get filled passively. This last stage of ventricular diastole lasts for about 500 ms [1]. The phases of this cycle are outlined in Fig. 2.3. These stages produce an electrical signal that can be measured. This measurements are usually captured and represented in a graph referred to as an electrocardiogram (ECG or EKG). Fig. 2.4 shows an example of the ECG waveform.

The ECG captures the actual electric current generated within the heart from the cardiac muscle depolarization followed by repolarization within each cycle. The signal is captured by electrodes attached to the surface of the skin on the chest, recorded, processed and displayed on an ECG device. The ECG generates a waveform known as a PQRST waveform that is associated with one event from the cardiac cycle discussed, as shown in Fig. 2.4, a downward deflection on the ECG waveform suggests that the cells are depolarizing, or their charges are becoming positive. An upward inflection implies

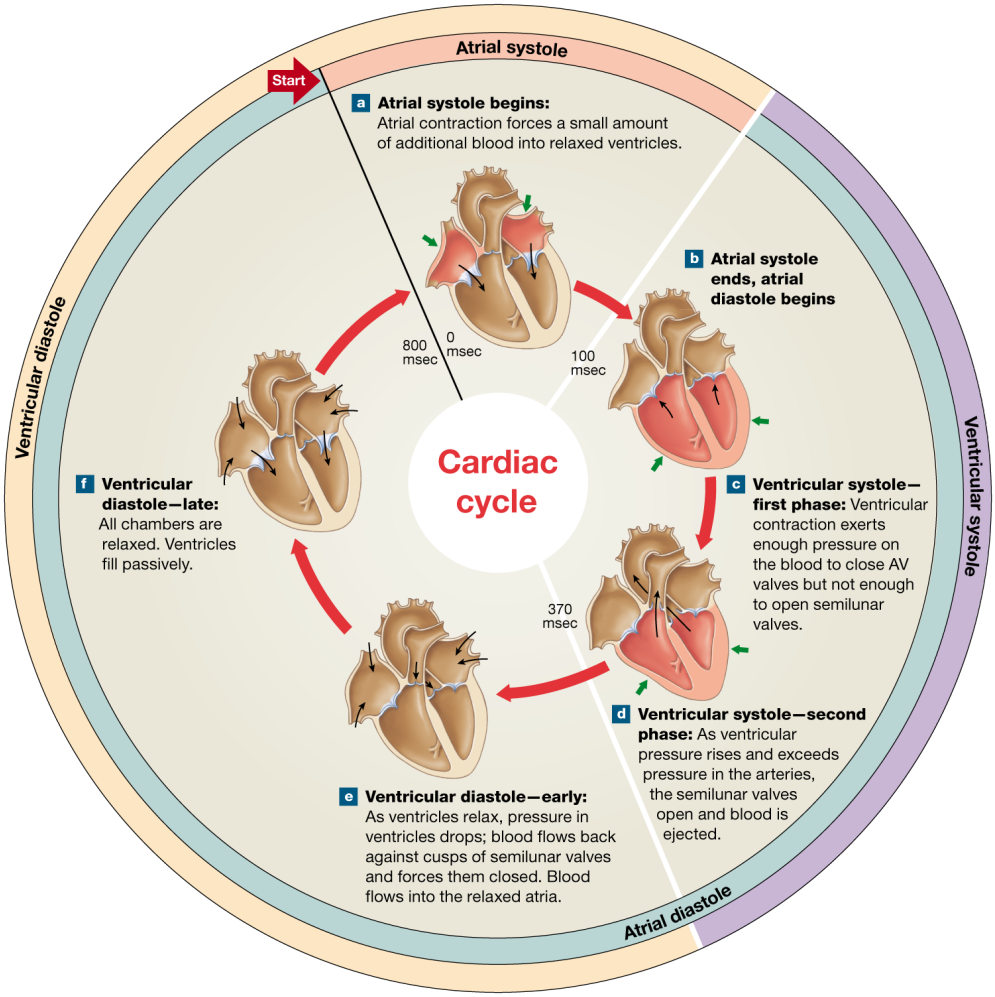

Figure 2.3: The cardiac cycle [1].

a repolarization of the cells, becoming more negative in charge [30]. The events of the PQRST ECG signal are as follows:

- P wave - is related to arterial depolarization which spreads from the SA node to the AV node. It coincides with the spread of the electrical signal in the atria and the beginning contraction.
- PR interval - represents the time to spread the signal from the sinus node to the AV node; it is measured from the start of the P wave to the start of the QRS complex.
- QRS - in a healthy heart has a much higher amplitude than the P wave and is caused by the ventricular depolarization. It coincides with the spread of the electrical signal in the ventricles and the beginning contraction.
- J-joint - is where the QRST ends and the ST segment begins; it is just a point that can suggest few problems in the heart.
- ST segment - represents the ventricles' depolarization and it connects the QRS complex to the T wave.
- T wave - is the repolarization and the recovery phase of the ventricles.

2.1.3 Respiratory Motion

Respiratory motion is related to the process of gas exchange within the lungs during breathing. The gas exchange happens when the atmospheric gas comes into intimate contact with blood. This process includes two systems, one for the gas and another for liquid. For this research, we are only interested in the gas system in the lungs. When inhaling air from the atmosphere, the diaphragm, a large dome-shaped muscle separating the thorax and the abdomen, contracts moving downward and becoming flat, to increase the thoracic volume. In addition, the external intercostals, the muscles located between the ribs, rotate the ribs outwards and upwards to increase the cross-section of the thoracic cavity [1]. In fact, during inspiration, the thoracic cage expands both anteriorly and laterally, which is done by the rib and sternum movement. Exhalation, on the other

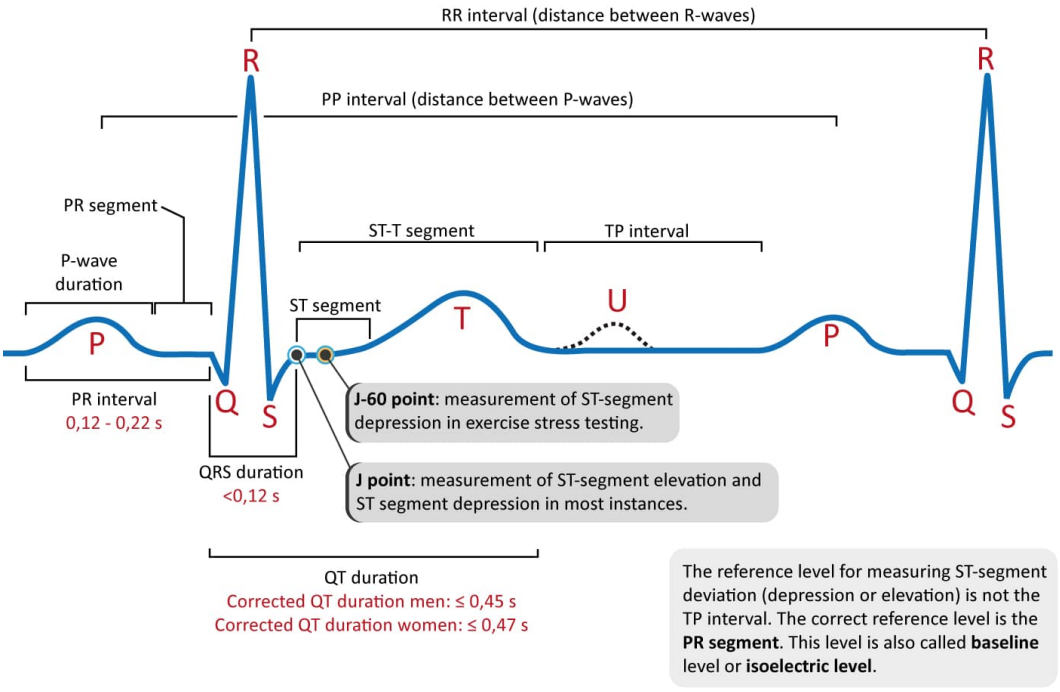

Figure 2.4: ECG waveform [6]

hand, is passive and doesn't require any muscle activity. During expiration, the abdominal muscles contract, which increases the pressure against the diaphragm to bring it back to equilibrium state at rest. However, in other states, both inhalation and exhalation are active. During exercise, more muscles are used, the internal intercostals, to pull the ribs downward, decreasing the volume of the thorax and forcing exhalation [3].

2.2 Cardiac Arrhythmia

The heart is a very complex organ and its problems are also complex. Strokes, one of the most serious heart diseases, is considered to be the fourth leading cause of death in the United States of America; in fact about 800,000 people have a stroke every year. According to the CDC, every 40 seconds someone has a stroke in the US and someone dies of a stroke every 4 minutes [2]. Moreover, in 2018, 1 in every 6 deaths from cardiovascular disease was a result of a stroke [2]. Cardiac arrhythmia is an irregular heartbeats. It is defined when the heart beats too fast (tachycardia) or too slow (bradycardia) in an chaotic fashion. In this section, Atrial Fibrillation and other types of cardiac arrhythmia

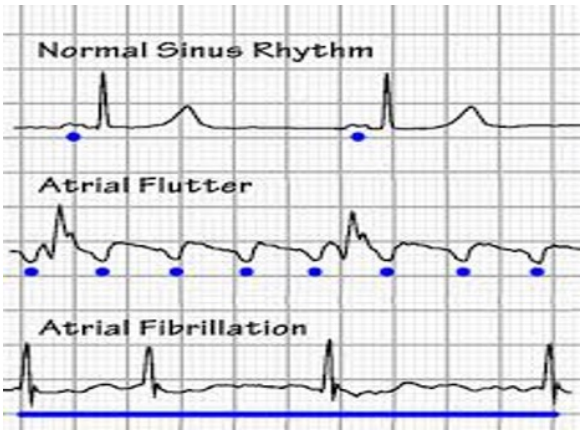

Figure 2.5: Heart arrhythmia [6]

are discussed.

2.2.1 Atrial Fibrillation

Atrial fibrillation (AFib) patients have five times greater risk to get a stroke; however, if AFib is successfully diagnosed, then 75% of all AFib-related stroke can be prevented. As discussed earlier, the heart contracts and relaxes to a regular beat synchronised by the electrical signal in the SA node. In an AFib episode, the atria, the upper heart's chambers, beat in an irregular manner, quiver chaotically and are unable to successfully move the blood into ventricles [31]. During an AFib episode, the rhythm of the atria increases to 250 to 600 bpm, 5-6 times faster than the normal case, and the rhythm is circular and chaotic circular motion. This chaotic beating of the heart can cause weakening to the heart muscle and leads to a failure in pumping the blood adequately. This condition, if left untreated, can cause life threatening conditions. In case a clot breaks off, it can enter the bloodstream. the clot could eventually cause a stroke if it is lodged in an artery leading to the brain. In a study, 15% to 20% of all strokes are attributed to one type of arrhythmia, AFib [14].

Fig. 2.5 shows the difference between the ECG of a normal sinus rhythm and the one from Afib (third ECG signal). In the AFib case, the electrical impulse in the heart is generated in more than one place. With these multiple triggers, the atrium is unable to fully contract and doesn't fully pump the blood to the ventricles. As a result, the

Afib's ECG has multiple small peaks between each R-peak. These peaks or quivers have very small amplitudes which maybe difficult to detect. We are using radar to detect arrhythmia; frequency domain analysis can be used to detect the frequency components of the heart signal and thus recover the rate at which the heart beats. In fact, in the frequency domain representation of the signal in an Afib episode, new low frequency components will be added at 4-12 Hz. However, the radar system is required to have a very good SNR so that the Afib components can be detectable and not buried within the noise floor.

There are three types of AFibs: Permanent, Persistent and intermittent or paroxysmal AFib. As it can be seen from Fig.1.2 permanent AFib happens when a patient is constantly experiencing an arrhythmia episode. In this case, the heart cannot converge back to the sinus rhythm, and patients are required to be on anti-clotting medication for their lifetime to control it. The second type is persistent AFib. It happens when the arrhythmia is experienced more the 80% of the time. Here, the the heart doesn't converge back to the sinus rhythm spontaneously. It is usually treated by medical treatment or cardioversion, electrical treatment, to end the episode. Finally, intermittent AFib or paroxysmal AFib, the heart develops atrial fibrillation and typically converts back again spontaneously to a normal rhythm. This type of Afib is the most challenging type to diagnose because the arrhythmia episode can happen randomly; but it can be as deadly. A person with an intermittent AFib can have an episode that may last from a few seconds to few days which makes it hard to be accurately diagnosed.

Afib is usually diagnosed by different tests:

- Electrocardiogram or ECG - records the heart's electrical impulses.
- Echocardiogram- uses sound waves to map and produce a picture of the heart.
- X-ray- looks for signs of concerning heart issues.
- Advanced imaging- uses CT scans, MRI and ultrasound when needed.
- Stress test- in which doctors check the heart's performance after exercise.

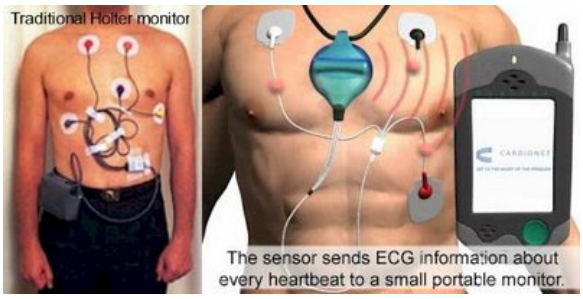

Figure 2.6: Example of a Holter monitor [6]

- Holter monitor- a wearable device to measure and record the heart's electrical signal for a few days, a portable ECG.
- Event monitor- another portable ECG monitor to measure the heart signal for a couple of weeks or months.

ECG, X-ray, ultrasound, and CT scans are the main diagnostic tools used to detect heart arrhythmia. These technologies are very mature and have been widely used in hospitals. However, in most cases, these techniques can only be accessed in hospitals or at doctors' offices, which is not convenient especially for patients living in rural areas. In addition, they are also not comfortable, as they require sticky gels and several probes attached to the body etc. Furthermore, another critical disadvantage of ECG and ultrasound is that they are not suitable for long-term monitoring of intermittent AFib mentioned above. Since the intermittent AFib can last anywhere from a few seconds to a few hours and happens randomly, to be successfully diagnosed with these techniques the patient needs to stay in the hospital for three days or more. The only device existing for this kind of detection is a Holter monitor. A Holter monitor is a battery-operated portable device that measures and records your heart's activity (ECG) continuously for 24 to 48 hours or longer depending on the type of monitoring used [15]. People invented the Holter monitor to diagnose the intermittent Afib; however, as can be seen from Fig. 2.6, it requires many leads attached to the patient's body with sticky gels which makes it not comfortable for the person to be wearing it for a long period of time. Thus, an alternative method needs to be used for cardiac long term monitoring that is not only

accurate but also comfortable for every day use and doesn't interface with the patients' daily activities. One of the technologies that could be used is radar.

2.2.2 Other Arrhythmia

Another type of heart arrhythmia similar to Afib is atrial flutter. In an atrial flutter, the atria, the upper heart's chambers, contract very fast, and result in a fast but usually regular heartbeat rhythm. In this case, the heartbeat is more organised and less chaotic than Afib. Also, atrial flutter rarely persists for months to years. However, sometimes a patient can have both atrial flutter and Afib simultaneously. Patients with this arrhythmia can be asymptomatic, but the problem can still increase the risk of a strokes or other heart complications. In atrial flutter, the atrial beats at a rate of 200-450 bpm, and causes problems with the AV node conduction. In fact, the beat slows down as the signals reach the AV node, a bundle of cells in the upper wall of muscle between the ventricles [31]. A person with this arrhythmia can either show no symptoms or show few symptoms. Some of these symptoms include palpitations, shortness of breath, anxiety and tiredness. Also, patients with heart failure, high blood pressure, or other acute illness have an increased chance of developing atrial failure. The danger of atrial flutter is that it makes it difficult for the blood to be pumped, causing blood clots in the heart which can travel in the blood stream and reach the brain causing heart attacks or strokes.

Fig. 2.5 shows the difference between a normal sinus rhythm and the one from atrial flutter ECG signals. In the atrial flutter case, the middle curve, for each PQRS peak, there are multiple T peaks that follow, instead of only one in a normal ECG signal. In a normal heartbeat, the electrical stimulus signal originates at the upper chambers of the heart, the atria, at the SA node. The stimulus causes the two atria to contract first. Then the electrical signal travels down to cause the heart's ventricles to contract and pump the blood out of the heart. The electrical stimulus starts at the SA node and travels down the atrioventricular node (AV), and slows down for a small period of time and goes down the conduction pathways, explained earlier, into the ventricles. Normally, this stimulus drives the heart to contract about 60 to 100 times in a minute, thus the heart rate. The atria contract for a fraction of a second before the ventricles as they empty the blood

into the ventricles before the ventricles contract. Every ventricle contraction represents one heartbeat. In the case of atrial flutter, the electrical stimulus travels in an organized circular motion pathway within the right atrium of the heart. This motion is referred to as a circuit because it takes an abnormal path through the atria circulating around the tricuspid [32].

Besides atrial flutter and atrial fibrillation, other heart arrhythmia exit, including atrial tachycardia, or atrioventricular nodal reentrant tachycardia (AVNRT). Sometimes it's difficult to differentiate atrial flutter from others. Patients are sometimes given adenosine to transiently slow the ventricular rate to determine the atrial motion and permit an accurate diagnosis. Depending on the the direction of the circular motion in the atria, i.e., the circuit, the atrial flutter can be described as clockwise or counterclockwise. Also, the atrial flutter can be categorised based on the anatomic location where it originated into typical (type I) or atypical (type II). Compared to Afib, atrial flutter is easier to detect. The abnormal beats, in this case, have a larger amplitude which reduces the constraint of the SNR of the system. In fact, using radar, frequency domain analysis can be used to detect atrial flatter without the need for extra circuitry or signal analysis.

2.3 EM Wave Propagation in the Thorax

Radar systems can be used to detect cardiopulmonary signals in contact with a human subject. Radar radiates an electromagnetic (EM) waves to capture the motion of the subject. EM waves suffer from losses and reflections as they travel from one medium to another. Hence, it's critical to find the path of minimum losses on a human chest. When the EM wave is radiated from the antenna of a radar system, it travels through the air, the skin, the superficial fascia, bones and muscles which form the outline of the thorax. It's worth mentioning that in the center of the chest, there is long flat bony plate called the sternum, Fig. 2.7. The sternum connects to the ribs with cartilage. It is part of the rib cage, to protect the heart and lungs from injuries. After the EM wave travels through the bone and muscle layer, it reaches the heart. The heart is composed of three layers: endocardium, myocardium, and pericardium.

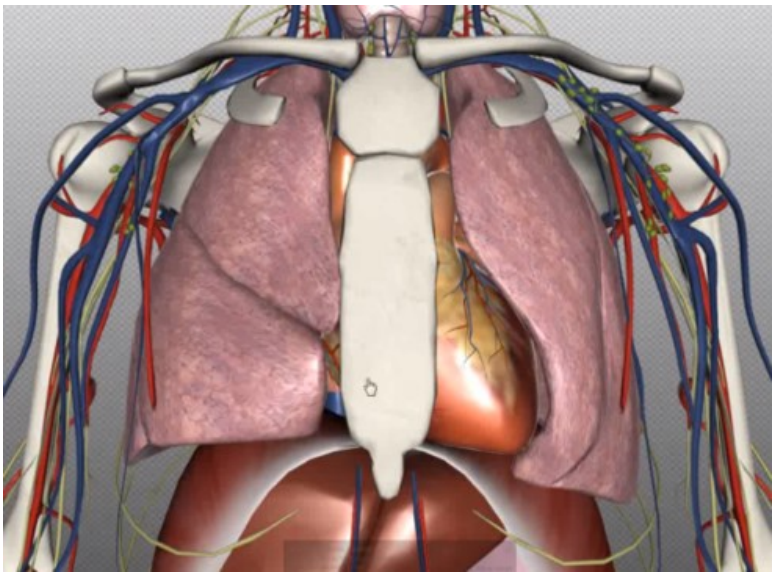

Figure 2.7: Thorax of a human subject showing the sternum [6]

As seen in Fig. 2.8, the EM wave path in the thorax can be modeled to understand the losses contributed by each layer and to find the optimum placement of the radar. The model includes the name and the thickness of each layer. The EM wave has to propagate through skin, superficial fascia (mainly made of fat), muscle (pectoral muscle), bone (ribs) and pericardium of the heart (also mainly made of fat) to reach the heart [7]. This model assumes the wave travels through the ribs. However, if the EM wave travels through the sternum the muscle layer will be omitted. The model can be used to evaluate the important parameters for wave propagation.

This thesis uses a continuous wave radar system. For CW radar, the most important parameter that needs to be considered for the design is the power loss due to reflection and attenuation and not the traveling time of each layer. As illustrated in Fig. 2.9, to minimize the total power loss of the EM wave as it travels through different tissues to the heart, the radar system needs to operate at lower frequency. However, as will be seen later, higher frequency will contribute to better resolution and sensitivity of the radar detector. The trade-off between the sensitivity and power loss is important to determine the optimal operating frequency. In addition to the power loss, noise will also play a major factor choosing the specifications of the radar system. Moreover, the thorax can be

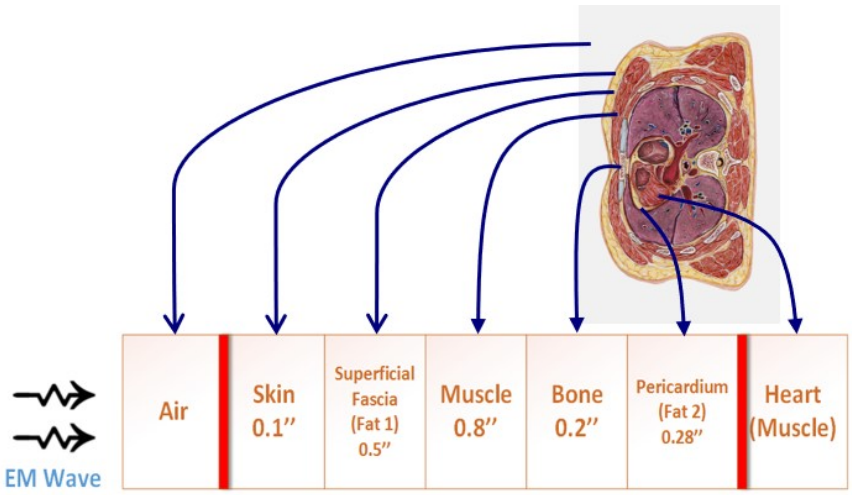

Figure 2.8: 1D Model Of EM Wave Propagation Path In Human Thorax. [7]

modeled as a classical transmission line channel with multiple sections in a CW system. However, to get accurate results, the thickness and dielectric properties of each tissue layer should be known exactly. This can be very challenging; it is not given to even get an approximation of these properties and they can be different from one person to another. Also, this approximation is valid only for low frequencies. Impedance matching can only decrease the reflection power loss, which accounts for only a small portion if the frequency is high [7].

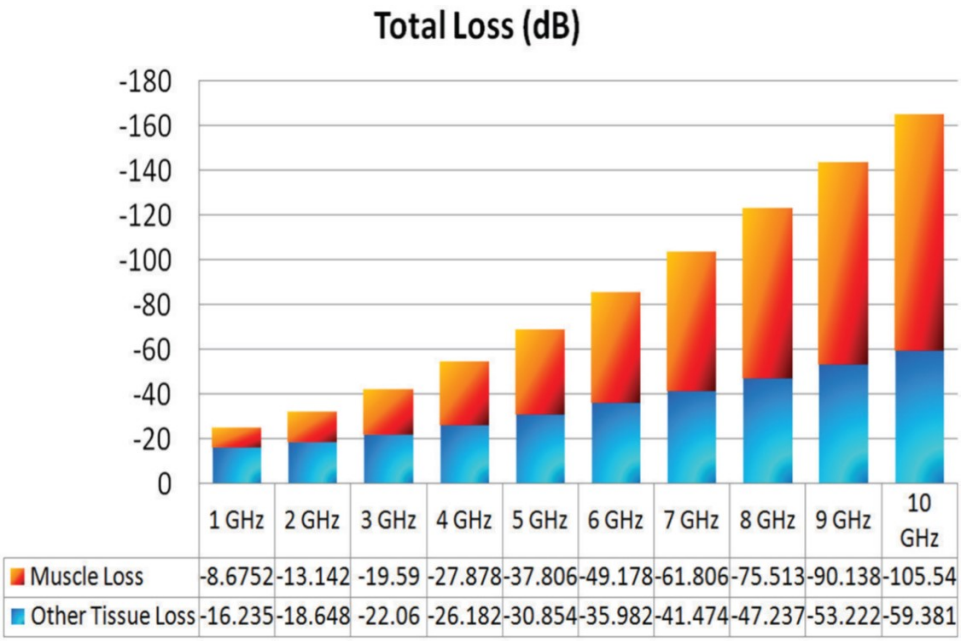

Figure 2.9: Total power loss in different media of EM wave propagation. [7]

Chapter 3

Self-Injection-Locking Radar systems

3.1 Introduction

Radars based on self-injection-locking (SIL) theory was first introduced when thinking of ways of phase noise suppression by injection the received signal back in the oscillator instead of mixing it into the oscillator [8]. The idea was observed by empirical observations of free running oscillators. When a waving hand was moved up and down in the vicinity of a free-running oscillator, the oscillation frequency of this later shifts up and down accordingly. This phenomenon is due to the fact that the oscillator get self-injection-locked to its leakage signal bouncing back from the moving hand, as long as the motion of the hand is within the range of the oscillator, which is much smaller compared to the free-space wavelength Fig. 3.1 . This small change in the frequency is in fact proportional to the hand motion and it's displacement, and can be captured using a frequency demodulator based on the Doppler effect [8].

With this observation was the birth of SIL based radar usage for motion detection and particularly for vital signs detection. In fact, the first demonstrated system to be used for respiratory and heart rate detection was presented in 2010. The idea is to use the voltage-controlled oscillator (VCO) to transmit a continuous-wave signal through the antenna to the subject (human chest). The signal is modulated by the movement of the chest and partially reflected back and injected into the same VCO forming and SIL loop [33]. The demodulation of the Doppler phase shit can provide information about

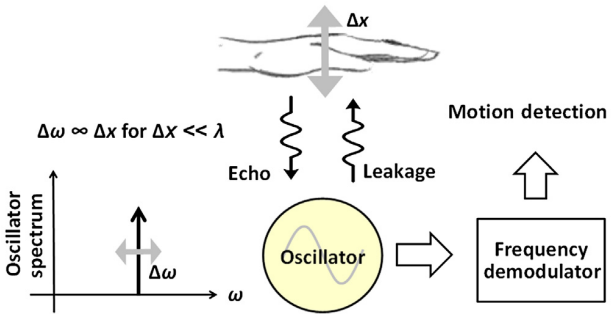

Figure 3.1: SIL effect on a free-running oscillator and its link to motion detection [8].

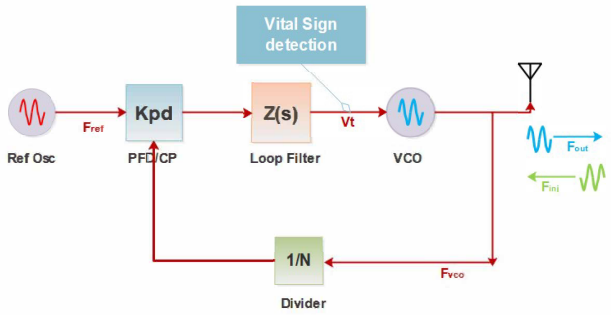

Figure 3.2: Block diagram of the SIL system radar.

the cardio-pulmonary movement of the subject's chest. In [34] [35], a non-contact SIL radar system was demonstrated achieving a long sensing distance without the need for a low-noise amplifier, the sensitivity of the system can increase to a longer rage with the increase of the operational frequency. Also, the null point problem was eliminated by sweeping the frequency. It has been demonstrated that the SIL based radar have a high sensitivity and low complexity and better SNR compared to the traditional radar system.

3.2 Theory

Fig. 3.2 represents a simplified block diagram of the SIL based Doppler radar system of the medical radar chip. The system development is based on a more concise, sensitive

and efficient circuit . The system is based on a phased locked loop (PLL) system that is controlling a voltage-controlled oscillator which achieves self-injection locking (SIL) [36]. This system is more attracting as it consists of a single antenna which saves area and reduces cost and power consumption and eliminates the necessity of a circulator and a noise cancellation path. The radar system radiates power from the VCO through the single antenna, which get modulated by the chest movement due to both respiration and cardiac motion. The reflected Doppler signal is injected back from the antenna to the VCO, which are connected directly to each other to ensure injection locking loop. The PLL demodulate the signal, matching the VCO frequency to the reference frequency through the tuning voltage. This latter is filtered and processed for vital signs measurements extraction. The SIL loop is established when an object is detected. The theory behind the injection locking of an oscillator was first derived in [37]. For an oscillator with a tank resonant frequency of ω_o and has an intrinsic signal of I_o, the Barkhausen oscillation criteria has to be met at all time to sustain oscillation. These criterion are 1. the magnitude of overall gain around the loop should be unity and 2. the overall phase shift around the loop should be either zero or a multiple of 360 degrees. As a matter of fact, if there is any phase shift inserted in the loop, it can no longer oscillate as the to total phase shift deviate from the Barkhausen condition. So, if a VCO is injected by a signal with a magnitude of I_{inj} and an angular frequency of ω_{inj}, it forces the tank of the oscillator to add a phase shift to meet the Barkhausen 2nd criterion and injection locking occurs and the VCO locks at the injection frequency and oscillates at ω_{inj} [38]- [39]. As a result, the instantaneous output signal from the VCO can be derived from vector analysis as shown in Fig. 3.3. When the VCO is phased locked, the output voltage V_{out} and I_{inj} will have a phase difference because the tank contributes a phase of ϕ_o forcing V_{out} to rotate with respect to I_R with the angle ϕ_o, while being still in phase with I_o. If the instantaneous output has a magnitude of I_R, it can be derived as the sum of I_{inj} and I_o. It has been shown in [38] that the relationship between ϕ_o and ϕ, the phase shift introduced to the system, as

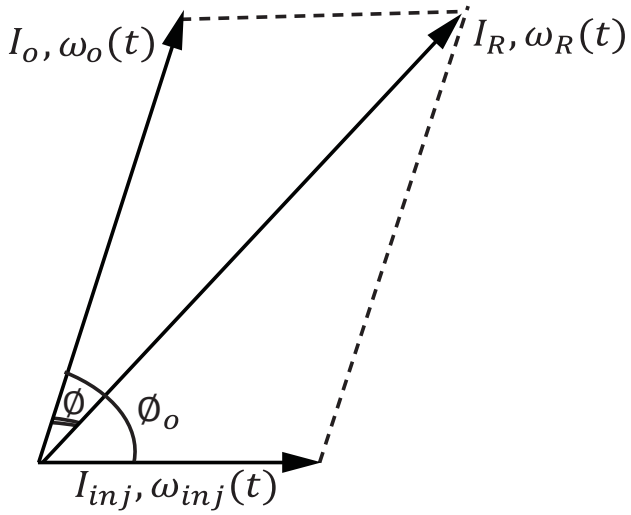

Figure 3.3: Vector diagram of the instantaneous current signals in the SIL oscillator.

$$\sin(\phi) = \frac{I_{inj}}{\sqrt{I_{inj}^2 + I_o^2 + 2I_{inj}I_o\cos(\phi_o)}}\sin(\phi_o), \tag{3.1}$$

Under weak injection approximation, the locking range of the oscillator is expressed in [37] as

$$\omega_{LR} = \frac{\omega_o I_{inj}}{2QI_o} \tag{3.2}$$

where Q id the quality factor of the VCO resonant tank. Equation 3.2 is famously known as Adler's equation for locking range under weak injection. When the SIL oscillator phase is locked,

$$\omega_{out} = \omega_{inj} = \omega_o - \omega_{LR}\cos(\phi(t)) = \omega_{syn}, \tag{3.3}$$

where ω_{LR} is one-sided locking range, $\phi(t)$ represents the free-space round-trip and circuit delays and ω_{syn} is the PLL synthesized frequency [40]. ω_o is determined by the tuning voltage of the oscillator and can be represented as,

$$\omega_o = \omega_{syn} + K_{vco}\Delta V_T, \tag{3.4}$$

where K_{vco} is the VCO gain with respect to the tuning voltage. The reflected Doppler signal directly injected into the VCO produces a variation of the tuning voltage $\Delta V(t)$. Since ω_{out} and ω_{inj} remain constant when the SIL oscillator is in a steady state,$\Delta V(t)$ can be derived,

$$\Delta V(t) = \frac{\omega_{LR} \cos(\phi(t))}{K_{vco}}, \tag{3.5}$$

The equation above gives an insight of how the tuning voltage of the PLL varies with the modulation established by the heart movement; but can't relate the heart position changes to the later. Equation 1 also gives an insight that for better sensitivity the K_{vco} should be reduced and the ω_{LR} should be increased. To get a better sense of how the tuning voltage changes with the heart displacement, a different approach of derivation is made.

3.3 Literature Review

In [41], a SIL radar system operating at a frequency of 2.4 GHz ISM band for detecting hidden people through walls by detection the respiration signal. The system uses two antennae as well as an LNA and PA, while the frequency demodulator consists of a mixer, a delay element and a low pass filter in addition of digital signal processing (DSP) unit to extract the position information. The system, however, was only able to detect the respiratory rate and slow body motion but not the heart rate and the circuitry is complicated. In [36], the sensitivity of the later system was improved by using frequency-modulated continuous-wave (FMCW) and sum-difference pattern detection approaches to determine the distance and azimuth from the radar to each subject behind the wall and a two element phase array antenna for the receiver end.

While [42] [43] [44] demonstrated a SIL radar system consisting of a SIL tag carried by the subject and a group of Injection-locked I/Q receivers to demodulate the RF signal and extract the vital signs of multiple subjects carrying the tag using frequency division multiple access operating at 2.4 GHz. The main problem with the system is that the receiver is required to be stationary during the signal acquisition, and if not, some of the signal with the doppler shift will be transmitted back to the tag module and cause some

interference.; which made it hard to detect the heart-rate. In [45], radar system proposed is a bistatic with a single-input multiple-output (SIMO) self-injection-locked oscillator tag attached to the subject's torso while the receiver is handheld at a remote location. The tag uses a circularly polarized antenna and a polarization-diversity CP array antenna for transmitting the tag's output signal to reduce the moving clutter resulted from the receiver, which caused an interference to the tag module. Although, this system improves the heart-rate detection, the signal is still weak, and more circuitry is needed, in addition, the power consumption in the tag is significant and is vulnerable to the body proximity effect.

Other systems used different approaches to reduce the clutter issue. While [46] tries to reduce the interference from the moving clutter and body proximity using a frequency selective surface (FSS) and an electromagnetic bandgap (EBG) surface by placing them on the front and back side of the tag antenna. The usage of artificial meta-surfaces (MTM) has increased in recent years. In fact, while the FSS, used as a directivity enhancer or a polarization converter, is a resonant structure [28], the EBG surface can ve considered as a perfect magnetic conductor and provide an in-phase reflection for an incident wave, which can reduce the effect of body proximity. These MTSs are very useful in the development of wearable sensors for vital-sign sensing applications. However, the system is very bulky, power hungry and the sensitivity is low. [47] uses an MTM based leaky wave antennae with SIL radar non-contact sensor for multi subject vital signs detection. the vital sign signals are obtained by converting the output signal of MTM LWA to RF signals with frequency dependent amplitude variance, using a first-order differentiator followed by an envelope detector [48].

In [49], the SIL radar system uses a phased-lock loop (PLL) as a demodulator to extract the vital sign information by directly sampling the VCO's tuning voltage for a non-contact sensor. In [40], the system was improved by using two antennae and a circulator with a path-diversity transmission block to provide two orthogonal paths to eliminate the null point and reduce the DC offset problem with a dual tuning VCO. The system was implemented with off-shelf components at 2.4 GHz. But the sensitivity was not very high

as the heartbeat signal was still very weak unlike the respiration signal, also, the system is very complicated which makes it the unpractical for healthcare applications. [50] reduces the SIL radar system to a single antenna connected directly to the VCO and eliminate the need of a circulator, but the heart-beat signal is still very weak. [51] implemented the SIL radar system in 65nm CMOS process to reduce the size and operating at 5.8 GHz with a dynamically time-frequency multiplexed operation [52] to avoid null point. Although the respiration rate was detectable at a distance of 4 meters, the hear-rate signal was very weak and hardly differentiated from the noise floor.

Other attempts were used to reduce the need of having two separate antennae for the transmitting and receiving ends. For instance, [53] uses an RF circulator in a monostatic radar based on a six-port interferometer to prevent the transmitter deteriorating the received weak Doppler signal at 24 GHz in a non-contact vital sign detector. Moreover, [54] also uses a PLL as a demodulator for the SIL based radar system for non-contact vital sign measurement, however instead of VCO, it uses a self-oscillating active-integrated-antenna (AIA). The AIA radiates the RF power to the chest and receives the modulated signal for vital signs extraction through the tuning voltage of the oscillator. The AIA is consisted of two-port circular patch antenna that is used to act as a frequency-selective element for the oscillator design and also radiate the RF signal into the subject chest. Although the system reduces the circuit complexity and cost, the sensitivity can be improved better.

The work in [55] uses a single conversion stepped-frequency continuous-wave (SCS-FCW) SIL radar to try to improve the sensitivity and range resolution for multiple subjects. But the system requires two antennae and requires both an LNA and PA in the system. Moreover, in [56], a non-contact SIL radar system was used at 24 GHz frequency. It uses an injection-locked frequency divider (ILFD) based on the push-push oscillator topology instead of the conventional VCO. The sensitivity of the system increase, as the operation frequency is higher, and uses a differentiator and envelope detector for demodulation and vital signs extraction. However, the system uses two antennae and have a shorter detection range and low efficiency in the conversion of frequency to amplitude modulation, especially that the modulation is off chip. Other SIL radar system uses a

more complex circuitry to reduce body motion artifact using two VCOs instead of one mutually injection locked to each other [57], with branch-line coupler and a circulator array [58], or a single VCO to transmit and re-transmit a continuous wave to the opposite sides of a human body to detect vital signs using circulators and a power splitter [59].

Chapter 4

SIL PLL based transceiver

4.1 Introduction

For the system development of the Medical radar chip, a more concise circuit is used. The circuit is based on a phased locked loop system that is controlling a voltage-controlled oscillator which achieves SIL. This system is more appealing because it consists of a single antenna which saves area and reduces cost and power consumption and eliminates the necessity of a circulator. The chip radiates power from the VCO through the single antenna, which get modulated by the heart movement. The reflected Doppler signal is injected back from the antenna to the VCO, which are connected directly to each other to ensure injection locking loop.The PLL demodulate the signal, matching the VCO frequency to the reference frequency through the tuning voltage. This latter is filtered, digitized and processed for vital signs measurements. All work done so far in the SIL single radar chip uses an LC tank based VCO ans suffers from a limited sensitive range. Another VCO architecture that can be used is a ring oscillator. LCVCOs have a superior phase-noise performance with a low power consumption. However,they have a lower tuning range compared to the ring oscillators. Also, for the LCVCOs, the phase-noise is strongly dependent on the quality factor of he on-chip inductor. Ring oscillators are avoided because of their worst phase noise than the LCVCOs. However, in this application, the phase noise is not of a major concern, as it will explained in this chapter. In fact, a study of the preference of using the LCVCO and Ring VCO (RVCO) will be

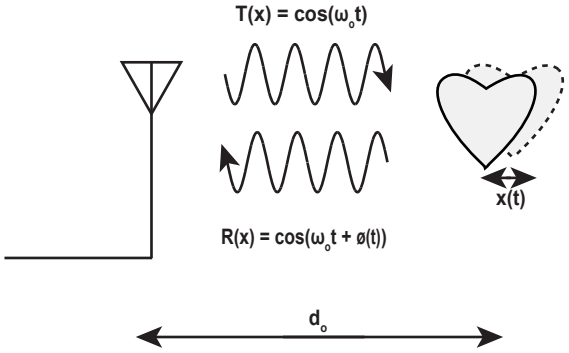

Figure 4.1: SIL transcieved signal to the heart.

presented. Although the LCVCO has many advantages over the RVCO, this later is shown to have a better sensitivity for motion detection.

4.2 Sensitivity study

4.2.1 LC Voltage Controlled Oscillator

In Fig. 4.1, a radar transmitter generates a continuous wave. After the transmitted signal is reflected by the target and the clutter around it, the received signals can be written as,

$$R(t) = \cos\left(\omega_o(t) - \theta - 4\pi\left[\frac{d_o + x(t)}{\lambda_o}\right]\right), \tag{4.1}$$

where ω_o is the oscillation frequency of the transmitted signal, θ is the phase shift from the reflection surface, λ_o is the wavelength at ω_o, and $x(t)$ represents the small displacement of the heart. The phase shift can be defined as

$$\phi(t) = \theta - 4\pi\left[\frac{d_o + x(t)}{\lambda_o}\right]. \tag{4.2}$$

Using Adler's equation, for injection locking [37], the change in frequency can be expressed as

$$\Delta\omega(t) = \sqrt{\frac{P_i}{P_o}}\frac{\omega_o}{2Q}\sin\left(\phi(t)\right), \tag{4.3}$$

where Q is the quality factor of the VCO, P_i is the injected power, and P_o is the radiated power from the VCO. Substituting (4.2) in (4.3), we find that the change in the angular

frequency can be written as

$$\Delta\omega(t) = \sqrt{\frac{P_i}{P_o}}\frac{\omega_o}{2Q}\sin\left(\theta - 4\pi\left[\frac{d_o + x(t)}{\lambda_o}\right]\right), \tag{4.4}$$

For the heartbeat motion, $4\pi x(t) << \lambda_o$, i.e. the heart displacement during the cardiac cycle is very small compared to the wavelength; therefore, using the small angle approximation

$$\sin(a+b) = \sin(a) + b\cos(a), \tag{4.5}$$

where $a = \theta - 4\pi\left[\frac{d_o}{\lambda_o}\right]$ and $b = -\left[\frac{4\pi}{\lambda_o}\right]x(t)$. Then, the Adler equation (4.4) becomes,

$$\Delta\omega(t) \approx \left[\frac{4\pi}{\lambda_o}\right]\sqrt{\frac{P_i}{P_o}}\frac{\omega_o}{2Q}\cos\left(\theta + \left[\frac{4\pi d_o}{\lambda_o}\right]\right)\Delta x(t) \tag{4.6}$$

The frequency sensitivity of a VCO is defined as,

$$K_{VCO} = \frac{\Delta f}{\Delta V_T} = \frac{\Delta\omega}{2\pi\Delta V_T} \tag{4.7}$$

which implies that,

$$\Delta\omega = 2\pi\Delta V_T K_{VCO}. \tag{4.8}$$

Substituting the frequency sensitivity in equation (4.6) implies that

$$2\pi\Delta V_T K_{VCO} \approx \left[\frac{4\pi}{\lambda_o}\right]\sqrt{\frac{P_i}{P_o}}\frac{\omega_o}{2Q}\cos\left(\theta + \left[\frac{4\pi d_o}{\lambda_o}\right]\right)\Delta x(t), \tag{4.9}$$

After simplification, equation (4.9) becomes

$$\frac{\Delta V_T}{\Delta x(t)} \approx \left[\frac{2}{\lambda_o}\right]\sqrt{\frac{P_i}{P_o}}\frac{\omega_o}{2QK_{VCO}}\cos\left(\theta + \left[\frac{4\pi d_o}{\lambda_o}\right]\right), \tag{4.10}$$

or,

$$\frac{\Delta V_T}{\Delta x(t)} \approx \left[\frac{2}{\lambda_o}\right]\frac{\omega_{LR}}{K_{VCO}}\cos\left(\theta + \left[\frac{4\pi d_o}{\lambda_o}\right]\right), \tag{4.11}$$

where ω_{LR} is the frequency locking range and is defined as $\sqrt{\frac{P_i}{P_o}}\frac{\omega_o}{2Q} = 2|\Delta\omega_o|_{max}$. The sensitivity of the system can then be expressed as,

$$\frac{\Delta V_T}{\Delta x(t)} \propto \frac{\omega_{LR}}{K_{VCO}}\frac{2}{\lambda_o}, \tag{4.12}$$

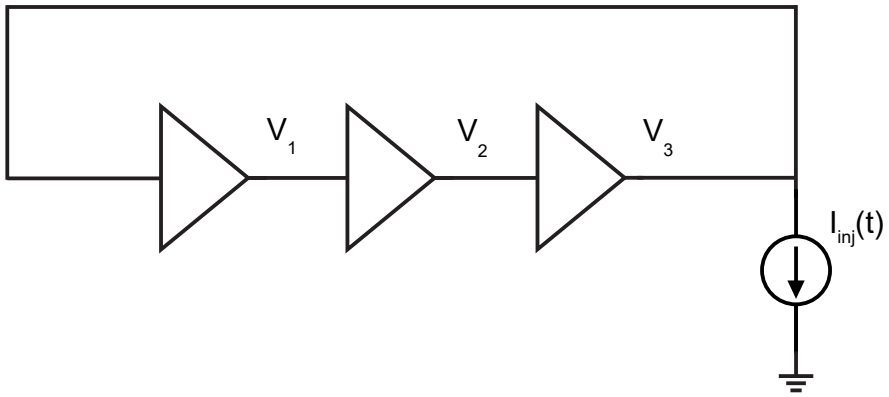

Figure 4.2: 3-Stage ring VCO.

Equation (4.12) becomes, after substituting $\lambda_o = 2\pi c/\omega_o$, where c is the speed of light,

$$\frac{\Delta V_T}{\Delta x(t)} \propto \frac{\omega_{LR}}{K_{VCO}} \frac{\omega_o}{\pi c} \propto \frac{1}{QK_{VCO}} \frac{\omega_o^2}{\pi c}, \tag{4.13}$$

Equation (4.13) provides an evaluation of the degree of sensitivity of the SIL radar system. It is safe to conclude that for better sensitivity of vital signs detection, K_{VCO} should be minimized while maximizing ω_{LR}, or Q should be minimized while maximizing ω_o, which agrees with Equation (3.5).

4.2.2 Ring Voltage Controlled Oscillator

The derivation of the sensitivity of the RVCO is similar to that of the LCVCO. However, while ω_{LR}, the locking range frequency, and Q, the quality factor of the LCVCO is very well known, understood and clearly defined, that of the RVCO is not. Also, most of the work presented before emphasizes a 3-stage RVCO. In this section, I will include the work already done for the 3-stage RVCO, and present my derivations for the 4-stage RVCO that will be used in the design.

4.2.2.1 3-Stage Ring VCO

For the Ring oscillator, equation 4.13 can also be applies, but the Q of the oscillator is not obvious and need to be determined.According to [60]- [61], based on the Perturbation Projection Vector (PPV), for more information see appendix A, the voltage at the output

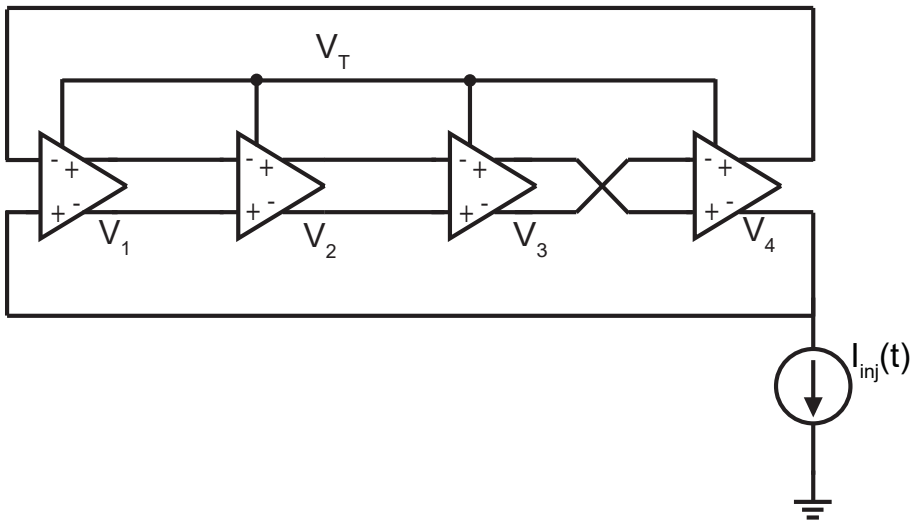

Figure 4.3: 4-Stage ring VCO.

node of a 3-stage ring oscillator can be expressed as,

$$V_3(t) = \begin{cases} \frac{1}{\sqrt{5}} I_o e^{(t/\tau)} & if 0 \leq t < \frac{\tau}{t} \\ I_o(\frac{2}{\sqrt{5}} - 1)e^{(t/\tau)} & if \frac{\tau}{t} \leq t < T \end{cases} \tag{4.14}$$

where I_o is the current at the output of the oscillator. With a sinusoidal injection $I_{inj} = I_i \cos(\omega_{inj} t)$, we can solve for when the VCO is locked, ie. $\frac{d\Delta\phi}{dt} = 0$,

$$\begin{aligned} \Delta\omega(t) &= 0.6773 \frac{R I_i \omega_o}{V} \cos(\phi(t) + 0.1446) \\ &= 0.6773 \frac{I_i \omega_o}{I_o} \cos(\phi(t) + 0.1446), \end{aligned} \tag{4.15}$$

The locking range is when $\Delta\omega(t)$ is maximum; $\omega_{LR} = 0.6773 \frac{I_i \omega_o}{I_o}$. We can apply the same derivation as above and so the sensitivity of the system can be expressed as,

$$\frac{\Delta V_T}{\Delta x(t)} \approx \left[\frac{2}{\lambda_o} 0.6773 \frac{I_i \omega_o}{I_o} \lambda_o \right] \cos\left(\theta + \left[\frac{4\pi d_o}{\lambda_o} + 0.1446 \right] \right), \tag{4.16}$$

4.2.2.2 4-Stage Ring VCO

Using the PPV method, the same approach has been carried to drive the output voltage expression at the output stage of the ring oscillator (the derivation is included in the

appendix B),

$$V_4(t) = \begin{cases} 3.8592 I_o e^{(t/\tau)} & if 0 \leq t < \frac{\tau}{t} \\ (-4.05) I_o e^{(t/\tau)} & if \frac{\tau}{t} \leq t < T \end{cases} \tag{4.17}$$

Where I_o is the current at the output of the oscillator. With a sinusoidal injection $I_{inj} = I_i \cos(\omega_{inj} t)$, we can solve for when the VCO is locked, ie. $\frac{d\Delta\phi}{dt} = 0$,

$$\begin{aligned} \Delta\omega(t) &= 0.6112 \frac{R I_i \omega_o}{V} \cos(\phi(t) + 0.446) \\ &= 0.6112 \frac{I_i \omega_o}{I_o} \cos(\phi(t) + 0.446), \end{aligned} \tag{4.18}$$

The next step is to map the result obtained for the locking range of the RVCO and obtain a value for the Q as a comparison to the LCVCO. Table 4.1 summarizes the results.

In literature, different approaches have been made to estimate the Q of the ring oscillator. Table 4.2 summarizes the different approaches for the locking range, LR, in literature. The table also details the LR results for three and four stages and the Q calculated after the mapping. The LR result calculated in this paper agrees with the ones published. It can be concluded from the different locking range calculations that the LR of the RVCO is a function of the Q, which in turn is a function of the number of stages in the ring oscillator.

Table 4.1: Q of both LCVCO and RVCO from the locking range equations

LC VCO	Ring VCO
Locking range	Ring Locking range (PPV Method)
$\omega_{LR} = \frac{I_i}{I_o}\frac{\omega_o}{Q}$	$\omega_{LR} = 0.6112\frac{I_i\omega_o}{I_o} = K\frac{I_i\omega_o}{I_o}$ In Comparison with the LC: $Q = \frac{1}{K} = \frac{1}{0.6112} = 1.636$
Better sensitivity: small Q and K_{VCO}	Better sensitivity: small Q and K_{VCO} Q,in this case is small

Table 4.2: Literature comparison for different locking rage approaches and the corresponding Q

LR derivation		$N=3$		$N=4$
	$\frac{\omega_{LR}}{\omega_o}$	Q	$\frac{\omega_{LR}}{\omega_o}$	Q
$\frac{I_i}{NI_o}\frac{1}{\tan\left(\frac{\pi}{N}\right)}$	0.0096	5.2	0.0125	4
$\frac{I_i}{NI_o}\frac{2}{\sin\left(\frac{2\pi}{N}\right)}$ [62]	0.0385	1.299	0.0250	2
$\frac{I_i}{I_o}\frac{1+\tan\left(\frac{\pi}{N}\right)^2}{N+\tan\left(\frac{\pi}{N}\right)*\left[\sqrt{1-(\frac{I_i}{I_o})^2}\right]}$ [63]	0.0384	1.2974	0.0251	1.9975
$\frac{I_i}{I_o}\frac{1+\tan\left(\frac{\pi}{N}\right)^2}{N+\tan\left(\frac{\pi}{N}\right)*\left[\sqrt{1-(\frac{I_i}{I_o})^2}-\tan\left(\frac{\pi}{N}\right)\frac{I_i}{I_o}\right]}$ [64]	0.0422	1.1849	0.0264	1.8975
$\frac{I_i}{NI_o}\frac{1}{\omega_o C R_L}$ [65]	0.025	2	0.2117	2.6318
PPV Model: $K\frac{I_i}{I_o}$	0.03386 [60]	1.4765	0.03056	1.6361
Razavi Derivation [66]	–	$\frac{3\sqrt{3}}{4}=1.3$	–	$\sqrt{2}=1.414$

4.3 Sensitivity

4.3.1 LCVCO and Ring Oscillator comparison

Equations (4.13) shows the sensitivity equation of the LCVCO and the RCVCO. It can be concluded that the sensitivity of the system is function of the operation frequency, the Q and the K_{VCO} of both oscillators. If both oscillators operate at the same frequency, where,

$$\frac{\Delta V_T}{\Delta x(t)} \propto \frac{\omega_{LR}}{K_{VCO}} \propto \frac{1}{Q * K_{VCO}}, \tag{4.19}$$

then to compare which oscillator would have a better sensitivity, we should compare their Q and K_{VCO}. The LCVCO's quality factor, Q, can be higher depending on the tank LC, while the RVCO's Q depends on the number of stages in the oscillator. The RVCO's Q is typically very small $1 \sim 3$ for different stages, in fact even for an $N = 999$ VCO, the Q, using different derivations from the table above, will not exceed a value of about 3.1,

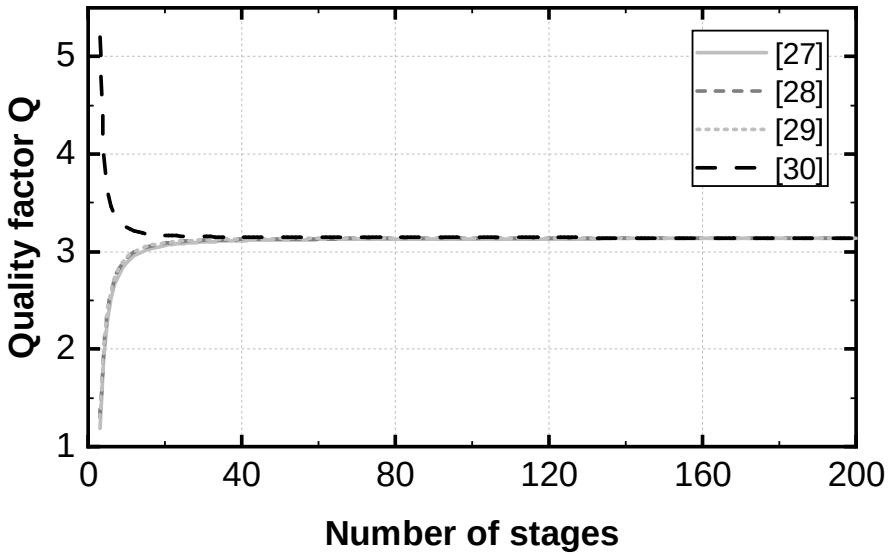

Figure 4.4: The Q of the ring oscillator versus the number of stages.

as it can be seen in Fig 4.4. For better sensitivity, if all other parameters are the same, a smaller K_{VCO} and a smaller Q are needed. The latter is inherent for the RVCO. Thus, the RVCO exhibits a better sensitivity compared to the LC with the same K_{VCO}.

4.3.2 Phase Noise And SNR Of The SIL Radar System

Next, to have a better understanding of the SIL Radar performance, the phase noise and signal to noise ration need to be investigated. The phase noise and SNR of the SIL system is derived by analyzing the loop Laplace domain. Fig. 4.5 shows the block diagram for the linear model for the SIL loop in frequency domain with all possible noise sources. In Fig. 4.5, $\phi(s)$ is the Laplace transform of $\phi(t)$ in 4.2, which represents the heart motion information. $\phi_{ref}(s)$, $\phi_o(s)$ and i_{CP} are the Laplace transform of the phase noises introduced but the reference oscillator, the VCO and the charge pump respectively. $Z(s)$, $K_{VCO}(s)/s$ and K_{PD} are the transfer functions of the loop filter, the VCO and charge pump and PFD gain respectively. The injected phase to the loop from the Doppler phase shift is controlled by $G_{inj}(s)$ and $T(s)$, since the SIL system can be represented as a delta-sigma modulator [40] [67]; $G_{inj}(s) = \omega_{LR}\cos\phi/s$ is the transfer function of the

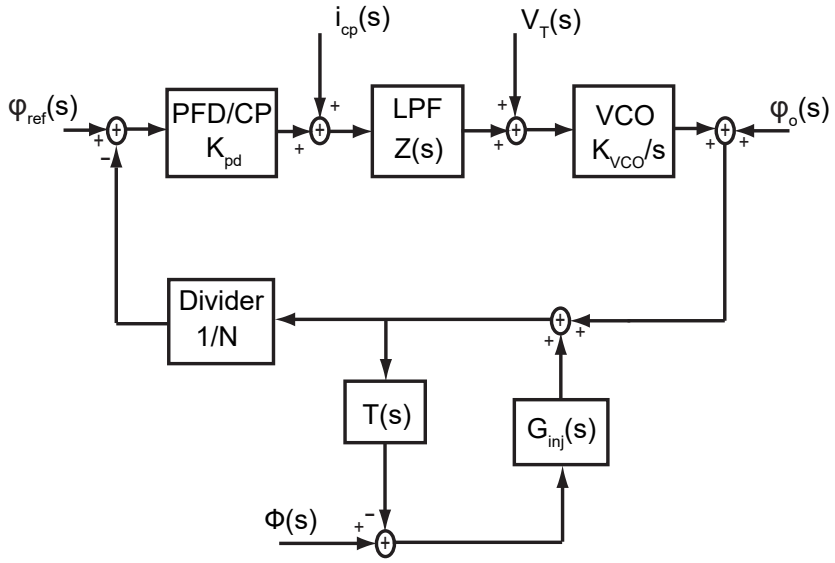

Figure 4.5: Phase noise block diagram of the linear model of SIL Radar system.

injection phenomenon and $T(s) = 1 - \exp(-s\tau_d)$ is the transfer function of the round-trip propagation with a τ_d delay. Previous work has investigated the SNR performance of an SIL based- vital sign detection. In both [67], where the SIL demodulator is a delay and a mixer, [67] and [40], where a PLL is used as a demodulator, the SNR gain is derived. The SNR gain is the ratio of the SNR before and after delta-sigma process and the SIL radar system has an SNR gain compared to any free running phase-locked oscillator and is derived as

$$G_{SNR}(s) = |\frac{\omega_{LR}\cos\phi}{s}|^2 \propto |\frac{\omega_o\cos\phi}{Qs}|^2. \tag{4.20}$$

Higher SNR gain can be achieved by increasing ω_{LR} or decreasing Q and increasing ω_o. It is worth noting that this also improves the sensitivity of the SIL system. It was found that at a rate of 20 dB the SNR gain improved with decreasing modulation frequency ω_o. Also, according to [68], the SNR performance of the SIL system is not influenced by the clutters. For our application, the vital signs measurement's bandwidth required is minimal, less than 20 Hz, making the SNR gain high. Also, the in-band phase noise of the locked oscillator is dominated by the reference crystal oscillator and the $1/N$ divider, which makes using a PLL as a demodulator for the SIL system advantageous in terms of

the phase noise factor.

4.3.3 SIL Radar System Design Consideration

In summary, SIL based Radar system can be successfully used to capture motion in general and vital signs specifically. For vital sign measurements, the breathing and heart beat movements need to be detected in the torso of a human subject. The SIL based detection system is based on the Doppler radar principal. From the derivation above, to design an SIL radar sensor, one needs to consider the sensitivity, phase noise and SNR. Equation (4.13) gives an insight of the sensitivity of the SIL radar system. to achieve a higher sensitivity, the K_{VCO} needs to be decreased and ω_{LR} should be increased, or Q should be decreased. Also, the higher the operation frequency, the sensitivity is improved by the power of 2. The K_{VCO} is the gain of the VCO which can be designed for when designing the oscillator circuit. The locking-range and the Q is also specific to the VCO, where the definition can vary for different type of oscillators. Also, a higher SNR gain can be achieved by increasing ω_{LR}, or decreasing Q and increasing ω_o. Also, the SNR gain is much higher for the small modulation frequency caused by chest motion for vital signs measurement. In addition, using a PLL for demodulation, the in-band phase noise of the locked oscillator can be minimized to achieved better result, as it will be discussed in the next section.

4.3.4 Phase Noise Study

4.3.4.1 LCVCO

Generally, Leeson's Equation [69] is widely used for estimating phase noise for LCVCOs.

$$\mathcal{L}(f) = 10log\left[\frac{1}{2}[(\frac{f_{VCO}}{2Q_L f})^2 + 1] * [\frac{f_{1/f^3}}{f} + 1] * [\frac{FkT}{P}\right] dBc/Hz, \tag{4.21}$$

where f is the offset frequency, F is the noise figure of active device, T is the temperature, P is the input power, k is Boltzmann's constant, f_{VCO} is the VCO frequency, Q_L is the loaded quality factor of the tank inductor and f_{1/f^3} is the $1/f^3$ is noise (flicker noise) corner frequency. To make the Leeson equation more complete, the tuning diode contribution should be added [70]; therefore, 4.21 becomes,

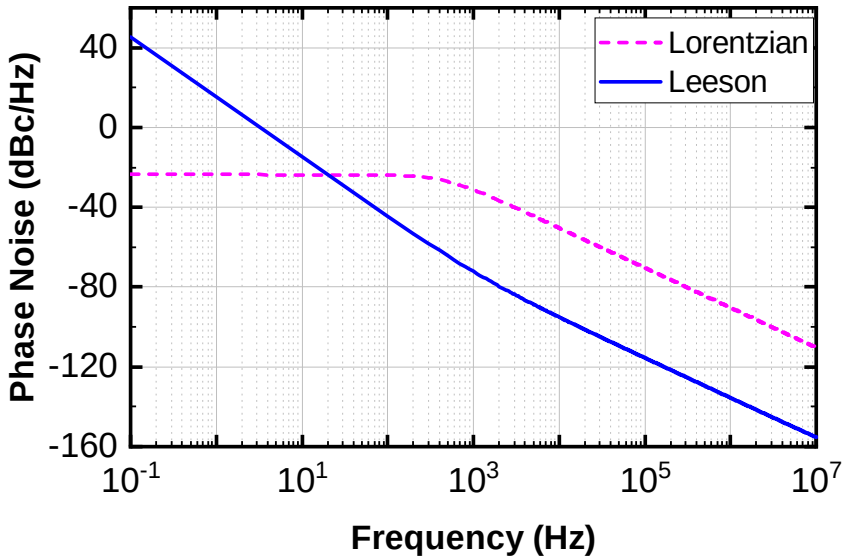

Figure 4.6: Phase noise comparison between Leeson's and Lorentzian model.

$$\mathcal{L}(f) = 10log\left[\frac{1}{2}[(\frac{f_{VCO}}{2Q_L f})^2 + 1] * [\frac{f_{1/f^3}}{f} + 1] * [\frac{FkT}{P} + \frac{2kTR_{var}K_{vco}^2}{f^2}\right] dBc/Hz, \quad (4.22)$$

In fact, Leeson's equation focuses on higher frequency offset and tend to approach infinity at very small offset frequencies and has asymptotic behavior. This outcome suggests that the VCO can have an infinite output power, which makes the model incorrect and that the phase noise can be greater than 0. This is due to that fact that the VCO is assumed to be linear at the steady state point [71]. It can be noted from the phase noise equation that the phase noise can be reduced if the Q is increases and the K_{VCO} is reduced. However, in this application, the heart and respiration of a human body happens at a very low frequency; it does not exceed 3 Hz. As a result, Leeson's model won't be very useful for this. In fact, for low frequency offset phase noise estimation, a different equation is used; the Lorentzian Function with is the Lorentzian spectral width [72].

$$\mathcal{L}(f) = 10log\left[\frac{2f_{3db}}{f_{3db}^2 + f^2}\right] dBc/Hz, \quad (4.23)$$

where,

$$f_{3db} = \frac{FkT}{P}(\frac{f_{VCO}}{2Q_L f})^2 \tag{4.24}$$

Fig. 4.6 shows the phase noise comparison between Leeson's and Lorentzian model. The main comparison is at low frequencies, around 1 Hz, the frequency of interest in this project. In fact, it shows that using the Lorentzian model makes more sense in terms of phase noise, because the Leeson's model gives us a positive phase noise which does not make sense. The figure also shows that this Lorentzian model is valid only up to the f_{3db} frequency, beyond that the Leeson's model is what valid.

In this case, K_{VCO} won't affect the phase noise, but the Q is still a big factor of the phase noise.Therefore, the trade-off in the design for the resonator Q for sensitivity and phase noise. However, since the PLL will filter out the phase noise of the VCO at the low frequencies, the value of the Q should be considered to increase the sensitivity of the system.

4.3.4.2 RVCO

The RVCO is very known for its worst phase noise. The Q of RVCO is poor because the energy stored in the node capacitances is discharged at every cycle. Also, the energy is restored to the resonator during the edges which is the worst time rather than at the voltage maxima [73]. However, this issue is not a big concern in this application, because a PLL is used and it will clean up the spectrum.

Unlike the LCVCO, there is not one equation that can be used to estimate the phase noise for all ring oscillators; but it will depend on the architecture of the delay element the ring oscillator, is it single-ended or deferential and the number of stages used. For a differential ring oscillator, with a simple inverter based delay element, Fig. 4.7, the differential flicker noise [74] can be expressed as,

$$\mathcal{L}(f) = \frac{K_f}{WLC'_{ox}} \left(\frac{1}{V_{effd}^2} \right) \frac{f_o^2}{f^3} \tag{4.25}$$

where f is the offset frequency, f_o is the VCO frequency, V_{effd} is the effective gate voltage on the differential pair at balance [9], and W, L are the width and length of the current source i the delay cell. While the white noise is,

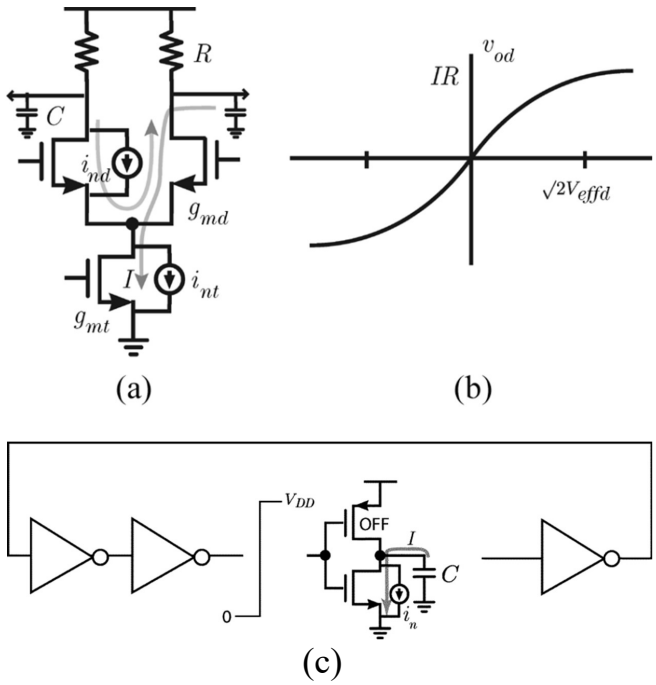

Figure 4.7: (a) Differential delay element with noise currents. (b)Input–output characteristic of differential pair. (c) Single ended ring oscillator with delay element and its noise currents [9].

$$\mathcal{L}(f) = \frac{2\mathrm{kT}}{I \ln 2}\left[\gamma\left(\frac{\frac{3}{4}}{V_{effd}} + \frac{1}{V_{efft}}\right) + \frac{1}{V_{od}}\right]\left(\frac{f_o}{f}\right)^2 \tag{4.26}$$

where V_{od} is the differential output voltage, f_o is the VCO frequency, T is the temperature, I is the current through the delay cell, γ is the transistor's noise factor, V_{efft} is the effective gate voltage on the current source transistor and k is Boltzmann's constant. On the other hand,for a single ended ring oscillator, with a simple inverter based delay element,figure 4.7, the flicker noise [74] can be expressed as,

$$\begin{aligned}\mathcal{L}(f) &= \frac{1}{4N(V_{\mathrm{DD}} - V_t)^2}\left(\frac{K_{fN}}{W_N L_N} + \frac{K_{fP}}{W_P L_P}\right)\left(\frac{f_o^2}{f^3}\right) \\ &= \frac{C'_{ox}}{8NI}\left(\frac{\mu_N K_{fN}}{L_N^2} + \frac{\mu_P K_{fP}}{L_P^2}\right)\left(\frac{f_o^2}{f^3}\right)\end{aligned} \tag{4.27}$$

where $K_{fN} \approx 10^{-24}$ is an empirical coefficient independent of bias, fabricator and tech-

nology for NMOS, K_{fP} is defined similarly for PMOS but is lower and depends on bias. To estimate the upper limit on the effects of flicker, noise can be estimated by setting $K_{fN} = K_{fP}$ [74]. N is the number of stages used in the ring oscillator, W_n, L_n, W_p and L_p are the widths and lengths of the NMOS and PMOS transistors of the delay cell. Further, the phase noise due to white noise for the single-ended ring oscillator can be expressed as

$$\mathcal{L}(f) = \frac{2\mathrm{kT}}{I}\left(\frac{1}{V_{\mathrm{DD}} - V_t}(\gamma_N + \gamma_P) + \frac{1}{V_{\mathrm{DD}}}\right)\left(\frac{f_0}{f}\right)^2 \tag{4.28}$$

For the differential ring oscillator, the noise is not a function of the K_{VCO}, N and explicitly of Q. While for the single ended ring oscillator, the noise is not a function of the Kvco, explicitly of Q. However, the flicker noise is a function of N; it increases with smaller N (smaller Q). However, these equations are not valid at low offset frequencies as the phase noise will approach infinity, as we mentioned for the LCVCO. Using a Lorentzian phase noise model is more accurate.

4.3.5 Comparison Of Sensitivity And Phase Noise Of Both Oscillators

In the previous section, we have discussed the differences between the LCVCO and RVCO in terms of sensitivity and phase noise. Fig. 4.8 shows a comparison of both oscillators in terms of sensitivity, As it can be seen in fig. 4.8, the RVCO exhibit a much higher sensitivity than the LCVCO. For the same power, operating frequency and K_{vco}, at the same phase shift, the RVCO has a larger frequency change then the LCVCO. However, there are other components to consider. In general, the RVCO occupies smaller area compared tor the LCVCO, as this latter have an inductor in the resonator tank, and inductors take up a large silicon area. Also, the RVCO is superior to the LCVCO in terms of power consumption. Table 4.3 summarizes these differences.

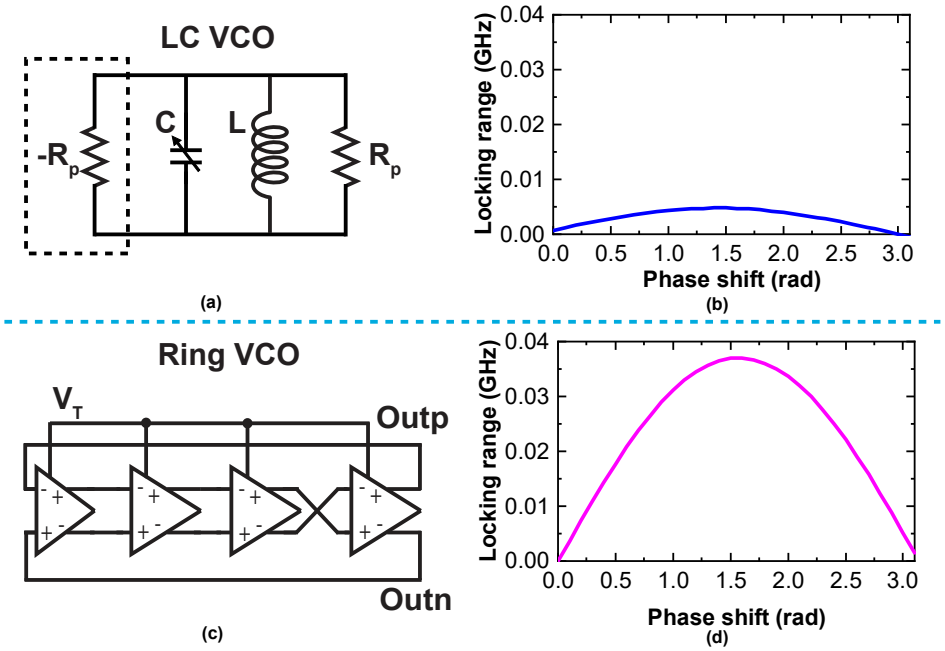

Figure 4.8: (a) LC oscillator tank. (b) The change in the locking range as a function of the change in the phase shift introduce to the LC tank. (C) 3-stage RVCO. (d) The change in the locking range as a function of the change in the phase shift introduce to the Ring.

Table 4.3: Comparison of sensitivity and phase noise of LCVCO ad RVCO

VCO requirements (LCVCO)	VCO requirements (RVCO)
Locking range	Locking range
$\omega_{LR} = \frac{V_i}{V_o}\frac{\omega_o}{Q}$	$\omega_{LR} = 0.6112\frac{V_i\omega_o}{V_o} = \frac{V_i}{V_o}\frac{\omega_o}{Q}$
Better sensitivity: small Q and K_{VCO}	Better sensitivity: small Q and K_{VCO}: Q is already small (1 3)
Small Phase noise: high Q and K_{VCO}	Phase Noise isn't a function of Q but for flicker noise in Diff mode: it decreases with bigger Q
Bigger area	Smaller area than LC even with large N,
Dissipate more power $P_{LC} = 2\frac{QV_{peak}^2}{L\omega_o}$	Dissipate less power $P_{ring} = 2\nu q_{max} V_{DD} f_o$
Less sensitive (narrow tuning range)	More sensitive (Small Q)
Better phase noise	Worst phase noise than LC
Good stability and Low Jitter	Poor stability at high frequency

Chapter 5

Phase-Locked Loop Circuits

5.1 Introduction

A phased-locked loop (PLL) is a negative feedback system where a high frequency oscillator-generated signal is phase and frequency locked to a a low frequency clean reference signal. The phase refers to the relative phase difference between an input signal and the loop's internal oscillator. The term locked means that the oscillator's phase maintains a constant relationship of that of the input signal, or the frequencies of the two signals are the same, otherwise the phase difference would change. Last, the term loop comes from the feedback loop that controls the internal oscillator's frequency to remain in sync with that of the input signal [10]. PLLs are used in many application; they are used as clock generators in microprocessors, as frequency synthesizer, in FM demodulation in FM receivers and many more. The phase frequency detector (PFD) behaves the differencing node of the feedback loop, matching the phase of the divided VCO frequency with that of the reference frequency by controlling the VCO frequency through the tuning voltage. The PLL achieves locking in steady state when both input and output are matched such that,

$$F_{VCO} = N * F_{ref} \tag{5.1}$$

PLL can be a 2nd-order system or higher; a careful study need to be done to insure its stability. Stability study is very important to ensure the functionality of the PLL because it affects the phase error, settling time and the jitters. Also, the PLL components need to be studied and designed carefully to avoid degrading the overall spectral at the output.

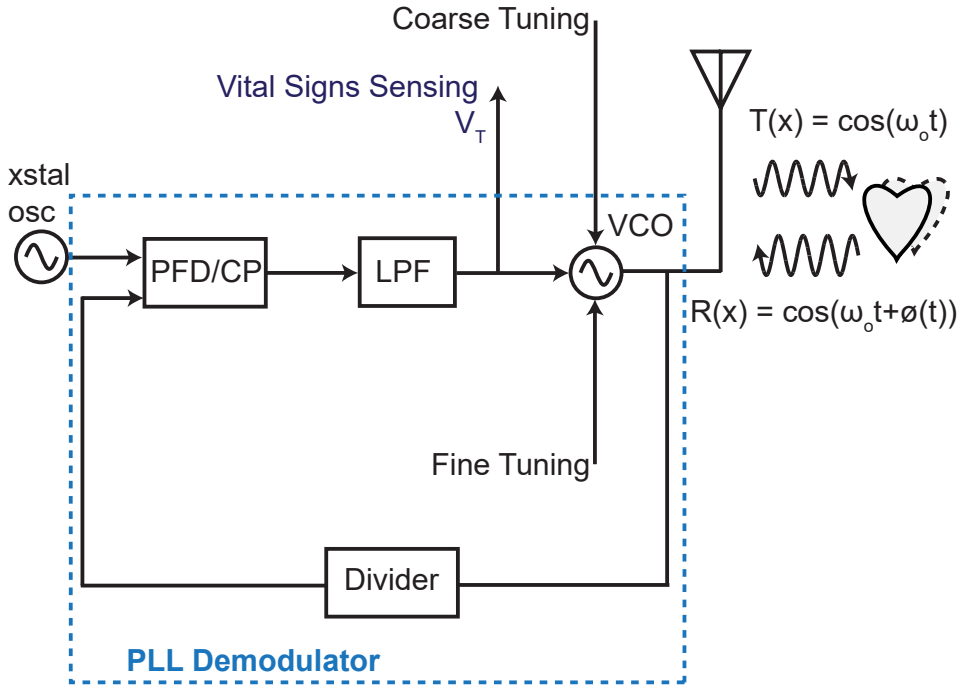

Figure 5.1: Block diagram of a basic PLL.

The PLL acts as a low-pass filter with respect to the reference; low-frequency reference modulation is passed to the VCO output while high-frequency reference jitter is rejected. The PLL also behaves as a high-pass filter with respect to VCO noise.

5.2 Building Blocks

Figure 5.1 shows the main building blocks of a basic PLL. These components are as follow:

- Phase Frequency detector (PFD): outputs digital pulse whose width is proportional to phase error
- Charge Pump (CP): produce current correction from the digital error signal
- Loop Filter (LPF): integrates and filter the error currents to a V_T used to steer the output frequency of VCO
- Voltage controlled oscillator (VCO): changes frequency in response to the control

voltage

- Divider (1/N): divides the output frequency to that of the PFD
- Pre-scaler (1/R) : a divide by R, optional, divided the reference frequency when resolution is needed
- Reference Source (Ref Osc): fix and stable reference frequency.

5.2.1 Voltage Controlled Oscillator

The voltage controlled oscillator produces the high frequency output of the PLL based on the tuning voltage V_T. There are many different architecture used for this block. In fact, at first RC multivibrators were very popular many years, but they are seldom used in integrated circuits (ICs). Ring oscillators are the most popular method used, but it's hard to achieve low jitter and are know for having a poor phase noise. LC tank-based oscillator have gained more popularity with the possibility of having on-chip inductors, they have better phase noise compared to the ring oscillators but take a lot of area in ICs. The VCO contributes the most for high frequency noise the the output of the PLL. But in this application it is not a big concern, as mentioned earlier the PLL will filter the VCO noise in the band of interest. The output of the VCO is tunable through the tuning voltage V_T such that,

$$\omega_o = \omega_n + K_{VCO} * V_T(t) \tag{5.2}$$

where K_{VCO} is the gain or the tuning sensitivity of the VCO, ω_n is the nominal VCO frequency when the tuning voltage is zero and $\omega_o = 2\pi f_{VCO}$ the output frequency of the PLL. Taking Laplace transform of equation 5.2,

$$L[\omega_o] = K_{VCO} * V_T(s) \tag{5.3}$$

where $s = j2\pi f$. It must be noted that the frequency is the derivative of the phase, $\theta_o(t) = \theta(0) + \int_0^t \omega(\tau)d\tau$. If we assume that the initial phase $\theta(0) = 0$, then we can write,

$$\theta_o(t) = \int_0^t \omega(\tau)d\tau = \int_0^t K_{VCO} * V_T(\tau)d\tau \tag{5.4}$$

which can be rearranged in the frequency domain by applying the Laplace transform,

$$\theta_o(s) = \frac{\omega_o}{s} = \frac{K_{VCO} * V_T(s)}{s} \tag{5.5}$$

The transfer function of the VCO block is

$$H_{VCO}(s) = \frac{\theta_o(s)}{V_T(s)} = \frac{K_{VCO}}{s} \tag{5.6}$$

which is the same as an ideal phase integrator in the s-domain.

5.2.2 Divider

A divider is the fastest block in PLL loop, and consumes the most power. It takes the output frequency at the VCO output and divides it by an integer number N usually. Another divider topology used consists of a modulus pre-scaler divider $M/M+1$, it divides the the VCO frequency to a range of frequencies instead of just one. To implement the divider, different circuit topologies can be used such as current-mode logic, CMOS divider, and True Single Phase Clock (TSPC) Logic and more. Current-mode logic are the highest speed can be fully differential but they are power hungry and do not have enough voltage head room for low VDD. TSPC, on the other hand, is a dynamic logic as it has fewer transistors and thus less loading then static ones. Also, it uses a single clock, which reduces clock routing and it is usually used at the front-end of high frequencies. A frequency divider can be seen as a phase divider, for which the phase domain transfer function is given by,

$$\theta_{div}(s) = \frac{\theta_o(s)}{N} \tag{5.7}$$

or,

$$H_{div}(s) = \frac{1}{N} \tag{5.8}$$

5.2.3 Phase and Frequency Detector

The function of a phase detector is to measure the phase difference of two incoming signals, the divider output signal and the reference signal, and produces a signal that is proportional to the difference between the two phases 5.2. The error signal has to remain constant with time for the loop to be locked. The most common circuit used for the

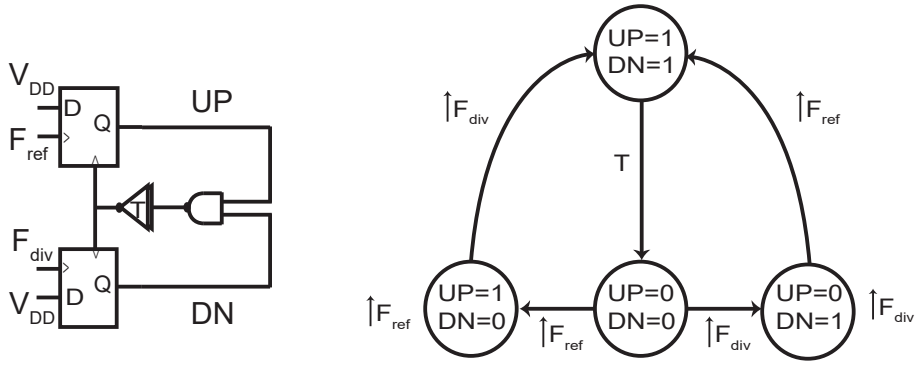

Figure 5.2: (a) Tri-state phase and frequency detector PFD and (b) Transition state diagram

PFD is the tri-state PFD. This configuration outputs two signal, UP and DN, that are pulse-width modulated as a function of the phase and frequency error difference between the two input signals. Fig. 5.2 b represents the transition state diagram of the tri-state PFD circuit. When the reference frequency is high, the UP signal goes high, and when the divider frequency is high, the DN signal goes high. However, when both the reference and divider signal are high, the reset is activated, which resets the UP and DN signal and both go low via the reset AND gate. Fig. 5.3 shows the PFD signal waveforms. In fact, when the reference signal leads the divider signal, the UP is high. When the reference signal lags the divider output signal, the DN signal turns high. The width of the UP and DN pulses depends strongly on the delay in the reset path. The delay in the PFD circuit is very important,as a minimum delay time before resetting the UP and DN pulses to avoid a phenomenon called the dead-zone. Fig. 5.4 shows a simplified time-averaged output of the PFD with respect to phase error. The PFD can lock to any phase error, but there are some performance considerations if the phase error is very small or if the phase error exceeds 2π.

5.2.4 Charge Pump

The charge pump circuit, as shown in Fig. 5.5, converts the digital output pulses, UP and DN signals, of the PFD to a digital current pulses and well-defined charges. These

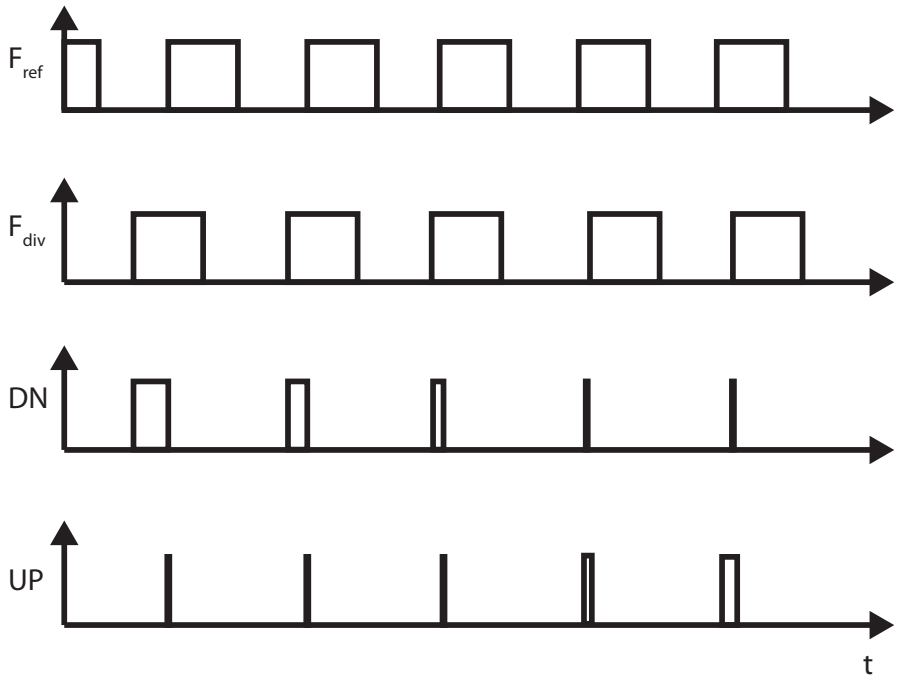

Figure 5.3: Tri-state phase and frequency detector signal waveforms

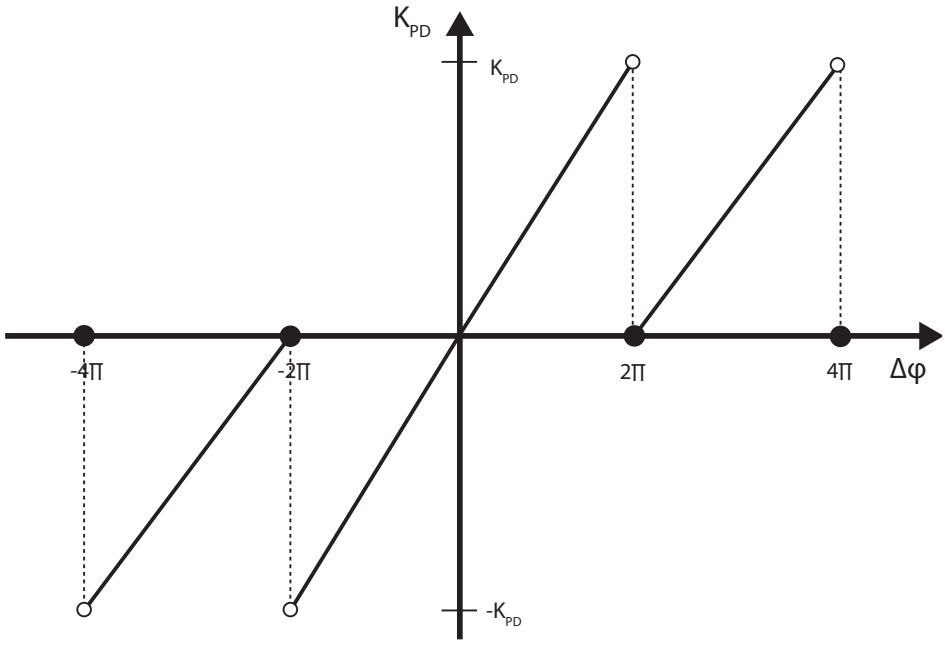

Figure 5.4: PFD Transfer function

current pulses are then passed through a loop filter to generate a tuning voltage to the VCO. When the phase error is very small, such that the UP and DN signals have a very small width, it is possible that the charge pump will not output a current proportional to the phase error. This phenomenon is what was mentioned before as the dead-zone and is unwanted. This phase error is seen as jitter at the output of the PLL. As mentioned earlier, adding a minimum delay in the path of the reset circuit, such that the UP and DN pulse widths is larger then the turn on time of the charge pump. Other ways to avoid dead-zone is to introduce a bleed current that pulls the phase detector away from operating with zero phase error. It can be also avoided by introducing a minimum on time for the phase detector to ensure that it operates away from a phase error that is too small. From Fig. 5.4, the tri-state of the PFD and CP ideally gives a transfer function with a constant slope over the range of -2π to 2π, while outside this range, the PFD and CP behaves as a frequency discriminator pushing the frequency back to the origin [17]. The PLL pull-in range, the range of frequency difference over which the PLL is able to acquire lock, is limited by other components in the loop. Once the PLL has reached lock, the phase error is ideally 0 and the PFD-CP transfer function can be written as follow,

$$H_{PD}(s) = \frac{I_{CP}}{2\pi} \tag{5.9}$$

Some non-ideal effects of the charge pump, is the UP and DN currents mismatches due to phase error and the loop adjustment so that the net charge is zero; phase offset. Also, the skew between UP and DN introduces ripples in the VCO tuning voltage or jitter, which can be suppressed by adding a pass gate at the DN path [10].

5.2.5 Loop Filter

The loop filter filters and conditions signal within loop, it minimizes the noise and spurs. It also manipulates the loop dynamics by making the system more stable and controlling the loop settling time. Many different implementations can be used, either on-chip or off-chip; Passive or active. Some have integration capacitor (type-II PLL) and some don't (type-I PLL), last but not least it can be analog (for I/VCO) or digital (for DCO). There is not a loop filter that is right for every application as it involves performance trade-off [10].

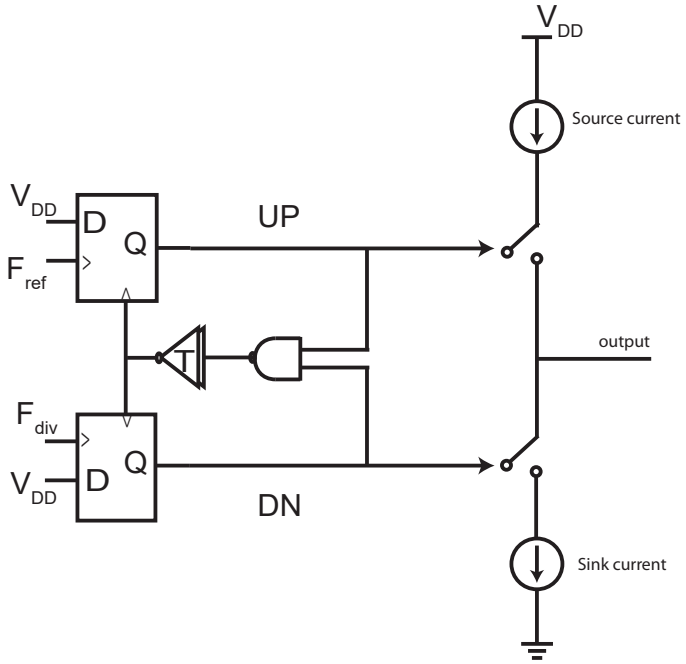

Figure 5.5: Phase and frequency detector PFD with a simple charge pump.

The loop filter used in this project is a 2nd order passive filter. It consists of a combination of a series resistor and a capacitor, in parallel with another capacitor, Fig. 5.6. Capacitor C_1 adds an integrator path and introduces a pole, while the resistor adds a proportional path and introduces a zero. The Capacitor C_2 is used to suppress the tuning voltage ripples while comprising the stability of the PLL. The loop filter functions as a low-pass filter and rejects the input high-frequency noise of the PLL and generates the control voltage to drive the VCO. The transfer function of a generic second-order loop filter is given by,

$$Z(s) = \frac{K_{LPF}}{s} * \frac{1 + s/\omega_z}{1 + s/\omega_p} \tag{5.10}$$

Analyzing the the second order loop filter in 5.6, $K_{LPF} = 1/(C1 + C2)$, the zero at $\omega_z = 1/(R_1C_1)$ and the pole at $\omega_p = R_1C_1C_2/(C_1 + C_2)$. Thus, equation 5.10 becomes,

$$Z(s) = \frac{s + \frac{1}{R_1C_1}}{C_2s^2(s + \frac{C_1+C_2}{R_1C_1C_2})} \tag{5.11}$$

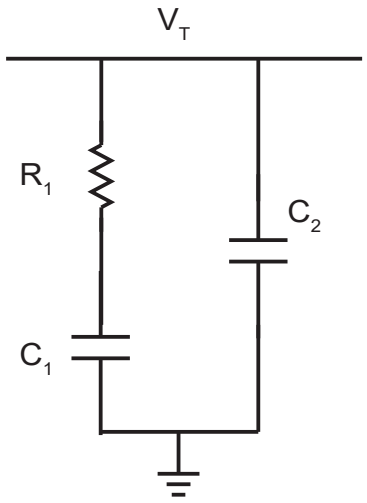

Figure 5.6: A second order passive loop filter.

5.3 PLL Loop Dynamics

In this section, the loop dynamics of the PLL will be analyzed in the locked state PLL is a feedback system, and thus the stability and dynamic response need to be studied. However, since PLLs are highly non-linear systems, it makes this study difficult. When the PLL is in Lock, it can be approximated to a linear model. The PLL has a particular order and type which are determined as follows [17]:

- The type of the PLL is determined by the number of integrators
- The order of the PLL is determined by the number of poles.

PLL controls the VCO frequency but compares phase in the PFD, the loop inherently contains a $1/s$ term already.

5.3.1 PLL Loop Theory

In this section, the discussion of the linearized continuous-time transfer functions valid for a third-order type-II PLL. The open-loop transfer function of the system can be expresses

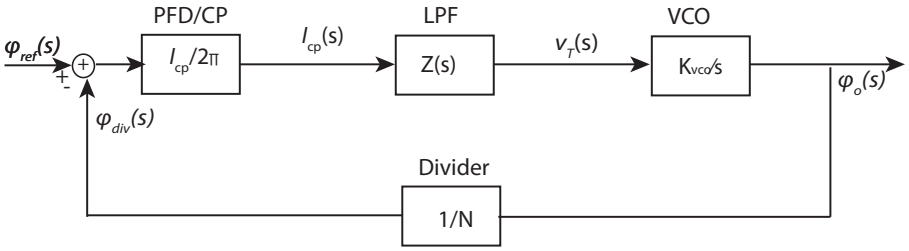

Figure 5.7: A linear model of the PLL system.

as,

$$G(s) = \frac{\theta'_{div}(s)}{\theta_{div}(s)} = \frac{K_{PD}K_{VCO}Z(s)}{s} \tag{5.12}$$

While the closed loop transfer function can be expressed as,

$$CL(s) = \frac{\theta_{ref}(s)}{\theta_{out}(s)} = \frac{G(s)}{1 + G(s) * \frac{1}{N}} \tag{5.13}$$

The loop bandwidth is defined as the frequency that forward loop transfer function to have a gain of one,

$$||G(j\omega_c)|| = 1 \tag{5.14}$$

where ω_c is the loop bandwidth in radians and the phase margin is defines as,

$$PM = \pi - \angle G(j\omega_c) = \tan^{-1}(\frac{\omega_c}{\omega_z}) - \tan^{-1}(\frac{\omega_c}{\omega_p}) \tag{5.15}$$

Choosing ω_c involves trading off lock time for spurious rejection, as it affects affects phase error, settling time and jitter. However, other configuration-dependent variables generally come into play as well. The benefit of the lead-compensation zero ω_z providing a substantial boost to the phase margin. Beyond ω_z, ω_p eventually begins to take effect and restores the response roll off to its original rate of $-40\,dB$ per decade. In fact, choosing the right phase margin is crucial to the stability of the PLL. If the phase margin is low, there tends to be peaking in the closed loop transfer function (CLTF) and ringing in the PLL transient response. But is the phase margin is higher, it gives a flatter CLTF, but excessively high PM will degrade the switching speed of the PLL. Practically,

the phase margin is usually set to 45-60 degrees [10]. From equation 5.15, the phase margin depends on the ratio of ω_c and pole and zero of the filter. As for choosing other parameters, $I_{cp}, K_{VCO}, K_{LPF}, N$, other constraints like noise and area need to be taken in consideration.

The Stability of a PLL is a closed loop analysis of the PLL; where large changes in the loop gains or unaccounting for VCO input capacitance can affect the performance of the loop. It requires that the poles of the closed loop transfer function, equation 5.15, are in the right hand plane. For this kind of stability, Routh's Stability Criteria, is the most complete test for this, but there also exist the criteria of phase margin and gain margin that can be used as indicators as well [10]. For the Routh's Stability Criteria, the poles should have a negative real part without explicitly calculating them. The phase margin study gives insight of the the transient behavior, the peaking in the loop filter response, and stability. Nevertheless, it is not perfect metric for stability because there is the possibility of having a low PM, and the loop is stable. The stability study requires a discrete sampling stability. The PLL's charge pump is often modeled as having a continuous analog current, but as mentioned before, the charge pump's output is pulse width modulated signal with an average current proportional to the error at the phase detector. To use the analog model for stability study, the bandwidth, ω_c should be less then a tenth of the PFD frequency. If $1/10 < \omega_c < 1/5$ of the PFD, The PLL will lock but with distortion. However, if $\omega_c = 28\%$ of the PFD frequency, he loop filter will be unstable due to the discrete sampling action of PFD. From stability stand point, the 2nd order filter is the most stable; there is no constraints for the gain and phase margin and the poles constraint always met [10].

5.3.2 PLL Transient Response

In this section, we assume that the phase detector is modeled as having a continuous analog output and the PLL system is ideal. Fig. 5.8 shows the typical transient response of a system. In case of the PLL, if the PLL is locked at frequency f_1, and the VCO output changed causing the PLL to switch and lock at a frequency f_2. The rise time is the time it takes to first reach the frequency f_2, while the time it takes to reach the maximum

frequency, the peak frequency, value is the peak time. The overshoot is the difference between the peak frequency and f_2. From the previous section, the loop filter equation 5.11 can be rewritten as,

$$Z(s) = \frac{T_2 s + 1}{s(A_1 s + A_o)} \tag{5.16}$$

where $A_1 = R_1 C_1 C_2$, $A_o =$ and $T_2 = R_1 C_1$ and the pole is at $T_1 = \frac{R_1 C_1 C_2}{R_1 C_1}$. The close loop transfer function can be expressed as,

$$CL(s) = \frac{KN(T_2 s + 1)}{A_1 s^3 + A_o s^2 + K s T_2 + K)} \tag{5.17}$$

where $\frac{K_{PD} * K_{VCO}}{N}$. The close loop transfer function in equation 5.17 can be approximated for a 2nd roder system,

$$CL(s) \approx \frac{N\omega_n^2}{s^2 + 2\zeta\omega_n s + \omega_n^2} \tag{5.18}$$

where $\omega_n = \sqrt{\frac{K_{PD} * K_{VCO}}{N A_o}}$ and $\zeta = \frac{T_2}{2}\omega_n$.The poles are located at $p_{1,2} = \zeta\omega_n \pm j\omega_n\sqrt{\zeta^2 - 1}$. The system is critically damped when $\zeta = 1$, and the poles are $p_{1,2} = \omega_n$. For under-damped response, $0 < \zeta < 1$, and the poles are repeated at $p_{1,2} = \omega_n \pm j\omega_n\sqrt{1 - \zeta^2}$. When $\zeta > 1$ and $\zeta = 0$, it is an over-damped response and undamped response respectively. The event of locking can be thought of as changing the reference frequency from f_1/N to f_2/N, which is equivalent to multiplying equation 5.18 by $\frac{(f_2 - f_1}{Ns}$,

$$CL(s) \approx \frac{N\omega_n^2}{s^2 + 2\zeta\omega_n s + \omega_n^2} \frac{(f_2 - f_1}{Ns} \tag{5.19}$$

Taking Laplace transform of this latter,

$$f(t) = CL(t) \approx f_2 + (f_2 - f_1)e^{-\zeta\omega_n t}\left[cos\left(\omega_n\sqrt{1-\zeta^2}t\right) + \frac{\zeta}{\sqrt{1-\zeta^2}} sin\left(\omega_n\sqrt{1-\zeta^2}t\right)\right] \tag{5.20}$$

Equation 5.20 will be used to derive the transient components of the PLL such as the peak time, percent overshoot etc. The rise time as mentioned before is the time it takes to first reach the steady state value, by setting $f(t) = f_2$. The rise time can be expressed as,

$$t_r = \frac{tan^-1\left(\frac{\sqrt{1-\zeta^2}}{\zeta}\right)}{\omega_n\sqrt{1-\zeta^2}} \tag{5.21}$$

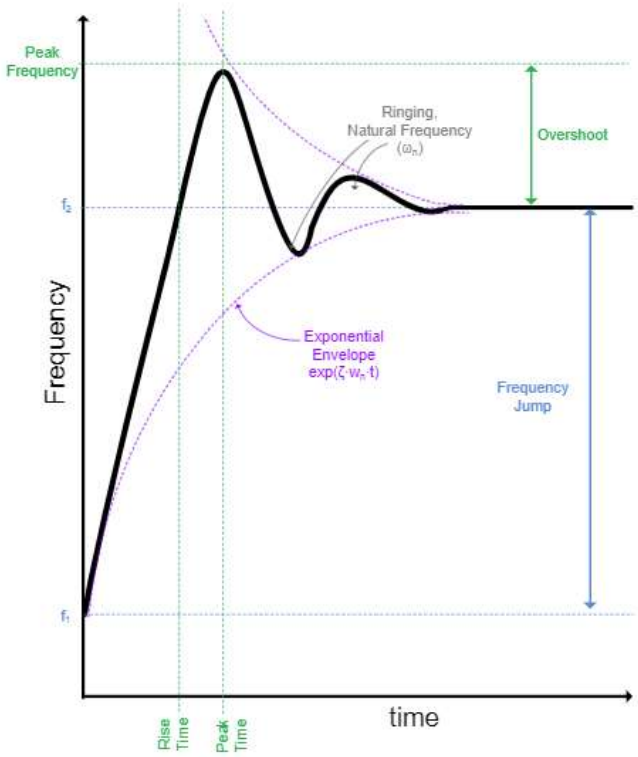

Figure 5.8: Classical model for the transient response of a PLL [10]

.

The peak time is the time to reach the peak frequency, to solve for that, we take the derivative of equation 5.20 and set it equal to zero,

$$t_{peak} = \frac{\pi}{\omega_n \sqrt{1-\zeta^2}} \tag{5.22}$$

The next step is to find the percent overshoot, which is the absolute difference of the peak frequency and the final frequency.

$$\%OS = f(t_{peak}) - f_2 = \frac{f_2 - f_1}{\sqrt{1-\zeta^2}} exp\left(\frac{-\pi\zeta}{\sqrt{1-\zeta^2}}\right) \tag{5.23}$$

The lock time (LT) is derived in [10] by setting the derivative of equation 5.20 to zero, finding the maximum value then substitute the result back in the same equation and

solving for time,

$$LT = \frac{-\ln\left(\frac{tolerance\sqrt{1-\zeta^2}}{|f_2-f_1|}\right)}{\zeta\omega_n} \tag{5.24}$$

These derivations are all based on the 2nd order approximation. There is dependence between the loop bandwidth, the natural frequency, the damping factor and phase margin, $\omega_c, \omega_n, \zeta, PM$, and the rule of thumb is that,

$$\begin{aligned} \omega_c &= 2\zeta\omega_n \\ \omega_n &= \frac{\omega_c}{2\zeta} \\ \zeta &= \frac{1}{2\sqrt{sec(PM) - tan(PM)}} \end{aligned} \tag{5.25}$$

The damping factor is a measure of stability, the natural frequency is a measure of the bandwidth. Also, the damping factor and natural frequency can be set independently by LPF resistor.

The linearized small-signal analysis predicts behavior when the PLL is locked well, however, attaining lock is highly nonlinear and not well understood. The capture range of a PLL is the maximum difference between VCO output frequency and the reference frequency which can be locked to. On the other hand, the lock range refers to the maximum difference between VCO output frequency and the reference frequency which will stay locked after already been locked. The lock range is wider then the capture range. Despite that, the PFD is what limits the PLL performance, because once PLL locked, it maintains it as input varies until either the PFD or VCO reach maximum value and cannot increase any further.The PFD limits first.

5.3.3 PLL Phase Noise

To study the phase noise of the PLL, the linear continuous time model derived in the previous section should be used. Although this model assumes steady-state, when the PLL is locked, behavior only, it is sufficient as the noise performance when the PLL is not locked is not pertinent. Fig. 5.9 shows all the noise contributors in the PLL loop, from the charge pump, the filter, the VCO and the divider. In practice, to make the phase noise analysis easier, the noises can be input or output referred. The input referred noises

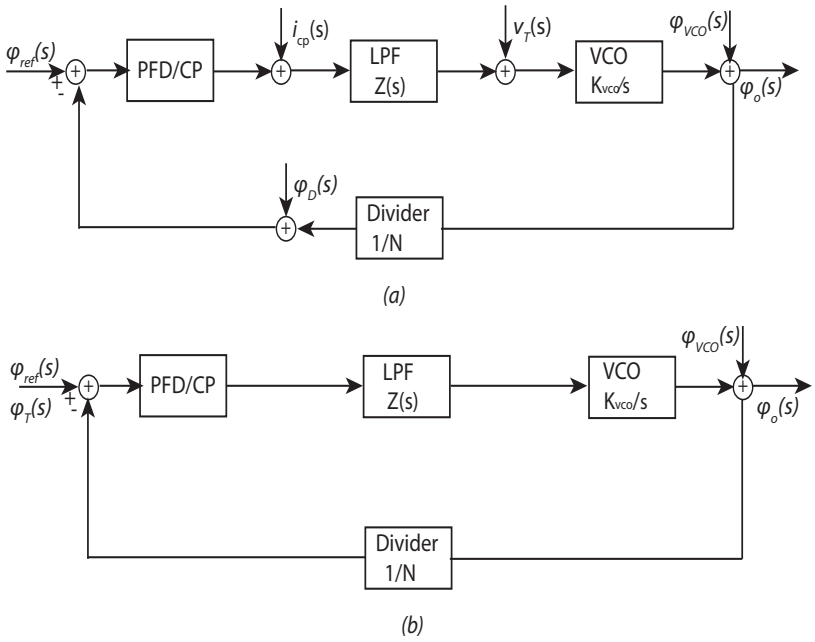

Figure 5.9: (a) PLL phase noise linear model when locked, (b) The same model with input and output referred noise.

.

in the forward path have a low pass behavior. For the reference input noise, the phase noise is expressed as,

$$S_{\phi,ref} = \Phi_{ref}^2 N^2 |CL(s)|^2 \tag{5.26}$$

The input referred noise from the PFD and the charge pump is written as,

$$S_{\phi,pfd} = \Phi_{pfd}^2 N^2 |CL(s)|^2 = i_{cp}^2 \left(\frac{N}{I_{cp}^2}\right)^2 |CL(s)|^2 \tag{5.27}$$

and for the divider,

$$S_{\phi,div} = \Phi_{div}^2 N^2 |CL(s)|^2 \tag{5.28}$$

As for The input referred noise from the loop filter is expressed as a bandpass characteristics,

$$S_{\phi,lpf} = \Phi_{lpf}^2 N^2 |CL(s)|^2 = v_T^2 \left(\frac{N}{I_{cp}^2}\right)^2 |\frac{CL(s)}{Z(s)}|^2 \tag{5.29}$$

The VCO's output referred noise have a high pass behavior and is expressed as,

$$S_{\phi,VCO} = \Phi_{VCO}^2 |\frac{1}{1+G(s)}|^2 \tag{5.30}$$

where $G(s) = K_{cp}K_{VCO}Z/sN$. The noise transfer functions can be derived to give overall noise of the PLL. The total output phase noise power spectral density is then calculated as,

$$\begin{aligned} S_\Phi(f) &= \sum_{n=j}^{\infty} |H_j^2(f)| \\ &= S_{\phi,ref} + S_{\phi,pfd} + S_{\phi,div} + S_{\phi,lpf} + S_{\phi,VCO} \\ &= \left[\Phi_{ref}^2 + \Phi_{div}^2 + i_{cp}^2 \frac{1}{I_{cp}^2} + v_T^2 (\frac{1}{I_{cp}^2} \frac{1}{|Z(f)|^2} \right] N^2 |CL(s)|^2 \end{aligned} \tag{5.31}$$

The single-side band (SSB) phase noise is defined as the ratio in dB of the noise power in a $1\,Hz$ bandwidth at an offset frequency from f of Δf is given by, (dBc/Hz):

$$\begin{aligned} L(\Delta f) &= 10 \log_{10} \left[\frac{noisepowerin1Hz + \Delta f}{carrierpower} \right] \\ &= 10 \log_{10} \left[\frac{S_\Phi(\Delta f)}{2} \right] \end{aligned} \tag{5.32}$$

it is worth mentioning that looking into the phase noise from each components, that all components except, for the VCO, are proportional to N^2. As a result, one thing to consider when designing a PLL is to reduce the N value. Moreover, the phase noise equations validates that the high frequency, out-of-band noise, Fig. 5.10 is dominated by the VCO, while the low frequency noise, in-band noise, is dominated by others, but mainly the reference. Also, increasing the charge pump current will also help reduce the in-band phase noise, because both the PFD/CP and LPF phase noise is a function of I_{cp}.

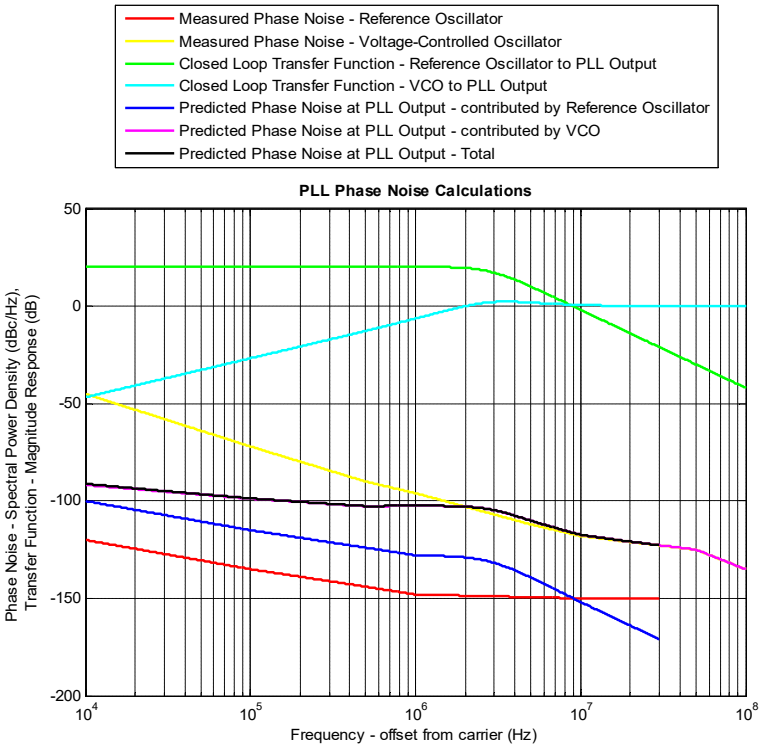

Figure 5.10: Simulated example of the the phase noise contribution of each block and the total phase noise of the PLL using MATLAB.

.

Chapter 6

Proposed SIL PLL-based Radar Systems

6.1 Introduction

A study of the preference of using the LCVCO and Ring VCO (RVCO) was made. Although the LCVCO has many advantages over the RVCO, this later is shown to have a better sensitivity for motion detection. In the previous chapter, I investigated and compared the LC tank based VCO and the ring VCO in terms of mainly sensitivity for motion detection and phase noise. A study of injection-locking of both LCVCO and RVCO was also established. The study has proven that the RVCO is superior to the LCVCO in terms of sensitivity while the phase noise won't be much different as the frequency of interest is very small, in fact heart rate and respiration frequency is very small up to few Hertz. The PLL demodulates the signal, matching the VCO frequency to the reference frequency through the tuning voltage. This latter is filtered, digitized and processed for vital signs measurements. One of the advantages of the PLL is that it acts like a high pass filter to the VCO noise, so all phase noise at low frequency,bellow the loop corner frequency, the frequency of interest, will be filtered. The PLL is also a low pass filter to the reference oscillator. As a result, in this design only the phase noise of the reference oscillator matters, and it can be improved by choosing a very good crystal oscillator to use as a reference. To verify the proposed idea, a design of both systems, LCVCO based PLL and RVCO based PLL was done in 65 nm CMOS process at 1.5 GHz frequency.

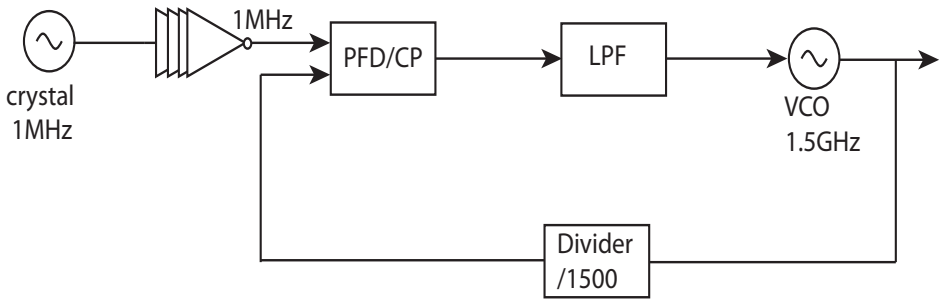

Figure 6.1: SIL effect on a free-running oscillator and its link to motion detection.

The simulation results confirm the idea proposed.

6.2 Phase-Locked Loop Circuits

6.2.1 Phase-Locked Loop Circuits And Simulation Results

6.2.1.1 Phase And Frequency Detector (PFD)

The PFD detects the phase and frequency difference between reference and divider clock, produce a signal proportional to the difference. The implementation of the PFD circuit is shown in 5.5 along with the charge pump.In the figure, f_N and f_R represents the divider signal and the reference signal respectively. Each D-flip-flop (DFF) is based on a NOR circuit. The PFD has three states, UP state where the source current is enabled, a DN state where the sink current is enabled and a RST state where both currents are enabled. The circuit was carefully designed to eliminate the dead zone problem discussed in the previous chapter, by adding the reset delay needed after the NAND gate at the reset input of the DFF. The two D-flip-flops used in the PFD are falling edge-triggered, where the D input is connected to Vdd, while The clocks of the upper DFF and the lower DFF are connected to the reference frequency and the divider's output respectively. When the falling edge of the reference signal leads that of the divider's output, then the UP signal is set to increase its output frequency. However,When the falling edge of the reference signal lags that of the divider's output, then the DN signal is set to decrease its output

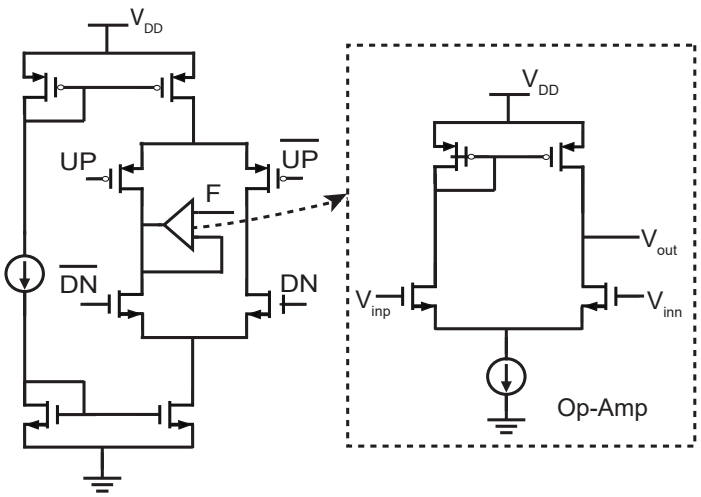

Figure 6.2: Phase and frequency detector PFD with a simple charge pump.

frequency. In the third state, the AND gate and inverters reset both the UP and DN signals and the next cycle starts. Fig. 6.2 shows the circuit used for the NOR-based DFFs with the AND and inverters in the reset path.

6.2.1.2 Charge Pump Design

The charge pump converts the digital pulses from UP and DN signals of thr PFD to current pulses to be fed to the filter to generate the tuning voltage to the VCO. The implementation of the charge pump circuit can be done in many different ways. One of the main hurdles to overcome while designing the charge pump is to reduce current mismatch. Current mismatch will lead to static phase offset and will cause ripples in the tuning voltage, which will introduce jitters in he output. In this project, bootstrapped architecture is used as in Fig. 6.2. In fact, using the bootstrapped architecture will insure the reduction of the up and down current mismatch, as it allows a differential current steering and can operate with low swing UP/DN signals. It employs a unity gain amplifier to ensures that the same voltage is maintained at the input and the output of the amplifier which allows the up current to equal the down current.

Fig. 6.3 shows the schematics of the PFD and charge pump circuit. Fig. 6.4 shows the simulation results of both PFD and charge pump with a 2nd order low-pass filter at the

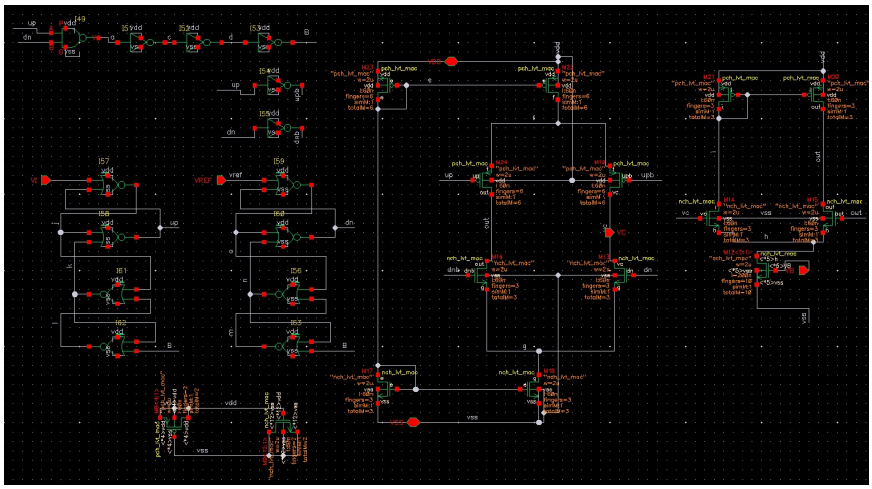

Figure 6.3: Schematics of the PFD and charge pump.

output. The PFD waveforms shows the PFD circuit is functioning correctly. When the $clk2$ signal is leading the clk signal, UP goes high, while in the case When clk goes high, $clk2$ goes low, DN signal is high. However, when both clocks are high and the reset path is activated which pulls UP and DN to 0. The 4th wavform in the graph shows the digital output voltage at the charge pump. Finally, the last waveform is the tuning voltage to the VCO after the output voltage of the charge pump get filtered and transformed to an analog signal. It shows that the tuning voltage increases as the UP voltage is high, and UP current is on, and it decreases as the DN voltage is high, and DN current is on.

6.2.1.3 Divider

The divider is the feedback linking the VCO to the PFD and charge pump. In this design, both the RVCO and LCVCO operates at a frequency of 1.5 GHz and the reference frequency is at 1 MHz.Thus, ad divider of 1500 is needed. This division was implemented with a series of three divide by-5-circuit and a divide-by-3 circuit and two divide-by-2 circuit. All divider circuits are implemented using a combination of DFFs and logic gates except for the first divide-by-2 circuit. Since the VCO frequency in in the gigahertz's range, the initial divide-by-2 DFF needs to be fast with low delay and clock-skew. In fact, a true-single phase clock (TSPC) architecture is used. Fig. 6.5 and 6.6 represents the schematics and simulation of the divider circuit respectively. The simulation shows

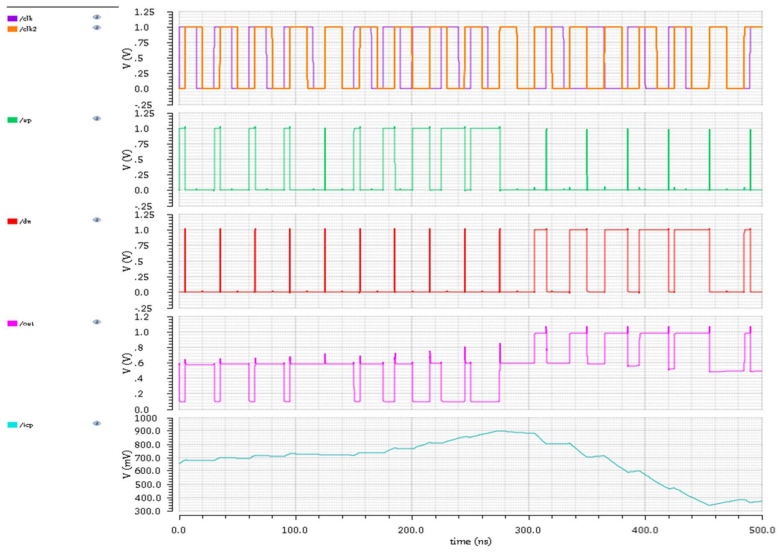

Figure 6.4: Figure 2 Phase and frequency detector PFD with a bootstrapped based charge pump

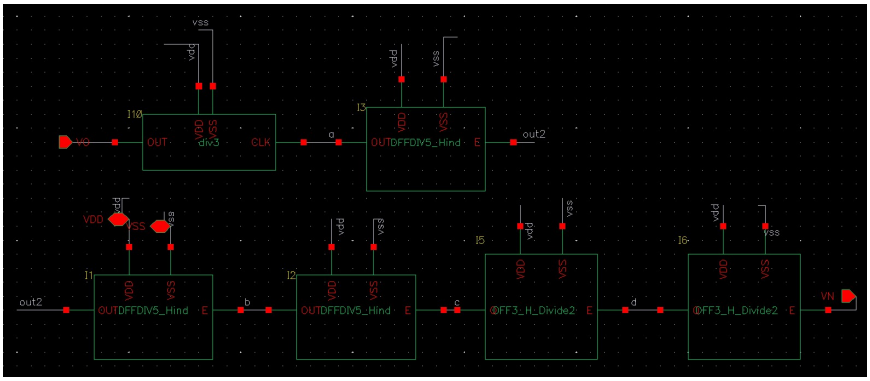

Figure 6.5: Schematics of the divider circuit.

the high-frequency of the VCO clock and the low-frequency divided clock. In figure 6.6, it can be shown that the frequency of VCO clock is 1.5 GHz while that of the divided clock is 1.0 MHz. As a matter of fact, the frequency of divided clock is a 1500th of the frequency of the VCO clock hence verifying the functionality of the divider circuit.

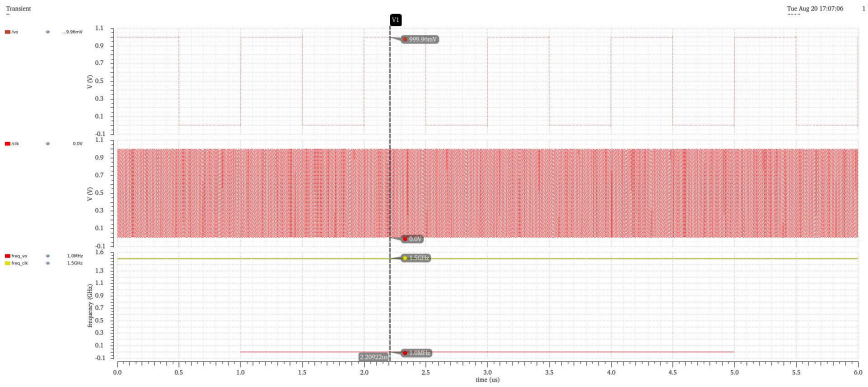

Figure 6.6: Simulation of the divider circuit.

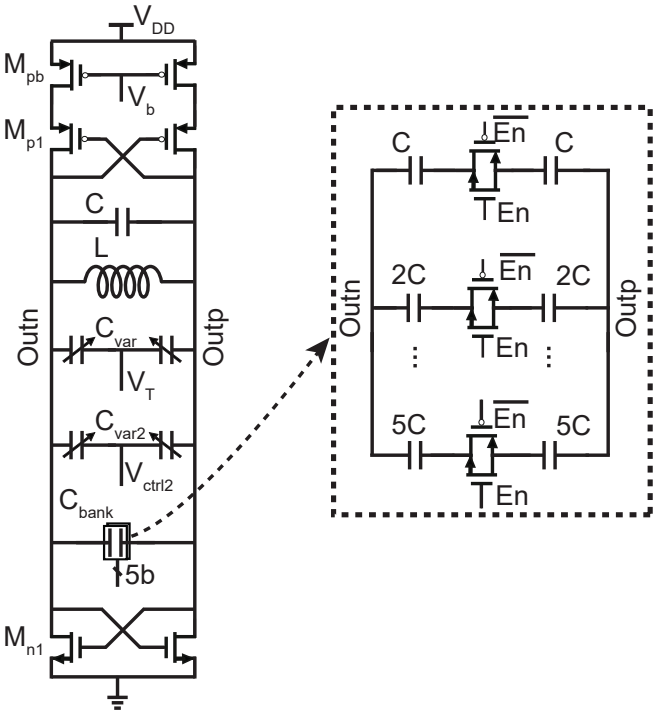

Figure 6.7: Proposed LC voltage controlled oscillator circuit.

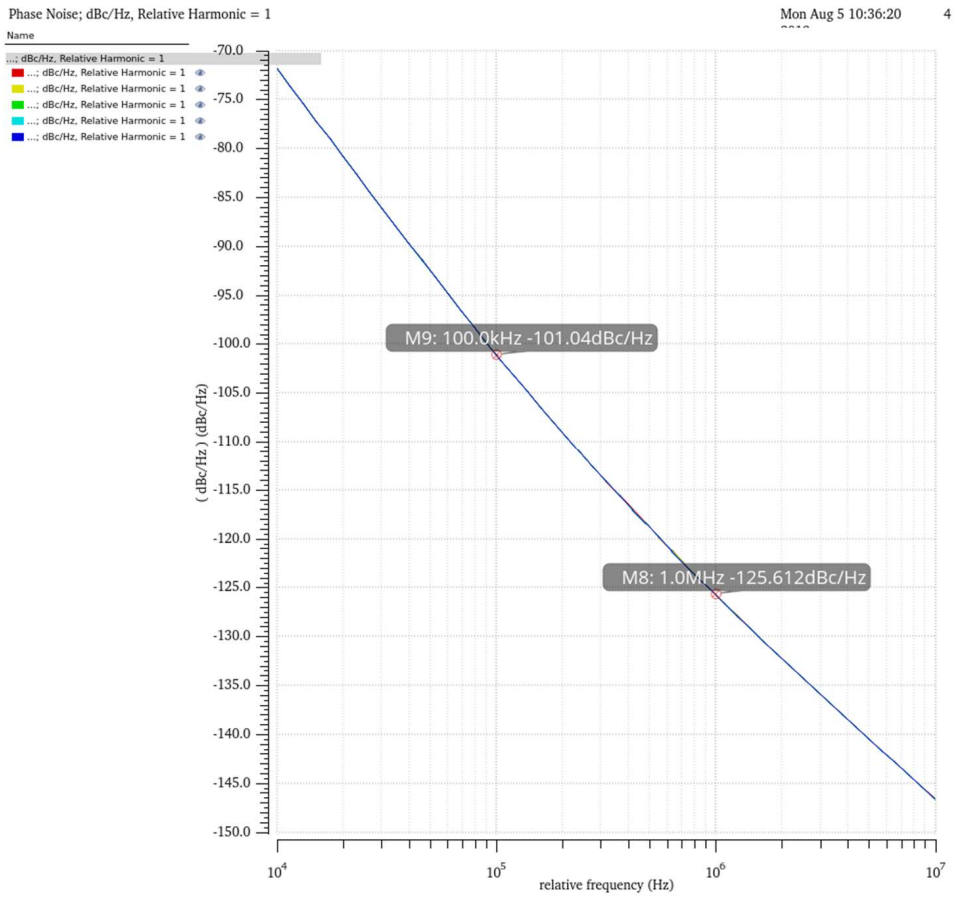

Figure 6.8: The transient simulation for the phase noise of the LCVCO circuit.

6.3 Voltage-Controlled Oscillators

6.3.1 LC VCO

The LC tank based VCO is implemented with an NMOS-PMOS cross coupled topology.The LCVCO oscillates at a frequency of 1.5 GHz and has a triple tuning mechanism. The fine tuning, tuning feeding from the PLL has a K_{VCO} of 6 MHz/V; a small K_{VCO} to encompass the small change in the frequency caused by the heart motion. This fine tuning is implemented through a couple of varactors, which are nothing more than NMOS or PMOS transistors with their source and drain terminals shorted together. The LCVCO has also a 5-bit digital tuning, a coarse tuning, to increase the range of the oscillation to 570 MHz/V. In addition, the VCO has also another analog tuning realized through a

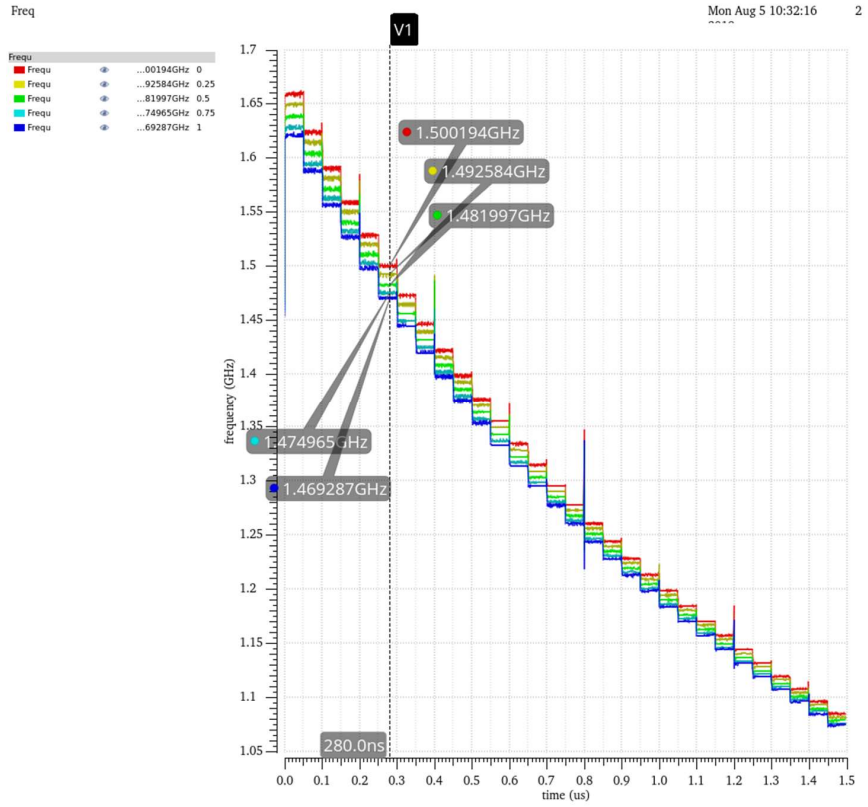

Figure 6.9: The transient simulation for the triple tuning LCVCO covering the full range of frequencies.

couple of MOS varactors with a 40 MHz/V K_{VCO} to cover the steps between the each digital frequency level. The LC-tank oscillator consists of a parallel combination of an inductor and a capacitor driven by a pair of complementary cross-coupled NMOS and PMOS transistors, which can be thought of as a cascade of two CMOS logic inverters, whose capacitance are set by the tuning voltage applied to their common node. This latter provides a positive feedback loop with a gain greater than unity that ensures oscillation and the LC-tank forces the frequency of oscillation ω_o to be

$$\omega_o(t) = \frac{1}{\sqrt{LC}}, \tag{6.1}$$

To achieve an oscillation at f_o =1.5 GHz, the tank capacitance was chosen to be $C = 3.75\,pF$ and $L = 3\,nH$. The Q of the inductor was designed to be 8, the Q is very small, because as discussed before, the smaller the Q the better is the sensitivity. The

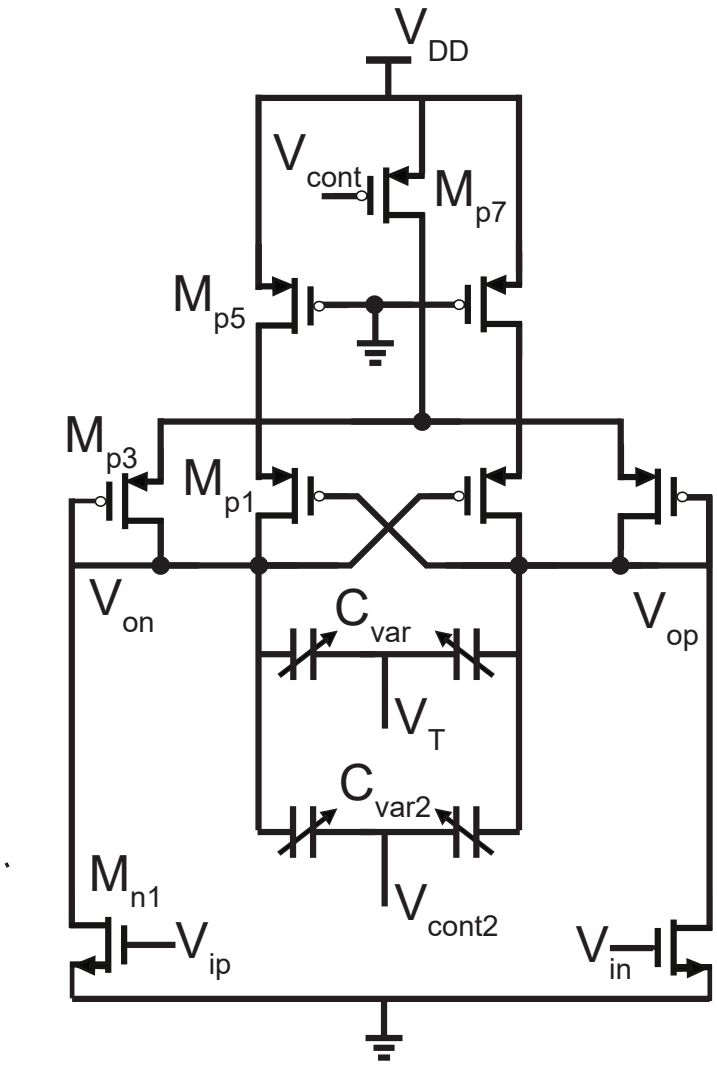

Figure 6.10: Proposed delay element with controllable current source.

LCVCO has a peak voltage ranging between $1000 - 880mVpeak$, the K_{VCO} is designed to be 6 MHz/V and the phase noise is -101 dBc/Hz at 100 KHz, Fig. 6.8. The other tuning consists of digital 5-bit tuning giving the oscillator a range of 570 MHz, while the third tuning voltage is analog tuning varactors with a range of 40 MHz/V to cover the digital steps; Fig. 6.9.

6.3.2 Ring VCO

The ring VCO is implemented using a 4-stage differential delay elements. Each delay elements is realized using the circuit shown in fig 6.10. The ring VCO has an oscillation frequency of 1.5 GHz and has a triple tuning mechanism. The fine tuning feeding from the PLL has a K_{VCO} of $6\,MHz/V$; similar to that of LCVCO. The other tuning, coarse tuning, to the RVCO is done through the gate of PMOS to change the current in the delay element. The third one is through a MOS varactor bring the tuning rage to 800 MHz.

The RVCO is implemented with a 4-stage differential topology 6.10. The differential topology is favoured because it has a better common mode rejection ratio (CMRR) performance and better noise performance. Also, the differential implementation can utilize an even number of stages by simply configuring one stage such that it does not invert [75]. The period of oscillation of a ring oscillator is defined by the time it takes for a transition to propagate twice around the ring. Each delay element in RVCO has a delay of τ, if the delay is repeated N time, odd of single ended delay element and even for differential, then the oscillation frequency of the oscillator is found as,

$$f_o = \frac{1}{2N\tau} \tag{6.2}$$

so, for an oscillation frequency of $1.5\,GHz$, a delay of $\tau = 83.3\,ps$ is needed for a four stage ting oscillator.

Each stage of the RVCO is implemented using the delay element circuit shown in Fig. 6.10. The delay element is based on a modified current starved architecture, and consisted of two NMOS input pair cross connected to a two PMOS transistor for negative conductance for oscillation. It also has a diode-connected PMOS pair and a PMOS tail transistor wit a tuning gate voltage to tune the frequency [75]. The tuning is established by changing the transconductance gm of the diode connected PMOS by changing the current going through the transistors.However,in this architecture,the V_T and ω_o relationship is nonlinear, because the relationship between the gm and the drain current is also non linear. As a result, this non-linear relationship will affect the loop dynamic of the PLL. To overcome this issue, two couple of varactors are added at the output node, each couple is tuned through a control voltage. One is used for coarse tuning and the other for fine

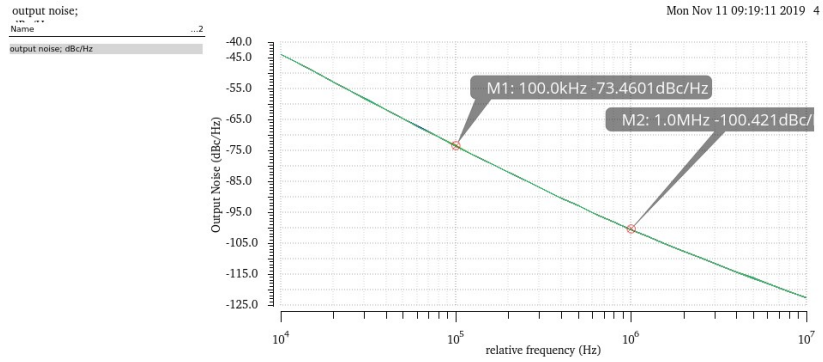

Figure 6.11: Phase noise of the 4-stage RVCO

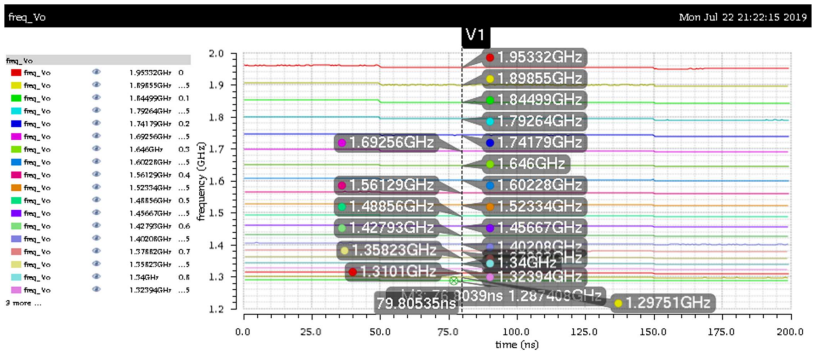

Figure 6.12: The transient simulation for the triple tuning LCVCO covering the full range of frequencies.

tuning, which is connected to the PLL. The circuit has also two PMOS transistors whose gates are grounded; they act as a current source for a pull-up for the cross-coupled PMOS transistors.

To achieve an oscillation at $f_o = 1.5\,GHz$, the delay of each of the 4 stages of the ring oscillator was set to $83.3\,ps$. The RVCO has a peak voltage ranging between 100 to $800mVpeak$, the K_{VCO} is designed to be $6\,MHz/V$ and the phase noise is $-100\,dBc/Hz$ at $1\,MHz$; 6.11. The other tuning consists of a second varactor giving the oscillator a range of 750 MHz through V_{cont2}, while the third tuning voltage is analog tuning the current of the PMOS transistor M_{P7}, through V_{cont}; Fig 6.10.

6.4 PLL Simulation Results

6.4.1 PLL calculation

The charge pump circuit designed has an UP/DN current equals to $610 micro - amps.$ to increase the sensitivity of the system, the control tuning the the VCO through the PLL should be as small as possible. With both VCO designs, the K_{VCO} of both oscillators is designed to be $6MHz/V$. For the initial design, MATLAB was used to calculate the loop filter components. First, the PLL's bandwidth and phase margin were set, and other components were calculated based on the circuit components designed. Let's define the optimization factor γ [10] as,

$$\gamma = \frac{T_2}{\omega_c^2 A_o} \tag{6.3}$$

This factor give a relationship between the loop bandwidth and the phase margin; in fact, if γ is unity, the phase margin is maximum at the loop bandwidth. When $\gamma > 1$, the maximum point is lower than the BW, while when $\gamma < 1$, it is higher than the loop bandwidth frequency. In this design, the optimization factor is set to be $\gamma = 0.7$. The VCOs oscillates at a frequency of $1.5\,GHz$.The bandwidth was set to $1\,KHz$, while keeping the charge pump operating as having a continuous analog current (as discussed in the previous chapter). Also, the phase margin was set to be equal to 60. Then,

$$\begin{aligned} K_{PD} &= \frac{I_{pump}}{2\pi} \\ K_v &= 2\pi K_{VCO} \\ \omega_c &= 2\pi f_{BW} \end{aligned} \tag{6.4}$$

Then, the T_1, T_2 and A_o, from the previous chapter, can be calculated as,

$$\begin{aligned} T_1 &= \left(\sqrt{(1+\gamma)^2 * \tan(pm^2) + 4\gamma} - (1+\gamma)\tan(pm)\right)\frac{1}{2\omega_c} \\ T_2 &= \frac{\gamma}{\omega_c^2 T_1} \\ \omega_c &= 2\pi f_{BW} \end{aligned} \tag{6.5}$$

Once T_1 and T_2 are calculated, A_o can be evaluated as,

$$A_o = K_{PD} K_v \frac{f_{ref}}{\omega_c^2 f_o}\sqrt{\frac{(1+\omega_c^2 T_2^2)}{(1+\omega_c^2 T_1^2)}} \tag{6.6}$$

Form here, the second order filter components can be calculated as,

$$\begin{aligned} C_1 &= A_o \frac{T_1}{T_2} \\ C_2 &= A_o - C_1 \\ R_1 &= \frac{T_2}{C_2} \end{aligned} \tag{6.7}$$

Using MATLAB, the PLL designed will be stable when the filter components are:

$$\begin{aligned} C_1 &= 228\,nF \\ C_2 &= 17.6\,nF \\ R_1 &= 2.60\ K\Omega \end{aligned} \tag{6.8}$$

6.4.2 PLL Simulation

In the real system, the PLL will be directly connected to the antenna to received the modulated signal from the heart. To perform the simulation in virtuoso, the heart modulated signal was simulated using a variable capacitor, as the heart signal is not quantified of how much modulation will cause. The PLL was simulated by adding a $50\,\Omega$ resistance and the capacitor, whose values are changed. As the theory suggested, changing the loading in the VCO, will change its frequency. Then, the tuning voltage will try to bring the frequency of the VCO back to its initial resonant frequency of $1.5\,GHz$. Figures 6.13 and 6.14 represents the simulation for the LCVCO based PLL and RVCO based PLL respectively. The top red curve represents the modulation of the tuning voltage, while the bottom curve shows the PLL locking.

6.5 PLL's Layout

The PLL was layed out and sent to be manufactured in the TSMC 65 nm process. Fig. 6.15 shows the layout for the LCVCO based PLL, while Fig. 6.15 is the layout for the RVCO based PLL. The LCVCO-based PLL die has an area of $0.4\,mm^2$, while the RVCO-based PLL die has an area of $0.28\,mm^2$.

6.5.1 Other Loop Components Consideration

The reference frequency was chosen to be small 1 MHz, the PFD frequency, to sense the heart and respiratory rate while having a low phase noise at these offset frequencies. The

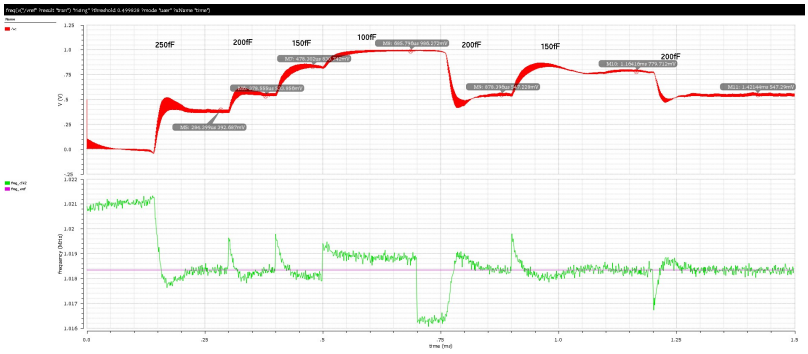

Figure 6.13: Full LCVCO PLL transient simulation.

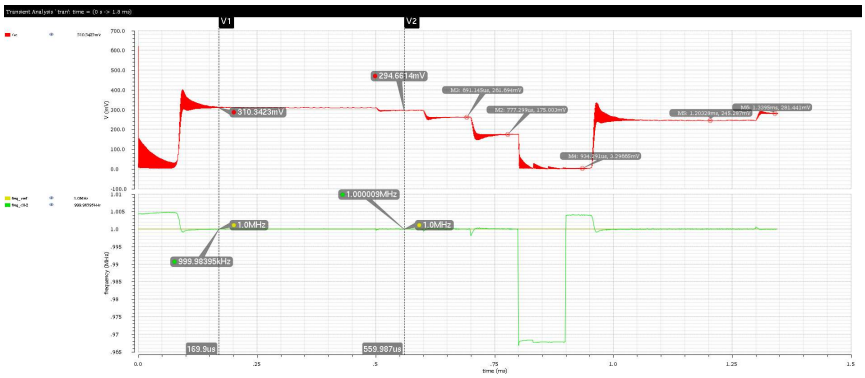

Figure 6.14: Full RVCO PLL transient simulation.

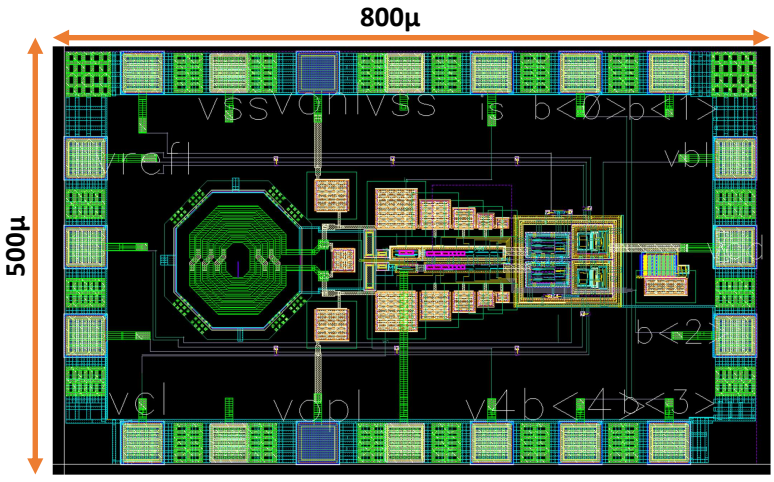

Figure 6.15: Layout of the LCVCO-based PLL.

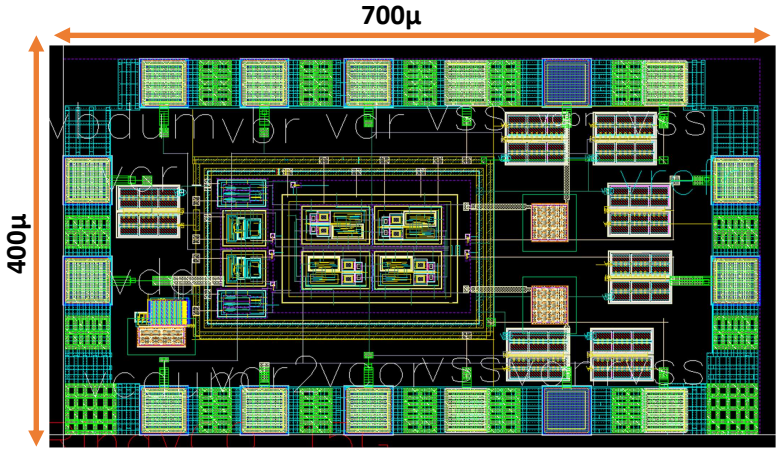

Figure 6.16: Layout of the RVCO-based PLL.

loop filter was designed off chip. The bandwidth of the loop was chosen to be small, few hundredths hertz, because the signal of interest is small, no more than 3 Hz. For this reason, the components of the filter are very large, consume a big area in silicon. Also, the off-chip filter can be tuned when needed to achieve the best performance.

6.5.2 Antenna Design

In this section, a differential dipole antenna is codesigned with the PLL IC. Since there is no buffer expected between the antenna and the output of the VCO, an increased loading impedance is preferred during the antenna design to lower the loading effect at the VCO output. However, on the other hand, a high output impedance will decrease the VCO output power due to the limited voltage swing. Therefore, a single-ended 400-Ohm load is found to be optimum with balancing the loading effect with relatively high output power based on the circuit simulation. As a result, a differential impedance of 800 Ohms is set to be the target for this antenna design instead of the typical single-ended 50-Ohm load.

The antenna has been simulated and fabricated in FR4 substrate with thickness of 57 mil. The simulation setup is shown in Fig. 6.17. To consider the parasitic effect between the IC and the antenna, the simulation includes simplified models for I/O pads, IC silicon substrate, ground layer and the dielectric layers based on the TSMC 65 nm process. Wirebond model provided by the simulation software has been used to estimate the

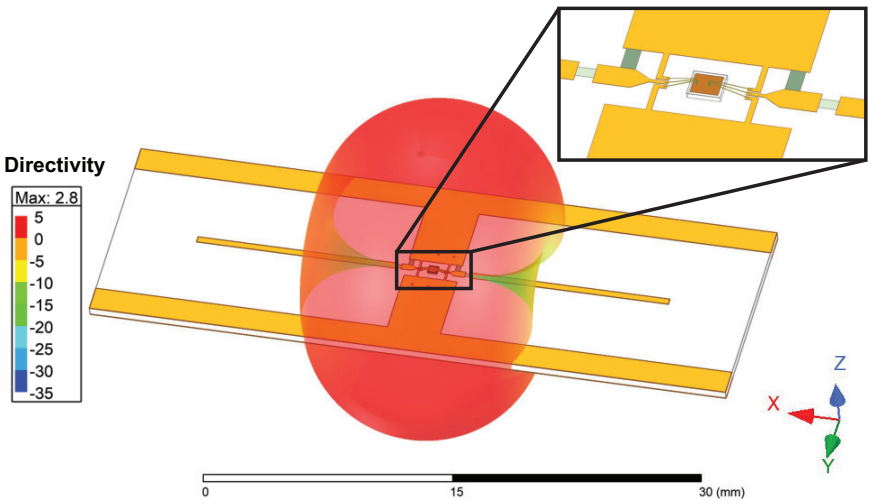

Figure 6.17: Simulation setup for the designed antenna integrating with chip design. The structure is overlaid with simulated far-field directivity pattern.

wirebond structure. After the wirebond, a one-stage matching network using capacitors is added to achieve a real-part impedance matching.

This design has been simulated using the Ansys Electronics Desktop (HFSS). The simulation result is presented in Fig. 6.18 which indicates a zero imaginary-part impedance at 1.5 GHz with a differential real-part impedance of 766 Ohms. The directivity of the antenna is also simulated and the result is overlaid on top of the simulation setup shown in Fig. 6.17, where the radiation pattern is omnidirectional with maximum directivity to be 2.8 dB.

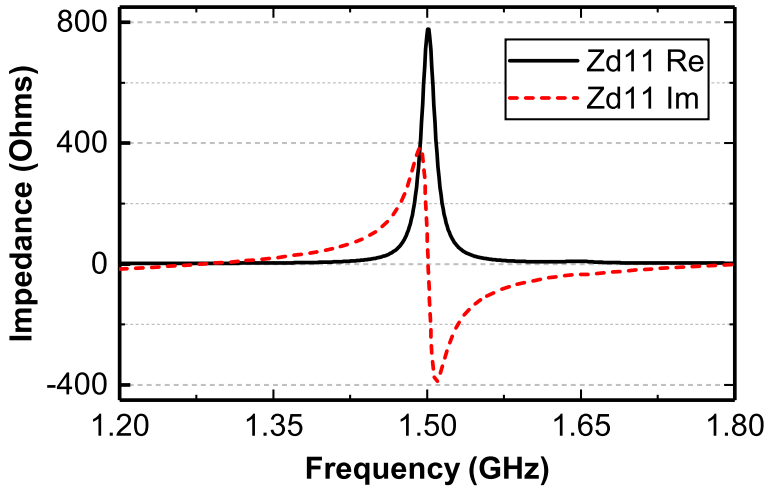

Figure 6.18: Simulated differential impedance of the designed antenna

Chapter 7

Experiment And Analysis

7.1 Test Setup

To verify the theory discussed and make a comparison between the RVCO and LCVCO based SIL radar for vital sign detection, multiple measurements and experiments have been conducted in the laboratory. Fig. 7.1 displays the SIL radar prototype PCBs, the photograph of the CMOS chips and set up for the experiment. Two boards have been manufactured for both the RVCO PLL and LCVCO PLL, each board has a reference crystal oscillator at 1 MHz with a low phase noise at the 1 Hz offset. The RVCO and LCVCO PLL boards have both an output frequency of 1.5 GHz with an output power of -10 dBm and -8 dBm respectively. The quality factor of the LCVCO is 8, while the K_{VCO} of both system is 6 MHz/V. The LCVCO chip measures 800x400 μm while the RVCO chip measures 600x300 μm, with a core size of 500x200 μm and 400x300 μm respectively. The LCVCO chip consumes a maximum power of 10 mW, which includes the analog, digital and RF blocks, while the RVCO has a maximum power consumption of only 7 mW. The phase noise was measured to be -98 dBc/Hz at 100 kHz offset and -95 dBc/Hz at 1 MHz offset for the LCVCO and RVCO respectively. Both systems used the same differential antenna in Fig. 7.1.

The first set up for the experiment is shown in Fig. 7.2. An actuator with a moving copper plate was placed in front of the patch antenna; the distance between the two was 10 cm. The plate is a square copper plate with a side length of 13 cm. The actuator mechanically

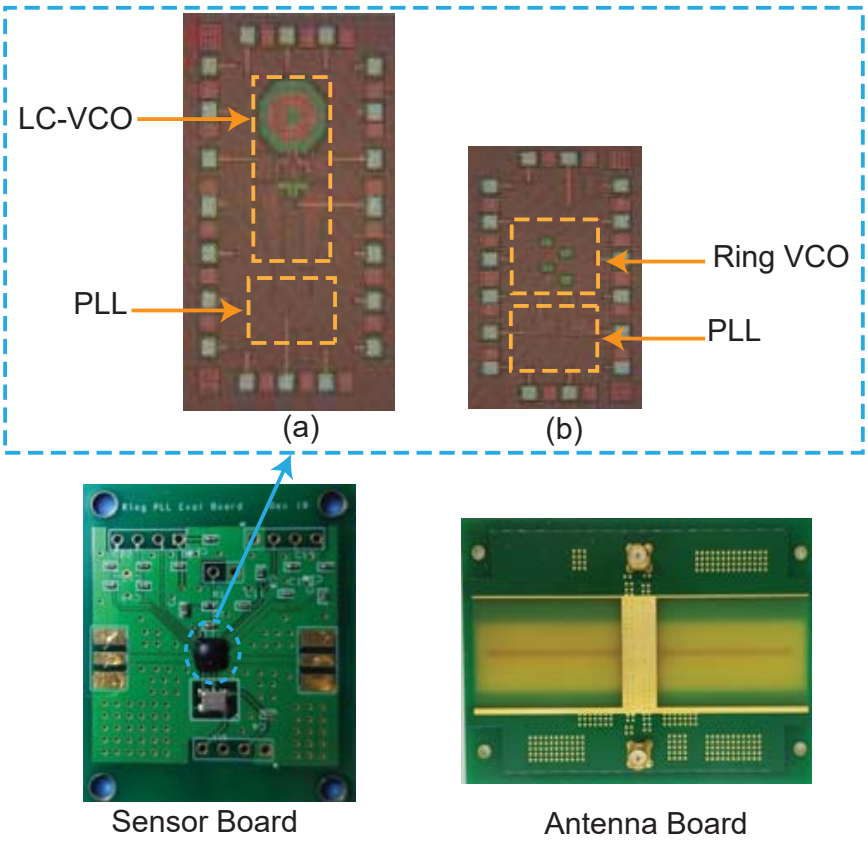

Figure 7.1: Top: Photograph of the SIL radar chip,(a)The LC chip and (b) the Ring chip. Bottom: Sensor board and measurements set-up.

move back and forth to simulate a displacement motion, while the vibration frequency can be adjusted by the user. Using the SIL radar board attached to the antenna, the demodulation of the injected signal from the actuator was done to retrieve the vibration frequency. The motion signal, the tuning voltage of the VCO, is then captured using NI-Daq signal acquisition system. Using MATLAB, the signal is further filtered. A digital low-pass filter is used with corner frequency of 4 Hz. Then, FFT is used to capture the frequency information in the voltage signal. At first, the actuator was placed in front the antenna and multiple measurements were done at different motion frequencies. Fig. 7.3 shows one sample of the experiments done when the actuator is programmed to move at a frequency of 1.3 Hz. The demodulated signal shows a clear peaks at the frequency of interest as well as the harmonics of the frequency. The RVCO based PLL design shows

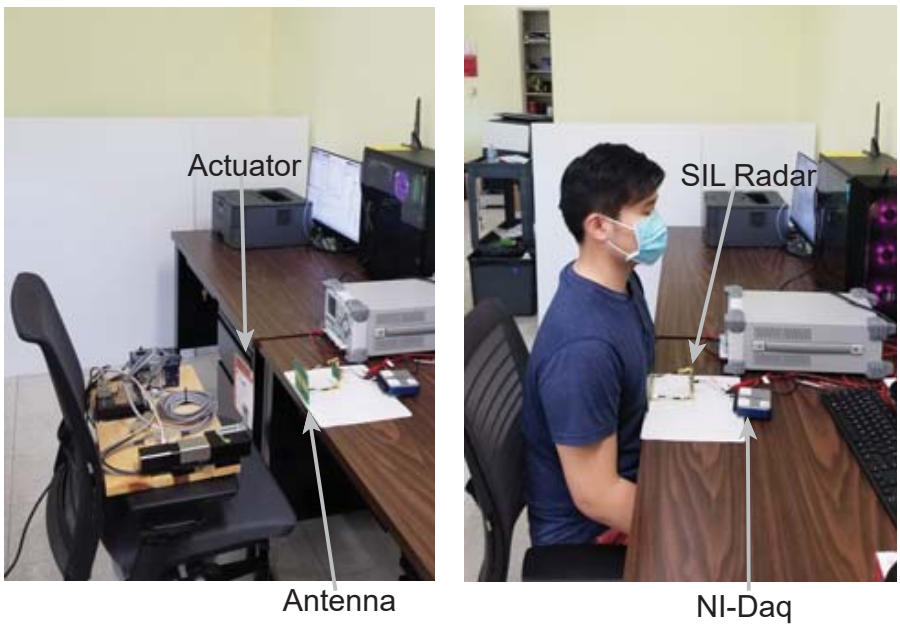

Figure 7.2: Photograph of the SIL radar chip, board and measurements set-up.

a better results then the LCVCO, as expected. Both systems have clear peaks at 1.3 Hz and the harmonic at 2.6 Hz, but the RVCO has stronger signal quality and a better SNR. In Fig. 7.3, the vertical axes are not at the same scale.

7.2 Vital Signs Measurement Results

To capture the vital signs measurements, a human subject sits on a chair while placing the system antenna on the chest, specifically on the sternum, the flat bone with no muscle in the front, as it has the less power loss for an EM wave transmitted to the heart. The intended using of this monitor is to be a wearable heart monitoring system. The SIL radar system is initialized at first to discard stationary clutter around the human subject, but since the antenna is placed directly on the chest, this latter is minimal, then measurements were taking for both PLL systems. The measurements were repeated for different human subjects at different times. The human subject was also asked to run to accelerate the heart rate beats and measurements were taken right after. Every time the vital signs were measured, they were verified using a commercially available smart watch with high

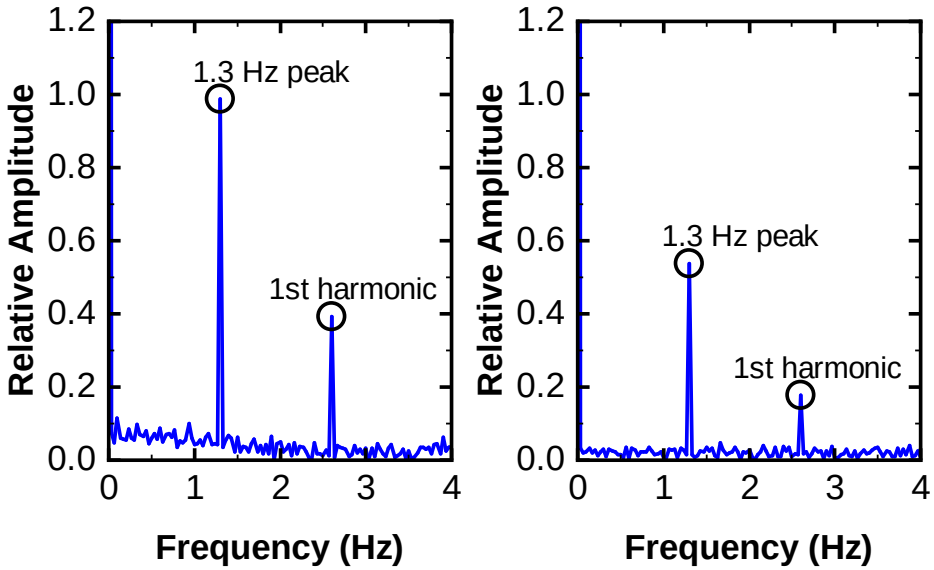

Figure 7.3: Measured actuator motion at 1.3 Hz using the RVCO (left) and the LC (right) based PLL radar system.

accuracy rate. Fig. 7.4 shows vital signs measurements sample for the LCVCO based SIL radar system and RVCO based SIL radar system. The main peaks indicates a 16 breaths per minutes respiration rate and 72 beats per minutes heart rate for the LCVCO and a 12.5 breaths per minutes respiration rate and 66.5 beats per minutes heart rate for the RVCO, which were both verified to be accurate. The RVCO based system demonstrates a stronger signal and lower SNR when compared to the LCVCO system.

To make a fair comparison between the two systems, the performance of RVCO based PLL system needs to be considered. Ring oscillators are known to be more prone to PVT variations. The histogram in Fig. 7.5 involving the plot between the number of samples and the output frequency of the Ring oscillator has been generated using Monte-Carlo simulation in 260 runs. It can be seen that the frequency can range between 1.15 and 1.9 GHz at different PVT. As a matter of fact, in the Ring oscillator design , this was taken into account and has an additional tuning to be able to overcome these variations and tune the oscillator back to the nominal value.

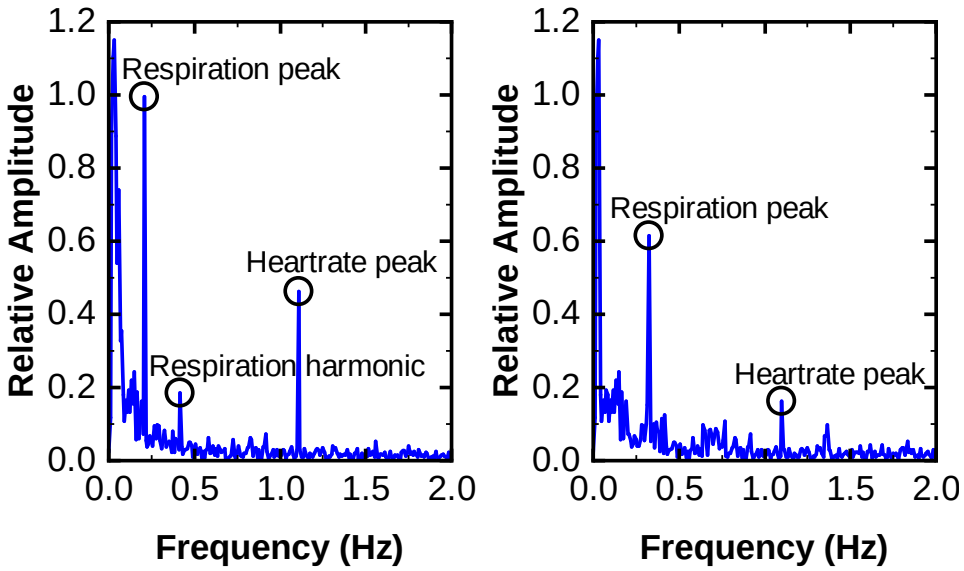

Figure 7.4: Measured respiration and heart rate signal using the RVCO (left) and the LC (right) based PLL radar system.

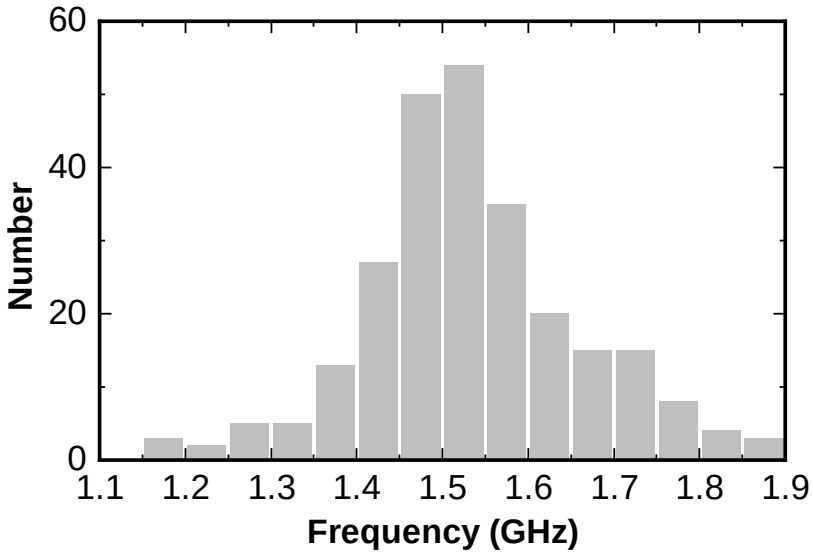

Figure 7.5: Monte-Carlo simulation of the operating frequency of the Ring oscillator with PVT variations.

7.3 Comparison Summary Of Both Systems

Fig. 7.4 shows the results from demodulation of the motion of the actuator at a frequency of 1.2 Hz using both the LCVCO and RVCO SIL radar systems. The RVCO system exhibits a better results compared to the LCVCO. Multiple measurements were done using both systems at different actuator's frequencies. The SNR was then measured and an average of 6 dB difference between the two systems. Then, the same was done by measuring vital signs. Table 7.1 shows the SNR measurements from 9 different trials for vital signs measurements. The measurements were all consistent while the RVCO exhibits a better SNR compared to the LCVCO by an average of 5.4 dB. When comparing the RVCO to the LCVCO SIL radar systems, with all the parameters the same and taking into consideration the output difference between the two, the ring exhibits better sensitivity and SNR compared to the LCVCO.

Table 8.1 lists recently reported Doppler radars for vital-sign detection using the same concept discussed in this paper. It's worth mentioning that most of the vital signs detectors are non-contact and are not meant to be wearable as the work done here. Although, the Radar designed in this work is meant to be wearable, it has also been tested for non-contact within 1 m and successful measurements were made. Making these non-contact measurements will provide a fair comparison between different detectors. In table 8.1, it's worth mentioning that in [51], measurements were done where the Radar was at 1.5 m from the antenna, in [52] was at 1 m, while in [56] was at 0.5 m. The results recorded from this work in table 8.1 were done at 1 m. Comparing different designs, the proposed SIL-radar in this work with the RVCO based PLL has the best detection quality with lowest area and power consumption among all recently reported works.

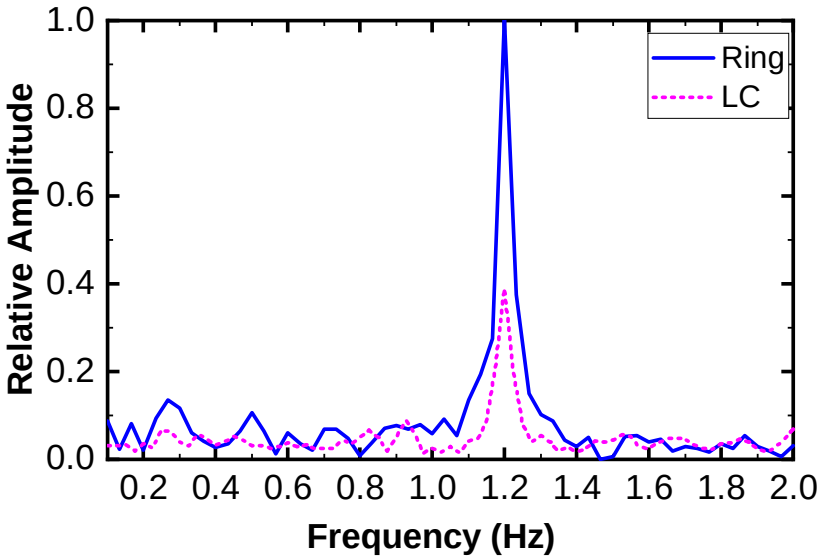

Figure 7.6: SIL radar Ring and LCVCO comparison with a 1.2 Hz actuator.

Table 7.1: SNR measurements while holding breath for the LCVCO ad RVCO comparison table

SNR (dB)	LCVCO	RVCO	Delta
Trial #1	16.35	21.66	5.31
Trial #2	13.81	19.90	6.10
Trial #3	16.28	21.24	4.96
Trial #4	14.97	20.01	5.05
Trial #5	14.25	19.54	5.30
Trial #6	14.18	19.82	5.64
Trial #7	14.12	20.11	5.99
Trial #8	15.05	19.99	4.939
Trial #9	14.99	20.67	5.68

Chapter 8

Conclusions

In this Chapter we summarize the findings presented and identify potential areas for future work.

8.1 Summary Of Work

So far, this wrok presented the analysis of self-injection locking of oscillators in PLL system to detect heart and respiration rate. The design and implementation of the PLL circuit were discussed. A study of sensitivity and phase noise of different oscillators architecture, LC and ring voltage controlled oscillators, was presented. Both theoretical and simulation results show that the RVCO is superior to the LCVCO in term of sensitivity. Although the RVCO has a poor phase noise compared to the LCVCO, it is not a problem in this design, because the system uses a PLL for demodulation and automatically filters out the low frequency noise, which is the frequency of interest.

In summary, two CMOS radar sensor chips has been designed based on the self-injection-locked oscillator and fabricated using TSMC 65 nm CMOS technology; one using an LCVCO and an RVCO. It uses an effective way to use SIL in a radar system to detect vital signs with minimal hardware. It expands the idea of using a phased locked loop (PLL) system as a demodulator and a single antenna, which makes it more concise. This work investigated and compared an LCVCO and an RVCO in terms of mainly sensitivity for motion detection and phase noise. It has been proven that the RVCO is superior to the LCVCO in terms of sensitivity while the phase noise is not much different as the

Table 8.1: Comparison table between reported CW radars for vital sign detection and this work

Author	Radar architecture	Freq (GHz)	Area (mm^2)	Power (mW)	Process	SNR (dB)
[51]	PSIL	5.8	0.3	10	65 nm	6*
[52]	SIL-DTFM	5.8	0.3	10	65 nm	10*
[56]	ILFD	24	1.03	63	180 nm	12*
This work "LC"	SIL	1.5	0.32	10	65 nm	12
This work "Ring"	SIL	1.5	0.18	7	65 nm	16

* The SNR values were estimated from the figures published.

frequency of interest is very small. The design of both systems, LCVCO based PLL and RVCO based PLL were done in TSMC 65 nm CMOS technology at 1.5 GHz frequency. The simulation and measurement results confirm the idea proposed. The RVCO shows better performance in terms of sensitivity, lower power consumption and smaller area compared to the LCVCO.

Doppler radars for vital-sign detection using the same concept discussed in this paper. It's worth mentioning that most of the vital signs detectors are non-contact and are not meant to be wearable as the work done here. Although, the Radar designed in this work is meant to be wearable, it has also been tested for non-contact within 1 m and successful measurements were made. Making these non-contact measurements will provide a fair comparison between different detectors. In table 8.1, it's worth mentioning that in [51], measurements were done where the Radar was at 1.5 m from the antenna, in [52] was at 1 m, while in [56] was at 0.5 m. The results recorded from this work in table 8.1 were done at 1 m. Comparing different designs, the proposed SIL-radar in this work with the RVCO based PLL has the best detection quality with lowest area and power consumption among all recently reported works.

8.2 Futher Consideration

The concept of using self-injection locking is very interesting and can be extended to be used in different applications. In fact, from the discussion above, the sensitivity of the system could be improved with increasing the oscillator output frequency. Also, since the sensing voltage, tuning voltage to the oscillator, is analog and need to be digitized for signal processing, this step could be omitted by using an all digital PLL (ADPLL). In an ADPLL, as it can be inferred from the name, all the PLL blocks are digital. The VCO is substituted with a digital controlled oscillator and the low pass filter is substituted with a discrete-time digital filter (generally second or third-order sigma-selta). Also, instead of the charge pump, a time error-to-charge or a time-to-digital converter (TDC) is used. The functionality of the ADPLL is very similar to the analog PLL. The PFD detects detects the frequency or phase mismatches between the divider output frequency and the reference frequency. Once the mismatch is detected, the charge pump and filter send a control word, instead of a tuning analog voltage, to either increase or decrease the DCO oscillation frequency. There are many advantages of the ADPLL compared to regular PLL. They are capable of outputting a signal with a low enough phase noise, at high enough frequencies to be used with RF systems [76]. The also consumes less power and area, as they have a greater flexibility in the loop bandwidth and does not require large capacitors. Moreover, ADPLL are less susceptible to process and noise variations than analog PLLs. An ADPLL was designed and simulated at the circuit level. All of the ADPLL blocks were designed and the ADPLL circuits are simulated operating at 24GHz and has proven that it can be successfully used for vital sign detection. The operation frequency and resolution of the TDC was carefully chosen to obtain the best performance.

8.3 Future Work

One of the unsolved issues in this project is dealing with the null point problem, dealing with CW radar. This happens when the distance between the radar and a target is a multiple of π. This problem is usually resolved by using an I/Q demodulator, having two signals from the heart, however in this case we have only one signal. One way to realise

the I/Q transmission is to use the SIL system with an envelop detector. In this manner, both the phase shift and amplitude variation of the received signal is processed. An other way to over come the null point is adding a delay to the transmitted signal to account of the 90 degrees phase shift.

Also, in the future, it requires testing the RCVO based SIL radar system with people with actual arrhythmia and correlate the results with that of the ECG.

Appendix A

Locking Range Of A 3-Stage Ring Oscillator Derivation

A.1 Introduction

In this appendix, the detailed derivation of equation 4.16 is presented. As mentioned in the main text, the analytical Perturbation Projection Vector (PPV) of a 3-stage ring oscillator is derived in [60] and, the voltage at the output node of a 3-stage ring oscillator can be expressed as,

$$V_3(t) = \begin{cases} \frac{1}{\sqrt{5}} I_o e^{(t/\tau)} & if \quad 0 \leq t < \frac{T}{2} \\ I_o(\frac{2}{\sqrt{5}} - 1)e^{(t/\tau)} & if \quad \frac{T}{2} \leq t < T \end{cases} \tag{A.1}$$

where I_o is the current at the output of the oscillator, τ is the RC time constant a the the output if each delay element and $T = 1/f_o = 2.8887\tau$ is the period of the ring oscillator.

A.2 PPV Phase Macromodel

In this section, we follow the analysis done [61] to obtain the locking range of the 3 stage ring oscillator. The derivation assumes an oscillator having a state space $\vec{x}(t)$. When the system is under perturbation of a $\vec{p}(t)$, the differential equation describing the system can be written as

$$\frac{d\vec{q}(\vec{x}(t))}{dt} + \vec{f}(\vec{x}) = \vec{p}(t) \tag{A.2}$$

where $q(.)$ and $f(.)$ are nonlinear functions. In the case the perturbation is very small, the case of injection locking, the variations in the amplitude can be small and the solution to equation A.2 cab written as

$$\vec{x}_p(t) = \vec{x}_s(t + \alpha(t)) \tag{A.3}$$

where $\vec{x}_s(t)$ is the T-periodic steady state solution with no perturbation signal. $\alpha(t)$ is the time shift in steady state or the phase shift can be written as,

$$\frac{d\alpha(t)}{dt} = \vec{v}_1^T(t + \alpha(t)) * \vec{b}(t) \tag{A.4}$$

where $\vec{v}_1^T$ is a T-periodic and is the PPV of the oscillator. This PPV results gives the phase sensitivity of the components of $x(t)$ to the injected signal $p(t)$. Once the PPV of the oscillator is analytically derived, the locking range can then be derived.

A.3 Locking Range Of The Ring Oscillator

In this derivation, a 3-stage ring oscillator is assumed. Also, let assume that all resistance and capacitance at the output of each stage are equal. ALso, the assumption that each delay element of the oscillator are ideal and can be expressed as [61],

$$s(V) = \begin{cases} A & if \quad V < 0 \\ -A & if \quad 0 \leq V \end{cases} \tag{A.5}$$

The 1-periodic representation of the PPV at the output of the ring oscillator, V_3 can be derived by substituting $t = f_o t$ in equation A.1,

$$X(t) = V_3^T(t/f_o) = \begin{cases} \frac{1}{\sqrt{5}} I_o e^{(t/f_o\tau)} & if \quad 0 \leq t < \frac{T}{2} \\ I_o(\frac{2}{\sqrt{5}} - 1)e^{(t/f_o/\tau)} & if \quad \frac{T}{2} \leq t < T \end{cases} \tag{A.6}$$

or

$$X(t) = V_3^T(t/f_o) = \begin{cases} \frac{1}{\sqrt{5}} I_o e^{(2.887t)} & if \quad 0 \leq t < \frac{1}{2} \\ I_o(\frac{2}{\sqrt{5}} - 1)e^{(2.887t)} & if \quad \frac{1}{2} \leq t < T \end{cases} \tag{A.7}$$

Let $A_1 = 2.887$, $A_2 = \frac{1}{\sqrt{5}}$, and $A_3 = \frac{2}{\sqrt{5}} - 1$, equation B.49 can be simplified as,

$$X(t) = \begin{cases} A_2 I_o e^{(A_1 t)} & if \quad 0 \leq t < \frac{1}{2} \\ I_o A_3 e^{(A_1 t)} & if \quad \frac{1}{2} \leq t < T \end{cases} \tag{A.8}$$

Let assume that the ring oscillator was injected with a sinusoidal injection current of

$$p(\phi_i(t)) = I_i \sin(2\pi\phi_i(t)) \qquad if \quad 0 \leq \phi_i < 1 \tag{A.9}$$

where $\phi_i(t) = f_i t$ and f_i is the frequency of the injected signal. Next, from equation (14) in [61], averaging the fast phase shift of injected signal and retaining the slow $\Delta\phi(t)$ variation of the actual signal, the sinusoidal can be expressed as

$$g(\Delta\phi(t)) = \int_0^1 X(\Delta\phi(t) + \phi_i(t)) * p(\phi_i)\, d\phi_i \tag{A.10}$$

Applying equation B.51 in the ring oscillator, we can obtain

$$g(\Delta\phi(t)) = \frac{1}{\sqrt{4\pi^2 + A_1^2}} \frac{I_i}{I_o} \sin(2 * pi\Delta\phi(t) + \zeta) * [A_2(e^{(A_1/2)} + 1] - A_3(e^{(A_1)} + e^{(A_1/2)} \tag{A.11}$$

where

$$\sin(\zeta) = \frac{2\pi}{\sqrt{4\pi^2 + A_1^2}} \tag{A.12}$$

From [61], the Gen-Adler's equation is expressed as

$$\frac{\Delta\phi}{dt} = -(f_i - f_o) + f_o g(\Delta\phi(t)) \tag{A.13}$$

Then, we can solve for when the VCO is locked, ie. $\frac{d\Delta\phi}{dt} = 0$,

$$\frac{f_i - f_o}{f_o} = \frac{1}{\sqrt{4\pi^2 + A_1^2}} \frac{I_i}{I_o} \sin(2 * pi\Delta\phi(t) + \zeta) * [A_2(e^{(A_1/2)} + 1] - A_3(e^{(A_1)} + e^{(A_1/2)} \tag{A.14}$$

The locking range happens when $g(\Delta\phi(t)$ is maximum, and so equation B.55 is maximum when the sine term is unity.

$$|\Delta f_o|_{max} = \frac{1}{\sqrt{4\pi^2 + A_1^2}} \frac{I_i}{I_o} [A_2(e^{(A_1/2)} + 1] - A_3(e^{(A_1)} + e^{(A_1/2)}) \tag{A.15}$$

or the locking range of the 3 stage ring oscillator is

$$\omega_{LR} = |\Delta f_o|_{max} = 0.6773 \frac{I_i}{I_o} \tag{A.16}$$

and

$$\Delta\omega(t) = 0.6773 \frac{R I_i \omega_o}{V} \cos(\phi(t) + 0.1446) \tag{A.17}$$

Appendix B

Locking Range Of A 4-Stage Ring Oscillator Derivation

B.1 Introduction

In this appendix, the detailed derivation of equation 4.16 is presented. The analytical Perturbation Projection Vector (PPV) of a 3-stage ring oscillator was already derives in [60], however not such can be found in literature for 4-stage ring oscillators. In this application, the goal is to use a 4-stage ring oscillator because a differential architecture is favored to reduce noise and suppress the common mode rejection ratio. A differential architecture can not be used with a 3-stage ring oscillator. Thus, the need to derive the locking range of the 4-stage ring oscillator.

B.2 The PPV derivation methodology

In [60], the PPV of a 3-stage ring oscillator is derived analytically for phase noise estimation. In this work, the same methodology was used to derive the PPV for a 4-stage ring oscillator to derive the locking range of the latter. The idea is to assume that all the delay elements are ideal inverters and have ideal switching characteristics while all deviation from non-idealities are captured in the resistance and capacitance at the output of the delays. The main concept behind the analytical PPV is using Floquet analysis by solving the linear periodically time-varying (LPTV) system of equations when linearizing the ring oscillator in steady state [60]. To capture the PPV, the phase equation is obtained by

following Floquet analysis by following these steps,

- 1) First, the differential equation of ring oscillator is obtained, equation B.1.
- 2) The exact analytical oscillator solution of B.1 in terms of the ring oscillator' specification such R, C and period T
- 3) The LPTV differential is derived to capture the perturbation of the oscillator around the nominal steady state, equation B.21
- 4) The B.21 is solved to obtain the general solution
- 5) Calculate the 4x4 monodromy matrix of the RVCO
- 6) Then, using the general solution, the eigen-solution obtained to find the PPV analytically.

B.3 The PPV Derivation Of A 4-Stage Ring Oscillator

The equation of the RCVCO can be derived from Fig. B.1 as

$$\dot{v}_1(t) = \frac{f(v_4) - v_1}{\tau}, \qquad \dot{v}_2(t) = \frac{f(v_1) - v_2}{\tau}, \qquad \dot{v}_3(t) = \frac{f(v_2) - v_3}{\tau}, \qquad \dot{v}_4(t) = \frac{f(v_3) - v_4}{\tau} \tag{B.1}$$

where $\tau = RC$ is the time constant at the output of each stage, and $f(v_n)$ is the ideal inverter characteristic and is defined as,

$$f(v) = \begin{cases} -1 & if \quad v > 0 \\ 1 & if \quad otherwise \end{cases} \tag{B.2}$$

Let assume $x(t) = v_1(t)$ to be the T-periodic and assuming both positive and negative symmetry, then

$$x(t) = -(1 + E_o)\exp(-t/\tau) + 1 \quad if \quad 0 \le t \le T/2 \tag{B.3}$$

here the initial condition $x(0) = -E_o$ and because of symmetry

$$x(T/2) = E_o \qquad => \qquad E_o = -(1 + E_o)\exp(-T/2\tau) + 1 \tag{B.4}$$

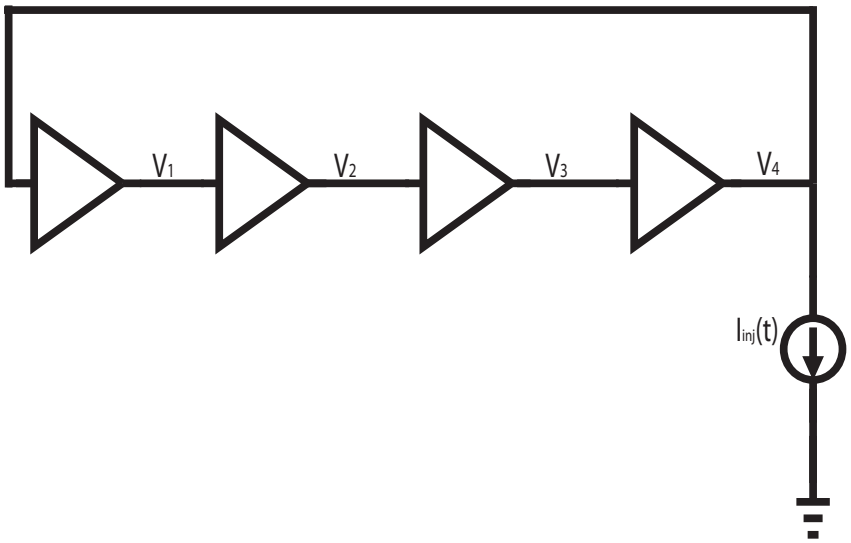

Figure B.1: 4-Stage ring VCO.

$$E_o = \tanh \frac{T}{4\tau} \tag{B.5}$$

From the delay symmetry, for an N stage delay element ring oscillator, the voltage at the nth node is

$$v_n(t) = x(t - \frac{(N-n+1)(N-1)T}{2N}) \tag{B.6}$$

Applying equation B.6 we can find expression for voltages at each output node of the 4-stage ring oscillator,

$$v_2(t) = x(t - \frac{9T}{8}), \qquad v_3(t) = x(t - \frac{6T}{8}), and \qquad v_4(t) = x(t - \frac{3T}{8}) \tag{B.7}$$

Looking at these voltages, we can plot their steady state waveforms and find that the find the second zero cross point happens when $t = T/2N$ a,d in the case of the 4-stage RVCO $t = T/8$

$$0 = -(1 + E_o)\exp(-T/8\tau) + 1 \implies \exp(-T/8\tau) = 1 + \tanh \frac{T}{4\tau} \tag{B.8}$$

$$\exp(-T/8\tau) = 1 + \frac{1 - \exp(-T/2\tau)}{1 + \exp(-T/2\tau)} \tag{B.9}$$

Simplifying the above equation,

$$2 - \exp(T/8\tau) - \exp(-3T/8\tau) = 0 \tag{B.10}$$

Let $y = \exp(T/8\tau)$, equation B.10 becomes

$$y^4 - 2y^3 + 1 = 0 \tag{B.11}$$

and generally for an N stage oscillator,

$$y^N - 2y^{N-1} + 1 = 0 \tag{B.12}$$

Unfortunately, equation B.11 can not be solved analytically and get a generalized solution. As a result from this point on, the equation needs to be solved for each case of numbers of stages for the oscillator. Solving equation B.11, we have $y = 1.8393$ and $T = 8\tau \ln y$. As a result, we can solve for E_o from equation B.13,

$$E_o = \tanh \frac{8 \ln y}{4\tau} \approx y - 1 = 0.8393 \tag{B.13}$$

Now, we can write the periodic steady-state equation for the oscillator as,

$$v_1(t) = x(t) = \begin{cases} 1 - ye^{(-t/\tau)} & if \quad 0 \le t < \frac{T}{2} \\ -1 + e^{(-(t-T/2)/\tau)} & if \quad \frac{T}{2} \le t < T \end{cases} \tag{B.14}$$

$$v_2(t) = x(t - \frac{9T}{8}), \qquad v_3(t) = x(t - \frac{6T}{8}), and \qquad v_4(t) = x(t - \frac{3T}{8}) \tag{B.15}$$

Let's define the periodic steady-state form as $x_s(t) = [v_1(t), v_2(t), v_3(t), v_4(t)]^T$ the derivative of $x_s(t)$ is

$$\dot{v}_1(t) = \dot{x}(t) = \begin{cases} 1 - ye^{(-t/\tau)} & if \quad 0 \le t < \frac{T}{2} \\ -1 + e^{(-(t-T/2)/\tau)} & if \quad \frac{T}{2} \le t < T \end{cases} \tag{B.16}$$

$$\dot{v}_2(t) = \dot{x}(t - \frac{9T}{8}), \qquad \dot{v}_3(t) = \dot{x}(t - \frac{6T}{8}), and \qquad \dot{v}_4(t) = \dot{x}(t - \frac{3T}{8}) \tag{B.17}$$

while the initial condition is $\dot{x}_s(0+) = \frac{1+E_o}{\tau}[1, y^{-3}, y^{-2}, y^{-1}]$. In step 3, the LPTV needs to be found. The goal is to linearize equations‘B.1 about the periodic steady state obtained above. The ideal inverter characteristic can be written when $x = 0$ as $f'(x) = -2\delta(t)$. The forward LPTV of the system follow the form

$$\dot{n}(t) + G(t)n(t) = 0 \tag{B.18}$$

where G(t) is the 4x4 T-periodic matrix

$$G(t) = \begin{bmatrix} 1 & 0 & 0 & -f'(v_4) \\ -f'(v_1) & 1 & 0 & 0 \\ 0 & -f'(v_2) & 1 & 0 \\ 0 & 0 & -f'(v_3) & 1 \end{bmatrix} \tag{B.19}$$

or,

$$G(t) = \frac{1}{\tau}\begin{bmatrix} 1 & 0 & 0 & 2\delta(v_4) \\ 2\delta(v_1) & 1 & 0 & 0 \\ 0 & 2\delta(v_2) & 1 & 0 \\ 0 & 0 & 2\delta(v_3) & 1 \end{bmatrix} \tag{B.20}$$

Then the adjoint system can be represented as,

$$\dot{n}(t) + G^T(t)n(t) = 0 \tag{B.21}$$

Looking at the waveform $v_1(t), v_2(t), v_3(t) and v_4(t)$ and the zero crossing points, the matrix $G(t)$ can be rewritten as,

$$G(t) = \begin{bmatrix} 1 & 0 & 0 & G_{14} \\ G_{21} & 1 & 0 & 0 \\ 0 & G_{32} & 1 & 0 \\ 0 & 0 & G_{43} & 1 \end{bmatrix} \tag{B.22}$$

this equation is valid for $0 < t < T$ where,

$$G_{14} = \frac{2}{|x'(t^*)|}(\delta(t) + \delta(t - \frac{T}{2})) \tag{B.23}$$

$$G_{21} = \frac{2}{|x'(t^*)|}(\delta(t - \frac{T}{8}) + \delta(t - \frac{5T}{8})) \tag{B.24}$$

$$G_{32} = \frac{2}{|x'(t^*)|}(\delta(t - \frac{2T}{8}) + \delta(t - \frac{6T}{8})) \tag{B.25}$$

$$G_{43} = \frac{2}{|x'(t^*)|}(\delta(t - \frac{7T}{8}) + \delta(t - \frac{4T}{8})) \tag{B.26}$$

and $t^* = T/8$, when $x(t)$ crosses the zero. At this point the slope is $x'(t^*) = 1/\tau$

In step 4, the adjoint LPTV system needs to be solved. Let's $S' = 2/(\tau|x'(t^*)|$ and expanding the LPTV system as $\dot{z}(t) + G^T(t)z(t) = 0$. After some tedious algebra, the solution can be written as,

$$z_1(t) = [z_1(0) + S'((z_2(0)u(t - \frac{T}{8})) + (z_2(0) + S'z_3(0))u(t - \frac{5T}{8})))]e^{t/\tau} \tag{B.27}$$

$$z_2(t) = [z_2(0) + S'((z_3(0)u(t - \frac{2T}{8})) + (z_3(0) + S'z_4(0) + S'z_1(0))u(t - \frac{6T}{8}))]e^{t/\tau} \tag{B.28}$$

$$z_3(t) = [z_3(0) + S'((z_4(0)u(t - \frac{3T}{8})) + (z_4(0) + 2S'z_1(0) + S'z_2(0))u(t - \frac{7T}{8}))]e^{t/\tau} \tag{B.29}$$

$$z_4(t) = [z_4(0) + S'((z_1(0)u(t - \frac{2T}{8})) + (z_1(0) + S'z_2(0))u(t - \frac{4T}{8}))]e^{t/\tau} \tag{B.30}$$

Now, we need to find the Monodromy matrix of the adjoint LPTV system. First, we evaluate **??-??** when $t = T$ for the initial condition,

$$M_A(t) = \begin{bmatrix} 1 & 2S' & S'^2 & 0 \\ S'^3 & 1 & 2S' & S'^2 \\ 3S'^2 & S'^3 & 1 & 2S' \\ 2S' & S'^2 & 0 & 1 \end{bmatrix} \tag{B.31}$$

Recall that $y^8 = e(T/\tau$ and $S' = 2/(\tau|x'(t^*)|$, equation B.31 becomes,

$$M_A(t) = \begin{bmatrix} 9 & 4 & 4 & 0 \\ 8 & 9 & 4 & 4 \\ 12 & 8 & 9 & 4 \\ 4 & 4 & 0 & 1 \end{bmatrix} y^8 \tag{B.32}$$

The characteristic polynomial can be expressed as,

$$\lambda^4 + 28\lambda^3 + +14\lambda^2 - 20\lambda + 89 \tag{B.33}$$

as a result, the eigenvalues are

$$\lambda = 1, \qquad \lambda = 13 + 4\sqrt{5} = y^5.06, and \qquad \lambda = 13 - 4\sqrt{5} = y^2.3 \tag{B.34}$$

and the eigen-decomposition is

$$\begin{bmatrix} -\sqrt{5} & \sqrt{5} & 1 \\ 3 & 3 & -1 \\ 2-\sqrt{5} & 2+\sqrt{5} & -1 \\ 1 & 1 & 1 \end{bmatrix} \begin{bmatrix} 13-4\sqrt{5} & 0 & 0 & 0 \\ 0 & 13+4\sqrt{5} & 0 & 0 \\ 0 & 0 & 1 & 0 \\ 0 & 0 & 0 & 1 \end{bmatrix} \tag{B.35}$$

Now, we are at the last step of the derivation and ready to find the PPV pf the oscillator. The eigen vector corresponding to the periodic Floquet multiplier can be written as $[-\sqrt{5}\sqrt{5}1]$ and the scaled PPV can be written as

$$V_{11}(t) = [-\sqrt{5} + 2(3u(t - \frac{T}{8})) + (3 + 2(2 - \sqrt{5}))u(t - \frac{5T}{8})]e^{t/\tau} \tag{B.36}$$

$$V_{21}(t) = [3 + 2((2 - \sqrt{5})u(t - \frac{2T}{8})) + ((2 - \sqrt{5}) + 2 - 4\sqrt{5})u(t - \frac{6T}{8})]e^{t/\tau} \tag{B.37}$$

$$V_{31}(t) = [(2 - \sqrt{5}) + 2((1 - 2\sqrt{5})u(t - \frac{3T}{8})) + (1 - 2\sqrt{5} + 12)u(t - \frac{7T}{8})]e^{t/\tau} \tag{B.38}$$

$$V_{41}(t) = [1 - 2\sqrt{5}u(t) + (-2\sqrt{5} + 12)u(t - \frac{4T}{8})]e^{t/\tau} \tag{B.39}$$

Now, we need to normalize the equation above against $\dot{x}_s(t)$. Using $\dot{x}_s(0+) = \frac{1+E_o}{\tau}[1, y^{-3}, y^{-2}, y^{-1}]$, we can write

$$K_A = V_1^T(0+)\dot{x}_s(t) \tag{B.40}$$

$$K_A = \frac{y}{\tau}[-\sqrt{5}, 3, 2 - \sqrt{5}, 1][1, y^{-3}, y^{-2}, y^{-1}] \tag{B.41}$$

$$K_A = \frac{y^3 - 1}{\tau(y^3 + 1)}[-\sqrt{5} + 3y^{-1} + (2 - \sqrt{5})y^{-2}] + y^{-3}] \tag{B.42}$$

We can obtain the analytical expression for the PPV for the four stage ring oscillator as

$$PPV(t) = \frac{\tau(y^3 + 1)}{(y^3 - 1)} \begin{bmatrix} -\sqrt{5} + 2(3u(t - \frac{T}{8})) + (3 + 2(2 - \sqrt{5}))u(t - \frac{5T}{8}) \\ 3 + 2((2 - \sqrt{5})u(t - \frac{2T}{8})) + ((2 - \sqrt{5}) + 2 - 4\sqrt{5})u(t - \frac{6T}{8}) \\ (2 - \sqrt{5}) + 2((1 - 2\sqrt{5})u(t - \frac{3T}{8})) + (1 - 2\sqrt{5} + 12)u(t - \frac{7T}{8}) \\ 1 - 2\sqrt{5}u(t) + (-2\sqrt{5} + 12)u(t - \frac{4T}{8}) \end{bmatrix} e^{t/\tau} \tag{B.43}$$

where $K_s = -\sqrt{5} + 3y^{-1} + (2-\sqrt{5})y^{-2}] + y^{-3}$. So, we have an expression for the PPV_4 to compute the locking range of the 4-stage ring oscillator and can be written as,

$$PPV_4 = \frac{\tau(y^3+1)}{(y^3-1)}[1 - 2\sqrt{5}u(t) + (-2\sqrt{5}+12)u(t-\frac{4T}{8})]e^{t/\tau} \tag{B.44}$$

$$PPV_4 = \frac{\tau(y^3+1)}{(y^3-1)}[1 - 2\sqrt{5} + (-2\sqrt{5}+12)u(t-\frac{1T}{2})]e^{t/\tau} \tag{B.45}$$

$$PPV_4 = \begin{cases} 3.8592e^{(t/\tau)} & if \quad 0 \le t < \frac{T}{2} \\ -4.05e^{(t/\tau)} & if \quad \frac{T}{2} \le t < T \end{cases} \tag{B.46}$$

B.4 Locking Range Of A 4-Stage Ring Oscillator

In this derivation, we follow the steps from appendix A. The 1-periodic representation of the PPV at the output of the ring oscillator, V_3 can be derived by substituting $t = f_o t$ in equation A.1,

$$X(t) = V_4^T(t/f_o) = \begin{cases} 3.8592I_o e^{(t/f_o\tau)} & if \quad 0 \le t < \frac{T}{2} \\ -4.05I_o e^{(t/f_o/\tau)} & if \quad \frac{T}{2} \le t < T \end{cases} \tag{B.47}$$

or

$$X(t) = V_4^T(t/f_o) = \begin{cases} 3.8592I_o e^{(4.857t)} & if \quad 0 \le t < \frac{1}{2} \\ -4.05I_o e^{(4.857t)} & if \quad \frac{1}{2} \le t < T \end{cases} \tag{B.48}$$

Let $A_1 = 4.875$, $A_2 = 3.8592$, and $A_3 = -4.508$, equation B.49 can be simplified as,

$$X(t) = \begin{cases} A_2 I_o e^{(A_1 t)} & if \quad 0 \le t < \frac{1}{2} \\ I_o A_3 e^{(A_1 t)} & if \quad \frac{1}{2} \le t < T \end{cases} \tag{B.49}$$

Let assume that the ring oscillator was injected with a sinusoidal injection current of

$$p(\phi_i(t)) = I_i \sin(2\pi\phi_i(t)) \qquad if \quad 0 \le \phi_i < 1 \tag{B.50}$$

where $\phi_i(t) = f_i t$ and f_i is the frequency of the injected signal. Next, from equation (14) in [61], averaging the fast phase shift of injected signal and retaining the slow $\Delta\phi(t)$ variation of the actual signal, the sinusoidal can be expressed as

$$g(\Delta\phi(t)) = \int_0^1 X(\Delta\phi(t) + \phi_i(t)) * p(\phi_i)\, d\phi_i \tag{B.51}$$

Applying equation B.51 in the ring oscillator, we can obtain

$$g(\Delta\phi(t)) = \frac{1}{\sqrt{4\pi^2 + A_1^2}} \frac{I_i}{I_o} \sin(2 * pi\Delta\phi(t) + \zeta) * [A_2(e^{(A_1/2)} + 1] - A_3(e^{(A_1)} + e^{(A_1/2)} \quad \text{(B.52)}$$

where

$$\sin(\zeta) = \frac{2\pi}{\sqrt{4\pi^2 + A_1^2}} \quad \text{(B.53)}$$

From [61], the Gen-Adler's equation is expressed as

$$\frac{\Delta\phi}{dt} = -(f_i - f_o) + f_o g(\Delta\phi(t)) \quad \text{(B.54)}$$

Then, we can solve for when the VCO is locked, ie. $\frac{d\Delta\phi}{dt} = 0$,

$$\frac{f_i - f_o}{f_o} = \frac{1}{\sqrt{4\pi^2 + A_1^2}} \frac{I_i}{I_o} \sin(2 * pi\Delta\phi(t) + \zeta) * [A_2(e^{(A_1/2)} + 1] - A_3(e^{(A_1)} + e^{(A_1/2)} \quad \text{(B.55)}$$

The locking range happens when $g(\Delta\phi(t)$ is maximum, and so equation B.55 is maximum when the sine term is unity.

$$|\Delta f_o|_{max} = \frac{1}{\sqrt{4\pi^2 + A_1^2}} \frac{I_i}{I_o} [A_2(e^{(A_1/2)} + 1] - A_3(e^{(A_1)} + e^{(A_1/2)}) \quad \text{(B.56)}$$

or the locking range of the 4-stage ring oscillator is

$$\omega_{LR} = |\Delta f_o|_{max} = 0.6112 \frac{I_i}{I_o} \quad \text{(B.57)}$$

and

$$\Delta\omega(t) = 0.6112 \frac{RI_i\omega_o}{V} \cos(\phi(t) + 0.446) \quad \text{(B.58)}$$

References

[1] W. F. Boron and E. L. Boulpaep, *Medical Physiology.* Philadelphia, PA: Elsevier, 2017.

[2] "Atrial fibrillation (afib) and strokes," *National Stroke Association.*, pp. 1–2, April 2015, https://www.cdc.gov/stroke/facts.htm.

[3] J. G. Betts and K. A. Young, *Anatomy and physiology.* SOpenStax, 2013.

[4] M. I. Skolnik, "Radar," *Encyclopedia Britannica*, November 2020, https://www.britannica.com/technology/radar. Accessed 13 September 2021.

[5] B. J. Hansen and V. V. Fedorov, "Mechanisms of normal and dysfunctional sinoatrial nodal excitability and propagation," *Cardiac Electrophysiology: From Cell to Bedside*, vol. Seventh Edition, 2018.

[6] Vol. Seventh Edition, 2018, https://ecgwaves.com/.

[7] S. BI, "Cardiac motion monitor based on contact doppler radar technology," Ph.D. dissertation, University of California at Davis, Davis, Ca, 2018.

[8] T. Horng, "Self-injection-locked radar: An advance in continuous-wave technology for emerging radar systems," in *2013 Asia-Pacific Microwave Conference Proceedings (APMC)*, Nov 2013, pp. 566–569.

[9] S. L. P. Gray, P. Hurst and R. Meyer, *Analysis and Design of Analog Integrated Circuits.* New York: Wiley, 2001.

[10] C. Banerjee, *PLL performance, simulation and design.* SNAA106C, 2017.

[11] S. Kingsley and S. Quegan, *Understanding Radar Systems.* Mendham,NJ: Scitech publishing, Inc, 1999.

[12] T. Horng, "Self-injection-locked radar: An advance in continuous-wave technology for emerging radar systems," in *2013 Asia-Pacific Microwave Conference Proceedings (APMC)*, Nov 2013, pp. 566–569.

[13] F. Fioranelli, J. Le Kernec, and S. A. Shah, "Radar for health care: Recognizing human activities and monitoring vital signs," *IEEE Potentials*, vol. 38, no. 4, pp. 16–23, July 2019.

[14] "Stroke facts," *Centers for Disease Control and Prevention*, 2021, https://www.cdc.gov/stroke/facts.htm.

[15] S. S. Dutt and S. Paknikar, "Holter monitoring- tests, procedures and results," *MD India*, May 2015, https://www.cdc.gov/stroke/facts.htm.

[16] M. Roberg, J. Hoversten, and Z. Popovic, "Efficient and linear transmitter concept for future high-power solid-state radar systems." Invited presentation at the 2010 CNC/USNC/URSI Radio Science Metting, Boulder, CO, 2011.

[17] A. D. Berny, "Analysis and design of wideband lc vcos," Ph.D. dissertation, University of California at Berkeley, Berkeley, Ca, 2006, http://www.eecs.berkeley.edu/Pubs/TechRpts/2006/EECS-2006-50.html.

[18] C. Caro and J. Bloice, "Contactless apnea detector based on radar," *The Lancet*, vol. 298, no. 7731, pp. 959–961, Octobre 1971.

[19] J. C. Lin, J. Kiernicki, M. Kiernicki, and P. B. Wollschlaeger, "Microwave apexcardiography," *IEEE Transactions on Microwave Theory and Techniques*, vol. 27, no. 6, pp. 618–620, Jun 1979.

[20] S. R. C. J. Seals and S. Sharpe, *Medical Physiology.* Atlanta, GA,: Georgia Tech Research Institute Biomedical Division, 1986.

[21] Kun-Mu Chen, Yong Huang, Jianping Zhang, and A. Norman, "Microwave life-detection systems for searching human subjects under earthquake rubble or behind barrier," *IEEE Transactions on Biomedical Engineering*, vol. 47, no. 1, pp. 105–114, Jan 2000.

[22] I. Arai, "Survivor search radar system for persons trapped under earthquake rubble," in *APMC 2001. 2001 Asia-Pacific Microwave Conference (Cat. No.01TH8577)*, vol. 2, Dec 2001, pp. 663–668 vol.2.

[23] C. Li, V. M. Lubecke, O. Boric-Lubecke, and J. Lin, "A review on recent advances in doppler radar sensors for noncontact healthcare monitoring," *IEEE Transactions on Microwave Theory and Techniques*, vol. 61, no. 5, pp. 2046–2060, May 2013.

[24] Xing Yun, E. C. Fear, and R. H. Johnston, "Compact antenna for radar-based breast cancer detection," *IEEE Transactions on Antennas and Propagation*, vol. 53, no. 8, pp. 2374–2380, Aug 2005.

[25] D. Gibbins, M. Klemm, I. J. Craddock, J. A. Leendertz, A. Preece, and R. Benjamin, "A comparison of a wide-slot and a stacked patch antenna for the purpose of breast cancer detection," *IEEE Transactions on Antennas and Propagation*, vol. 58, no. 3, pp. 665–674, March 2010.

[26] X. Li, J. Yan, M. Jalilvand, and T. Zwick, "A compact double-elliptical slot-antenna for medical applications," in *2012 6th European Conference on Antennas and Propagation (EUCAP)*, March 2012, pp. 3677–3680.

[27] N. T. P. Van, L. Tang, N. D. Minh, F. Hasan, and S. Mukhopadhyay, "Extra wide band 3d patch antennae system design for remote vital sign doppler radar sensor detection," in *2017 Eleventh International Conference on Sensing Technology (ICST)*, Dec 2017, pp. 1–5.

[28] O. Boric-Lubecke, V. M. Lubecke, A. Host-Madsen, D. Samardzija, and K. Cheung, "Doppler radar sensing of multiple subjects in single and multiple antenna systems," in *TELSIKS 2005 - 2005 uth International Conference on Telecommunication in ModernSatellite, Cable and Broadcasting Services*, vol. 1, Sep. 2005, pp. 7–11 vol. 1.

[29] J. M. Park, D. H. Choi, and S. O. Park, "Wireless vital signal detection systems and its applications at 1.9ghz and 10ghz [biomedical applications]," in *IEEE Antennas and Propagation Society International Symposium. Digest. Held in conjunction with: USNC/CNC/URSI North American Radio Sci. Meeting (Cat. No.03CH37450)*, vol. 4, June 2003, pp. 747–750 vol.4.

[30] E. S. P. R. Henry Blackburn, Ancel Keys and S. Punsar, "The electrocardiogram in population studies: a classification system," *Circulation*, vol. 6, no. 21, pp. 1160–1175, 1960.

[31] "What is atrial fibrillation (afib or af)?" *American Heart Association editorial*, 2016.

[32] T. N. J. James L Wells, W AH MacLean and A. L. Waldo, "Characterization of atrial flutter. studies in man after open heart surgery using fixed atrial electrodes," *Circulation*, vol. 3, no. 60, p. 665–673, 1979.

[33] D. S. C. Li, M. Tofighi and T.-Z. J. H. (Eds), *Principles and aplications of RF/microwave in healthcare and biosensing: Biomedical radars for monitoring health.* Elsevier Inc, 2017.

[34] F. Wang, C. Li, C. Hsiao, T. Horng, J. Lin, K. Peng, J. Jau, J. Li, and C. Chen, "A novel vital-sign sensor based on a self-injection-locked oscillator," *IEEE Transactions on Microwave Theory and Techniques*, vol. 58, no. 12, pp. 4112–4120, Dec 2010.

[35] F.Wang, C. Li, C. Hsiao, T. Horng, J. Lin, K. and J. Jau and J. Li, and C. Chen, "An injection-locked detector for concurrent spectrum and vital sign sensing," in *2010 IEEE MTT-S International Microwave Symposium*, May 2010, pp. 768–771.

[36] F. Wang, T. Horng, K. Peng, J. Jau, J. Li, and C. Chen, "Detection of concealed individuals based on their vital signs by using a see-through-wall imaging system with a self-injection-locked radar," *IEEE Transactions on Microwave Theory and Techniques*, vol. 61, no. 1, pp. 696–704, Jan 2013.

[37] R. Adler, "A study of locking phenomena in oscillators," *Proceedings of the IRE*, vol. 34, no. 6, pp. 351–357, June 1946.

[38] B. Razavi, "A study of injection locking and pulling in oscillators," *IEEE Journal of Solid-State Circuits*, vol. 39, no. 9, pp. 1415–1424, Sep. 2004.

[39] C. Li, C. Hsiao, F. Wang, T. Horng, and K. Peng, "A rigorous analysis of a phase-locked oscillator under injection," *IEEE Transactions on Microwave Theory and Techniques*, vol. 58, no. 5, pp. 1391–1400, May 2010.

[40] P. Wu, J. Jau, C. Li, T. Horng, and P. Hsu, "Phase- and self-injection-locked radar for detecting vital signs with efficient elimination of dc offsets and null points," *IEEE Transactions on Microwave Theory and Techniques*, vol. 61, no. 1, pp. 685–695, Jan 2013.

[41] Fu-Kang Wang, Tzyy-Sheng Horng, Kang-Chun Peng, Je-Kuan Jau, Jian-Yu Li, and Cheng-Chung Chen, "Seeing through walls with a self-injection-locked radar to detect hidden people," in *2012 IEEE/MTT-S International Microwave Symposium Digest*, June 2012, pp. 1–3.

[42] F. Wang, C. Fang, T. Horng, K. Peng, J. Li, and C. Chen, "Concurrent vital sign and position sensing of multiple individuals using self-injection-locked tags and injection-locked i/q receivers with arctangent demodulation," *IEEE Transactions on Microwave Theory and Techniques*, vol. 61, no. 12, pp. 4689–4699, Dec 2013.

[43] Y. Chiu, F. Wang, Y. Chou, and T. Horng, "Wearable doppler radar health monitor with gesture control," in *2014 Asia-Pacific Microwave Conference*, Nov 2014, pp. 944–946.

[44] C. Tseng, L. Yu, J. Huang, and C. Chang, "A wearable self-injection-locked sensor with active integrated antenna and differentiator-based envelope detector for vital-sign detection from chest wall and wrist," *IEEE Transactions on Microwave Theory and Techniques*, vol. 66, no. 5, pp. 2511–2521, May 2018.

[45] C. Hsu, L. Hwang, F. Wang, and T. Horng, "Wearable vital sign sensor using a single-input multiple-output self-injection-locked oscillator tag," in *2018 IEEE/MTT-S International Microwave Symposium - IMS*, June 2018, pp. 248–251.

[46] R. E. Arif, M. Tang, W. Su, T. Horng, F. Wang, and C. Tseng, "Designing a metasurface-based tag antenna for wearable vital sign sensors," in *2019 IEEE MTT-S International Microwave Symposium (IMS)*, June 2019, pp. 373–376.

[47] Y. Yuan, C. Lu, A. Y. Chen, C. Tseng, and C. M. Wu, "Noncontact multi-target vital sign detection using self-injection-locked radar sensor based on metamaterial leaky wave antenna," in *2019 IEEE MTT-S International Microwave Symposium (IMS)*, June 2019, pp. 148–151.

[48] C. Huang, C. Ji, X. Wu, J. Song, and X. Luo, "Wideband high directive aperture coupled microstrip antenna design by using a fss super-strate layer," *IEEE Transactions on Antennas Propagation*, vol. 66, no. 3, pp. 1628–1632, 2018.

[49] Ping-Hsun Wu, J. Jau, C. Li, T. Horng, and Powen Hsu, "Vital-sign detection doppler radar based on phase locked self- injection oscillator," in *2012 IEEE/MTT-S International Microwave Symposium Digest*, June 2012, pp. 1–3.

[50] P. Wu and P. Hsu, "Single-antenna phase- and self-injection-locked radar for vital sign sensor module miniaturization," in *2014 IEEE MTT-S International Microwave Symposium (IMS2014)*, June 2014, pp. 1–3.

[51] P. Wu, Feng-Hsu Chung, and P. Hsu, "A 5.8 ghz phase- and self-injection-locked cmos radar sensor chip for vital sign detector miniaturization," in *2016 IEEE MTT-S International Microwave Symposium (IMS)*, May 2016, pp. 1–3.

[52] P. Wu, "Single-chip dynamically time-frequency multiplexed phase- and self-injection-locked cmos vital-sign sensor," in *2017 IEEE MTT-S International Microwave Symposium (IMS)*, June 2017, pp. 1232–1234.

[53] G. Vinci, S. Lindner, F. Barbon, S. Mann, M. Hofmann, A. Duda, R. Weigel, and A. Koelpin, "Six-port radar sensor for remote respiration rate and heartbeat vital-sign monitoring," *IEEE Transactions on Microwave Theory and Techniques*, vol. 61, no. 5, pp. 2093–2100, May 2013.

[54] C. Tseng and L. Yu, "Self-injection-locked aia radar sensor using pll demodulator for n oncontact vital sign detection," in *2018 IEEE/MTT-S International Microwave Symposium - IMS*, June 2018, pp. 252–254.

[55] W. Su, M. Tang, R. El Arif, T. Horng, and F. Wang, "Single conversion stepped-frequency continuous-wave radar using self-injection-locking technology," in *2019 IEEE MTT-S International Microwave Symposium (IMS)*, June 2019, pp. 420–423.

[56] C. Tseng and Y. Lin, "24-ghz self-injection-locked vital-sign radar sensor with cmos injection-locked frequency divider based on push–push oscillator topology," *IEEE Microwave and Wireless Components Letters*, vol. 28, no. 11, pp. 1053–1055, Nov 2018.

[57] M. Tang, C. Kuo, D. Wun, F. Wang, and T. Horng, "A self- and mutually injection-locked radar system for monitoring vital signs in real time with random body movement cancellation," *IEEE Transactions on Microwave Theory and Techniques*, vol. 64, no. 12, pp. 4812–4822, Dec 2016.

[58] Mu-Cyun Tang, Chao-Yun Kuo, Da-Cian Wun, F. Wang, and T. Horng, "Same side dual sil-radar system for real-time vital sign monitoring with random body movement cancellation," in *2016 IEEE MTT-S International Microwave Symposium (IMS)*, May 2016, pp. 1–4.

[59] M. Tang, F. Wang, and T. Horng, "A single radar-based vital sign monitoring system with resistance to large body motion," in *2017 IEEE MTT-S International Microwave Symposium (IMS)*, June 2017, pp. 995–998.

[60] Xiaolue Lai and J. Roychowdhury, "Capturing oscillator injection locking via non-linear phase-domain macromodels," *IEEE Transactions on Microwave Theory and Techniques*, vol. 52, no. 9, pp. 2251–2261, Sep. 2004.

[61] P. Bhansali and J. Roychowdhury, "Gen-adler: The generalized adler's equation for injection locking analysis in oscillators," in *2009 Asia and South Pacific Design Automation Conference*, Jan 2009, pp. 522–527.

[62] G. R. Gangasani and P. R. Kinget, "Time-domain model for injection locking in nonharmonic oscillators," *IEEE Transactions on Circuits and Systems I: Regular Papers*, vol. 55, no. 6, pp. 1648–1658, July 2008.

[63] J. Chien and L. Lu, "Analysis and design of wideband injection-locked ring oscillators with multiple-input injection," *IEEE Journal of Solid-State Circuits*, vol. 42, no. 9, pp. 1906–1915, Sep. 2007.

[64] A. Tofangdarzade and A. Jalali, "An efficient method to analyze lock range in ring oscillators with multiple injections," *IEEE Transactions on Circuits and Systems II: Express Briefs*, vol. 62, no. 11, pp. 1013–1017, Nov 2015.

[65] A. R. Hazeri and H. Miar-Naimi, "Generalized analytical equations for injected ring oscillator with rc -load," *IEEE Transactions on Circuits and Systems I: Regular Papers*, vol. 65, no. 1, pp. 223–234, Jan 2018.

[66] B. Razavi, "A study of phase noise in cmos oscillators," *IEEE Journal of Solid-State Circuits*, vol. 31, no. 3, pp. 331–343, March 1996.

[67] F. Wang, C. Li, C. Hsiao, T. Horng, J. Lin, K. Peng, J. Jau, J. Li, and C. Chen, "A novel vital-sign sensor based on a self-injection-locked oscillator," *IEEE Transactions on Microwave Theory and Techniques*, vol. 58, no. 12, pp. 4112–4120, 2010.

[68] T. H. C. T. S. Y. C. C. F. Wang, C. M. Wu and P. Juan, "Review of self-injection-locked radar systems for noncontact detection of vital signs," *IEEE JOURNAL OF ELECTROMAGNETICS, RF, AND MICROWAVES IN MEDICINE AND BIOLOGY*, vol. 4, no. 4, 2020.

[69] D. Leeson, "A simple model of feedback oscillator noise spectrum," *Proceedings of the IEEE*, vol. 54, no. 2, pp. 329–330, Feb 1966.

[70] A. K. P. U. L. Rohde and G. Boec, *Modern Microwave Oscillators for Wireless Applications: Theory and Optimization*. Hoboken, NJ: Wiley, 2005.

[71] A. K. Poddar, U. L. Rohde, and A. M. Apte, "How low can they go?: Oscillator phase noise model, theoretical, experimental validation, and phase noise measurements," *IEEE Microwave Magazine*, vol. 14, no. 6, pp. 50–72, Sep. 2013.

[72] A. Mirzaei and A. A. Abidi, "The spectrum of a noisy free-running oscillator explained by random frequency pulling," *IEEE Transactions on Circuits and Systems I: Regular Papers*, vol. 57, no. 3, pp. 642–653, March 2010.

[73] T. H. Lee and A. Hajimiri, "Oscillator phase noise: a tutorial," *IEEE Journal of Solid-State Circuits*, vol. 35, no. 3, pp. 326–336, March 2000.

[74] A. A. Abidi, "Phase noise and jitter in cmos ring oscillators," *IEEE Journal of Solid-State Circuits*, vol. 41, no. 8, pp. 1803–1816, Aug 2006.

[75] S. A. C. Demartinos, A. Tsimpos and G. Souliotis, "Delay elements suitable for cmos ring oscillators," *JOURNAL OF Engineering Science and Technology Review*, vol. 9, no. 4, pp. 98 – 101, Sep. 2016.

[76] N. Tripathi and S. N. Pradhan, "Design of power efficient all digital phase locked loop (adpll)," in *2016 International Conference on Wireless Communications, Signal Processing and Networking (WiSPNET)*, March 2016, pp. 778–782.